SOME ASPECTS OF THE CRASHWORTHINESS OF RAIL VEHICLES : VOLUME I

Lik-Beng Lim, *BEng.*

A thesis submitted for the degree of
Doctor of Philosophy at the University of Sheffield

Department of Mechanical and Process Engineering

January, 1996

Abstract

This thesis describes the studies carried out by the author on two aspects of the crashworthiness of rail vehicles : (1) The behaviour of rakes of vehicles during collisions; (2) Interior crashworthiness for occupants (passengers) during secondary collisions.

The investigation of the behaviour of vehicles in rakes aims to study how the initial kinetic energy is partitioned amongst the vehicles after impact. Head-on collisions between two rakes of up to seven coaches were simulated using two non-linear Finite Element codes. The model, which correlates well with British Rail's full scale test results, assumes that a rake of coaches may be represented by a series of masses connected by non-linear springs. Important parameters that governed the rake behaviour have been identified. The effects of inter-vehicular distances, velocity-sensitive couplers, number of coaches, initial impact velocities and spring characteristics (e.g. constant collapse force, softening, hardening etc.) on energy distribution along colliding rakes have been studied and discussed.

In order to study the behaviour of passengers in the vehicle interior during the collision, acceleration pulses generated by the above rake models were used as input to Finite Element models of the vehicle interior which included dummies, placed in various seating arrangements. The investigation of interior crashworthiness of occupants began by 'tuning' some selected input parameters of the non-linear Finite Element dummy model so that its behaviour matched that found in an actual sled test. The effects of various pulses on the occupant have also be investigated. These pulses contain the parametric effects caused by couplers, damping forces, spring characteristics, initial impact velocities and inter-vehicular distances. Assessments of the injury potential of occupants are based on comparing the selected output forces/moments from the dummy models to well-established human injury criteria.

Another major aspect of this crashworthiness study included an investigation into the collapse behaviour of simple components (e.g. tubes and beams) in order to gain an insight as to how energy is absorbed during structural collapse. It is also important to study how recycled energy absorbers function and how much energy absorbing capacity has been lost after the recycling process. Studies of this nature are included in the Appendices of this thesis for tubes made from High Density Polyethylene (HDPE).

To my mother

Contents

Acknowledgements

I would like to express my gratitude to my supervisor, Professor R. A. Smith, for his guidance and support throughout this research programme.

The following people must also be mentioned here for their invaluable advice and assistance during the course of my PhD:

- Staff from British Rail Research at Derby, particularly Mr. J. H. Lewis, the success of this research programme owes much to them;
- FE analysts from Ove Arup & Partners, who offered professional advice concerning the use of DYNA3D;
- Dr. K. W. Distin, who generously shared his experience and knowledge;
- Mr. Williams and Mr. Chalk for releasing the technical details concerning Oleo couplers;
- Mr. C. Nex, Mr. J. J. Carruthers and Mr. N. R. Harris, for their help, friendship and for reading the thesis drafts;
- Dr. Y. Liu and Dr. X. B. Lin.

Last but not least, I would like to express my utmost gratitude to my family, especially my mother, for the support and encouragement I have received throughout the research programme here in the UK.

Lik-Beng Lim

January 1996

References

References in this thesis are included in the text using numbers in square brackets and are listed at the end of each Chapter.

Declaration

This research has been carried out in the Department of Mechanical and Process Engineering at the University of Sheffield between October 1992 and January 1996. The contents of this thesis are original and are solely the work of the author except otherwise stated. No part of this thesis has been submitted to any other university or institution.

L. B. Lim

January 1996

Chapter 1
Introduction

1.1 What is crashworthiness ?

The crashworthiness of a vehicle is defined as the ability of the vehicle and its cargo to withstand the trauma of an unplanned collision. The study of crashworthiness is a very broad subject which encompasses impact engineering, biomechanics, dynamic strength of materials, energy absorption of engineering components, non-linear finite element analysis, fire dynamics and many other mechanical engineering sciences. It is a fast growing research subject which is widely studied and applied in the transport and nuclear industries.

Research in crashworthiness can broadly be divided into : (1) Structural crashworthiness and (2) Interior crashworthiness. Structural crashworthiness is concerned with the design of vehicle body and structural members for achieving a desirable controlled collapse characteristic to provide the collision energy absorption and deceleration pulse. Interior crashworthiness aims to design a safe interior environment for the passengers within a vehicle so as to reduce their injury potential due to secondary collisions between the passengers and the interior when the vehicle is subjected to a sudden acceleration or deceleration. A transporting body may be thought of as consisting of a protective container with decoupled cargoes within. During collisions, the structural body of the container suffers the impact and undergoes damage locally in the impact region. This is known as a primary collision and is the subject of interest for structural crashworthiness studies. As a direct consequence of the primary collision, a deceleration pulse is generated to the container and its fixtures which creates a relative velocity between the decoupled cargoes and the interior fixtures (mainly seats and floor), and impact between them inside the container soon follows. This is termed as a secondary collision and is the main interest for studying interior crashworthiness.

Due to its rapid growth as a stand alone engineering subject, there is now an English language journal which exclusively devotes itself to crashworthiness : The International Journal of Crashworthiness. The first volume is expected to be published in early 1996.

1.2 Crashworthiness in the automobile industry

According to Burstall [1], the current century up till 1963 can be separated into two distinct periods in terms of achievements in Mechanical Engineering : (1) The age of mechanical road and air transport, 1900-1940, and (2) The age of nuclear energy and space travel, 1940-1963. The second period has extended to present days. One prominent characteristic of the transport vehicles designed and manufactured during these periods is that they operate at higher speeds with resulting large increases in kinetic energy. This has served the consumers well in terms of convenience and efficiency but has also subjected them to greater danger should collisions occur. Where and how should the large amount of kinetic energy be dissipated safely during a collision? Designing a vehicle which is comfortable, economical and aesthetically nice

can no longer satisfy the consumers. Designers are obliged, legally and by profession, to ensure that the designed vehicle can cope with an unexpected collision such that the passengers are subjected to minimum potential of injury. Public opinion on safety has also placed considerable pressure on the designers to continuously provide better protection against injury from vehicles undergoing collision, and as people are generally becoming better educated and well informed, such pressure has been increasing over the years. It is perhaps not too much to expect from drivers nowadays to appreciate the fact that the damaging power in colliding vehicles is proportional to the speed squared [2] and that during a vehicular collision the designed crush zones should provide the passengers with the necessary survival space [3]. See Figure 1.1.

A common way of cushioning heavy colliding objects is the use of energy absorbers. Assuming that the impact entities are brought to rest eventually (e.g. two equal masses travelling at an equal and opposite velocity), the mean retarding force (P) which acts during the impact can be related to the kinetic energy (E_k) and the distance (x) over which the force acts by the relationship :

$$P = \frac{E_k}{x} \tag{1.1}$$

For a given E_k , x is inversely proportional to P and since the retardation is directly proportional to P, an energy absorber can be thought of as a load limiter which trades distance with time. A collapsible energy absorber dissipates the kinetic energy into its structure as strain energy, so the structural integrity of the absorber is sacrificed in elastic or plastic deformation. The absorbers could be some form of external device (such as car bumpers) attached to the colliding bodies or, as generally is the case, part of the colliding bodies (the crush zone shown previously in Figure 1.1).

The idea of using collapsible impact energy absorbers (structural crashworthiness) in the automotive industry flourished during the sixties [4,5]. At the same time, research and development for studying human response (interior crashworthiness) to a dynamic impact environment also began [6]. Cadavers and dummies were used to simulate human response during sled tests. Dummies were designed by the motor industry which has over the years developed instrumented dummies for use in the standard tests which are conducted to demonstrate conformance of the vehicle with legislation. These dummies have been upgraded from time to time to improve their bio-fidelity. The latest versions are the HYBRID III family, which have instrumentation designed for frontal impact. For side impacts further dummies have been developed such as the EUROSID, US-SID, BIOSID etc.. Car manufacturers such as the Volvo, a company well known for its dedication to designing safe and crashworthy cars, have extensively applied the dummy family for their tests to suit the variety of their potential customers' shapes and sizes as shown in Figure 1.2 [7]. It must be noted that cadavers are still used by some of the car manufacturers for their interior crashworthiness research programmes [8].

Earlier mathematical models that represent human were grossly simplified due to the restricted computational resources in terms of both hard and software, but with the advent of digital computers and explicit finite element codes in recent years, dummies have been incorporated into FE models as standard database, ready to be merged into user defined interior settings for secondary impact simulations; see Figure 1.3 [6].

1.3 Crashworthiness in the railway environment : British Rail

Studies in interior crashworthiness for rail vehicles are similar to those of the motor cars but due to the large amount of kinetic energy involved in rail vehicles, there are some fundamental differences in structural design requirements between a rail coach and a motor car. British Rail (BR) Research has been advancing the development of structural crashworthiness in rail vehicles for over a number of years, both with tests (see Figure 1.4) [9] and numerical computations [10]. BR chaired the ORE-B165 committee formed in 1983, in search of a unified structural design code for the European railways. At the beginning of this period in 1985, a paper was published by Scholes [11], advocating the need to incorporate plastic energy absorption criteria (i.e. crumple or crush zones at the ends of a coach) into the structural design requirements of rail vehicles, to supplement the static structural proof loading requirements set by the International Union of Railways (UIC). However towards the end of this paper, he stated that the idea published was his own opinion and did not represent the official BR philosophy. Eight years later, in another paper with Lewis [12], it was confirmed that the idea has been incorporated into BR design philosophy. Note that the concept of different stages of controlled structural collapse by plastic deformation for rail vehicles was proposed by Pugsley in 1960 [4], and there is evidence that the concept had been promoted at even earlier dates.

Prior to 1989, the research effort in BR was mainly devoted to improving structural crashworthiness. However, an incident that occurred in the late eighties was to abruptly steer and boost the overall BR research programmes in the early nineties.

On the morning of 12th December 1988, two commuter trains collided just south of Clapham Junction station, killing 35 people, and causing 69 major and 350 minor injuries. A public inquiry was convened to formally investigate the accident. The inquiry made some recommendations to BR, one of which required BR to extend its research programmes "to include dynamic testing of full scale simulations of collision retardations in order to improve the design of internal furniture under conditions of passenger impact" [13]. As a result, large resources were committed by BR to establish suitable design codes for both structural and interior crashworthiness for its entire service fleet.

A very large amount of work (tests and computer modelling) went into the post-Clapham programme and eventually led to the current enhanced structural crashworthiness development in BR Research.

Some of the initial research work on interior crashworthiness for the post-Clapham programmes were contracted to the Motor Industry Research Association (MIRA) and Vehicle Safety Consultants Ltd. (VSC) so as to share their expertise in this field. Subsequently BR acquired a non-linear finite element code and developed its own capability to perform some of the structural and interior crashworthiness studies. Consequently, BR has gained considerable expertise over the past few years which is vital for the development of a comprehensive crashworthiness design code for rail vehicles.

1.4 Applications of crashworthiness in other fields

The following paragraphs highlight some examples of the applications of crashworthiness in the nuclear, mining and other transport industries, among many others.

The design of a nuclear reactor with vertical fuel channels must have provisions to guard against the accidental dropping of components. To absorb the energy consequent on dropping some components, it is usual to provide energy absorbing devices [14].

The aerospace industry also has intensive interior crashworthiness research activities due partly to regulatory pressure. Once an aircraft is airborne, it has to be self sufficient in all safety measures during any emergency. Many aspects of airliner crashworthiness are featured in [15]. Fire hazards are a main concern for airliners which have recently prompted some serious questions about the use of composites in aircrafts. The Manchester disaster in August 1985 in which nearly all the victims were poisoned by toxic smoke billowing from melting plastic and burning seats, is still well remembered [16].

Ships not only collide with other ships but also with bridges and docking structures, see Figure 1.5. Although the occurrences of such accidents are not frequent and are far less common than road accidents, the scale of damages both in terms of cost and casualties for one shipping disaster can be considerable and newsworthy. Full scale collision tests for ships are not practical but some component collision tests have been conducted, such as the test on a ship's bow as shown in Figure 1.6 [15].

The Markham colliery disaster on the 30th July 1973 which killed 18 mine workers, "would not had been so serious", according to the official report after the investigation of the incident, "if instead of landing baulks, an arresting cushioner (energy absorbing device) had been installed below the lowest winding level". Thus it was recommended that all solid landings in shafts be replaced by suitable arresting devices below the lowest winding level [15].

1.5 Summary of work done in this thesis

This thesis reports the work done by the author from September 1992 to September 1995 using the facilities provided in the Department of Mechanical & Process Engineering, University of Sheffield. The chart over the page provides the overview of the areas covered in this thesis : bracketed number inside a box indicate the Chapter number. It is provided as a guiding map to assist navigation of the thesis.

The deceleration pulses derived from mass-spring models (dotted lines in the Chart) in Chapters 4 and 6 were used as input pulses to forward facing dummy models in Chapter 8.

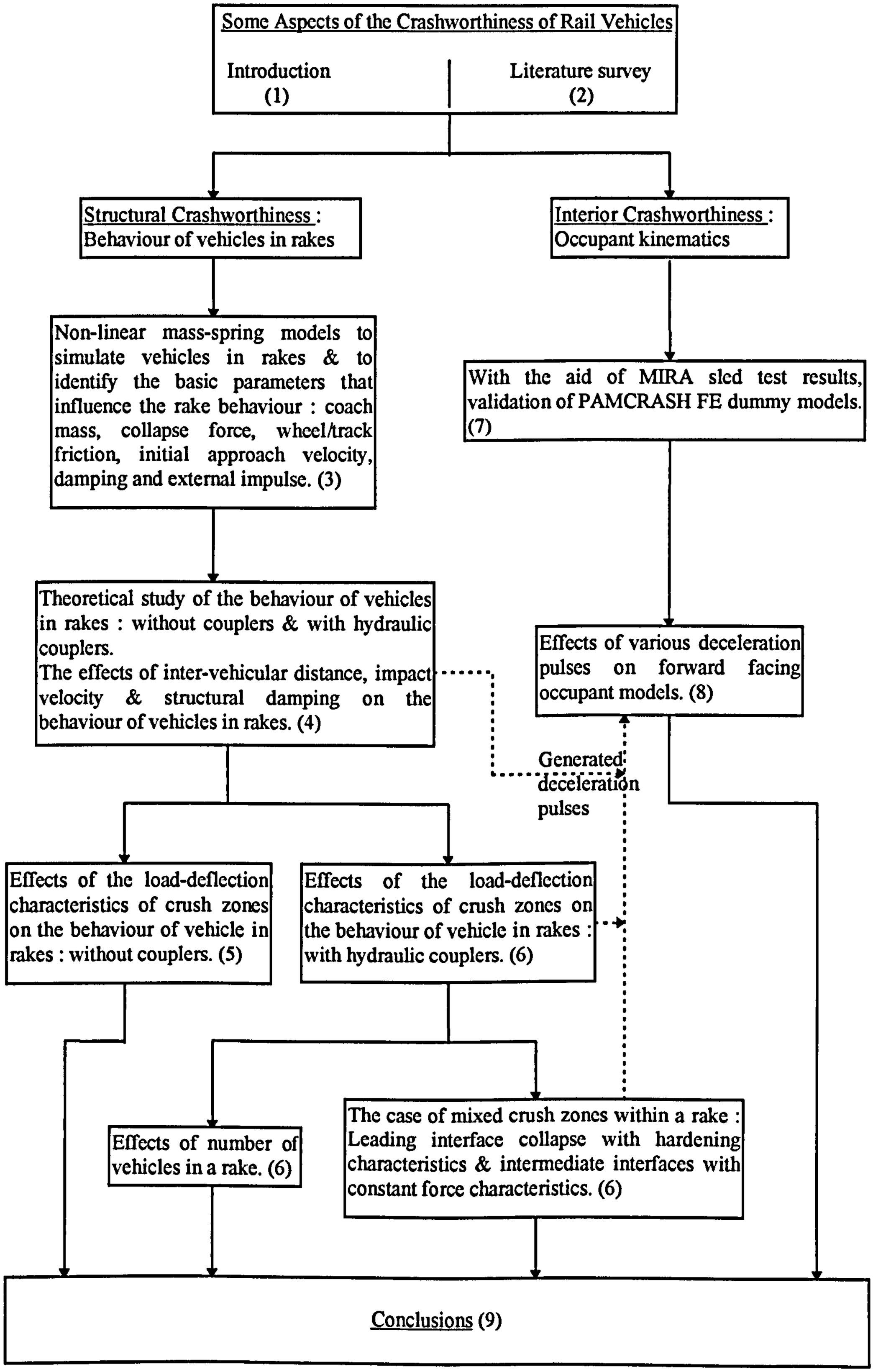
Some Aspects of the Crashworthiness of Rail Vehicles
Introduction (1)
Literature survey (2)
Structural Crashworthiness : Behaviour of vehicles in rakes
Interior Crashworthiness : Occupant kinematics
Non-linear mass-spring models to simulate vehicles in rakes & to identify the basic parameters that influence the rake behaviour : coach mass, collapse force, wheel/track friction, initial approach velocity, damping and external impulse. (3)
With the aid of MIRA sled test results, validation of PAMCRASH FE dummy models. (7)
Theoretical study of the behaviour of vehicles in rakes : without couplers & with hydraulic couplers.
The effects of inter-vehicular distance, impact velocity & structural damping on the behaviour of vehicles in rakes. (4)
Effects of various deceleration pulses on forward facing occupant models. (8)
Generated deceleration pulses
Effects of the load-deflection characteristics of crush zones on the behaviour of vehicle in rakes : without couplers. (5)
Effects of the load-deflection characteristics of crush zones on the behaviour of vehicle in rakes : with hydraulic couplers. (6)
Effects of number of vehicles in a rake. (6)
The case of mixed crush zones within a rake : Leading interface collapse with hardening characteristics & intermediate interfaces with constant force characteristics. (6)
Conclusions (9)

Prior to the commencement of the crashworthiness studies as highlighted on the previous page, some experiments were conducted on axially loaded cylindrical thermoplastics shells for investigating their energy absorbing capability. The investigation of the buckling of solid struts and thin-walled tubes, of circular and non-circular cross section, when subjected to static and dynamic axial compression is a very common subject for crashworthiness research. It also provided a good start for the present series of crashworthiness studies. Thermoplastics tubes were chosen because of their ability to partially restore the uncrushed geometry after reheating the crushed tubes in boiling water. The idea of a recycling impact energy absorber is very attractive and worthy of further investigation. This work for thermoplastic tube crushing is reported in Appendix A.

Some non-linear F.E. analyses on the tube crushing using the non-linear F.E. code DYNA3D were conducted, mainly for allowing the author to become familiar with the new software, and at the same time to compare experimental and computational results of thermoplastic tube crushing. These computations for tube crushing are reported in Appendix B.

This thesis consists of two volumes, one for the text and the other for the figures, to assist cross referencing between text and figures. Mathematical symbols are introduced as they appear in individual Chapters. References are cited in the text of each Chapter by numbers in square brackets and are listed at the end of each Chapter.

References

[1] Burstall, A. F., "A History of Mechanical Engineering.", Faber and Faber, London, 1963.

[2] Johnson, W., "The Elements of Crashworthiness : Scope and Actuality.", Proc. IMechE., Vol. 204D, p. 255, 1990.

[3] Dellis, E. A., "Evolutions in Safety.", Automotive Engineering, Vol. 98, No. 1, p. 51, January 1990.

[4] Pugsley, A. G., "The Crumpling of Tubular Structures under Impact Conditions.", Symposium on the Use of Aluminium in Railway Rolling Stock, Paper 4, Inst. Loco. Engr., London, p. 33, November 1960.

[5] Miura, N. & Kawamura, K., "An Analysis of Deformation Mechanism in Head-on Collisions," SAE Paper No. 680484, 1968.

[6] Lupker, H. A., de Coo, P. J. A., Nieboer, J. J. & Wismans, J., "Advances in MADYMO Crash Simulations," SAE Paper No. 910879, February 1991.

[7] Almqvist, R., "Volvo Safety Design Philosophy," Int. J. of Veh. Design, Special Issue on Vehicle Safety, Vol. 7, p. 76, 1986.

[8] Gedye, R., "Bodies 'Sold on Cheap' for Crash Tests", Daily Telegraph, 20 November 1993.

[9] Smith, R. A., "Crashworthiness Moves From Art to Science.", Railway Gazette Int., p. 227, April 1995.

[10] Sutton, A. & Lewis, J. H., "Elastic/plastic interaction of rakes vehicles," Structural Impact and Crashworthiness, Vol. 2, Edited by Morton, J., Elsevier Applied Science Publications, p. 783, 1984.

[11] Scholes, A., "Passenger vehicle design loads and structural crashworthiness," IMechE. Conference on Railway Vehicle Body Structures, Paper No. C294/85, Mechanical Engineering Publications, London, p. 147, 1985.

[12] Scholes, A. & Lewis, J. H., "Development of crashworthiness for railway vehicle structures," Proc. IMechE., Vol. 207, p. 1, 1993.

[13] Hidden, A., "Investigation into the Clapham Junction Railway Accident," The Department of Transport, HSMO, London, November 1989.

[14] Alexander, J. M., "An Approximate Analysis of the Collapse of Thin Cylindrical Shells Under Axial Loading.", Quart. J. Mech. Appl. Math., Vol. XIII, p. 10, 1960.

[15] Johnson, W. & Mamalis, A. G., "Crashworthiness of Vehicles," Mechanical Engineering Publications, London, 1978.

[16] Barthorpe, F., "Danger Fibres on Fire," Professional Engineering, Vol. 8, No. 11, p.10, June 1995.

Chapter 2
Literature survey

2.1 Introduction

The phenomenal development of crashworthiness would seem inevitable in modern times in which advances in technology have led to larger vehicles moving at higher velocities with the potential for ever more serious damage to people, the surrounding environment and the vehicles themselves. The objective of any crashworthiness research is to safeguard the people, cargoes and vehicles from excessively high retardations and hence damages. The study of crashworthiness involves large deflections and high strain-rate loading of structures, which the traditional linear elastic analyses fail to handle; the more sophisticated theory of plasticity has to be applied instead. The matter is made even more complicated by the fact that the study of crashworthiness also involves dynamics.

Despite rapid development in the field of crashworthiness, few books can be found which totally devote themselves to the subject. Pugsley's "The Safety of Structures" [1] is a classic text, which discusses real safety problems faced by engineers up to the late sixties, and contrasts the extensive progress or development made during the past two decades. "Crashworthiness of Vehicles" by Johnson and Mamalis [2] is an excellent monograph which provides a very good overview on the subject and makes a useful primer for beginners. Johnson has produced an across-the-board survey to update [2] in a recent publication [3]. The book "Structural Impact" by Jones [4] provides some useful theoretical background on structural crashworthiness, with the last Chapter discussing some aspects of impact injury. Another volume "Introduction to Impact Engineering" by Macaulay [5] is also an excellent book with lesser technical detail than [4] and it aims to serve as an introductory guide at a level which is intelligible to the non-specialist, but in sufficient detail for an interested reader to move on to specialist published work.

Proceedings of many conferences on structural or interior crashworthiness held over the past few years also provide useful and up-to-date technical information on the subject. Two proceedings of such a nature are "Structural Crashworthiness" edited by Jones [6] and "Structural Impact and Crashworthiness" in two volumes, volume 1 edited by Davies [7] and volume 2 by Morton [8].

Until the anticipated first publication of the International Journal of Crashworthiness in January next year, there has been no journal which is exclusively devoted on the subject of crashworthiness. However, informative articles can frequently be found in parts D and E of the IMechE Proceedings, the International Journal of Impact Engineering, the International Journal of Mechanical Science and the International Journal of Vehicle Design.

This Chapter provides a literature review on the subject of crashworthiness with the emphasis placed on its application to rail vehicles. BR research has, over the years, produced an extensive collection of its own research reports/memoranda both in structural and interior crashworthiness, and many of which the author has constantly

referred to. Most of the works reported in this thesis have been based on information extracted from the extensive published works by BR research.

The review in this Chapter is organized into Sections as shown in the contents page. Some important background information will be briefly reiterated in future Chapters when the need arises.

2.2 Basic concepts

2.2.1 Impact mechanics

High velocity impacts between heavy masses nearly always involves the plastic collapse of structures, and the conversion of kinetic energy into strain energy. In order to better understand the mechanics of inelastic collisions, Calladine [9] has proposed a three stage schematic representation for the collinear impact between an isolated system of two bodies as shown in Figure 2.1. Stage 1 is prior to contact, stage 2 is during the contact and stage 3 is the post impact phase. The intermediate diagrams between each stage show the impulses which act between stage 1 and 2 (loading phase during contact) and stage 2 and 3 (unloading phase during contact). Two useful graphical interpretations of such an inelastic impact event are shown in Figure 2.2a (the force-deflection graph for the contact region) and 2.2b (the impulse history for the impact event). The results shown on these graphs are schematic and only serve to represent typical impact response. The numbers 1, 2 and 3 as labeled on these graphs denote the three stages of the impact. The following equations as derived by Calladine in [9] supplement the information given in Figure 2.1 and 2.2 (refer to Figure 2.1 for the nomenclature of the notations) :

$$\frac{E_{23}}{E_{12}} = \frac{(V_3 - v_3)^2}{(V_1 - v_1)^2} = e^2 \tag{2.1}$$

and

$$\frac{I_{23}}{I_{12}} = e \tag{2.2}$$

where

$$E_{12} = \int_1^2 P \, du \tag{2.3a}$$

is the energy dissipated during the loading phase and

$$E_{23} = \int_2^3 P \, du \tag{2.3b}$$

is the energy released during the unloading phase. Also

$$I_{12} = \int_1^2 P\, dt \tag{2.4a}$$

and

$$I_{23} = \int_2^3 P\, dt \tag{2.4b}$$

are the corresponding impulses during the loading and unloading phase respectively. e is the coefficient of restitution, which is a measure the irreversibility of the contact process, where $0 \leq e \leq 1$.

Two special cases of e are of great interest in impact mechanics : the case of e=1, representing a purely elastic impact with full recovery of initial kinetic energy after impact; and e=0, representing a fully plastic impact with total energy dissipation without any recovery of energy and the two vehicles move together at the same velocity after the impact. The special case of e=0 is of particular interest for application in rail vehicles, since collisions of rail vehicles usually involved negligible amount of energy recovery during the unloading phase, i.e. e≅0. Consider a vehicle of mass M with velocity V_1 impacting another vehicle of mass m travelling at v_1. To be consistent with the notation used in Figure 2.1, let the velocities after impact be V_3 and v_3 for M and m respectively. From momentum conservation :

$$MV_1 + mv_1 = MV_3 + mv_3 \tag{2.5}$$

and from energy conservation :

$$\frac{1}{2}MV_1^2 + \frac{1}{2}mv_1^2 = \frac{1}{2}MV_3^2 + \frac{1}{2}mv_3^2 + E_D \tag{2.6}$$

Whence E_D is defined as the plastic energy or collision energy [10]. For a purely elastic collision E_D=0 and e=1, and :

$$V_3 = \frac{(M-m)V_1 + 2mv_1}{M+m} \tag{2.7}$$

and :

$$v_3 = \frac{2MV_1 + v_1(m-M)}{M+m} \tag{2.8}$$

For a purely plastic collision :

$$V_3 = v_3 = \frac{MV_1 + mv_1}{M+m} \tag{2.9}$$

and

$$E_D = \frac{1}{2}\frac{Mm(V_1 - v_1)^2}{M+m} \tag{2.10}$$

The above were re-derived from Reference [11], although a different version can be found in [10] among many others. Carney [11] also established a useful form of mathematical expression between the dissipated plastic energy E_D and the coefficient of restitution e for the impact between two masses M and m travelling initially at V_1 and v_1 respectively, as shown in Equation 2.11 :

$$\frac{E_D}{E} = \frac{\frac{M}{m}(1-e^2)[1-\frac{v_1}{v_1}]^2}{[1+\frac{M}{m}][\frac{M}{m}+(\frac{v_1}{v_1})^2]} \tag{2.11}$$

where E is the initial kinetic energy of the system. The highly non-linear nature of the relationship between the energy ratio (E_D/E), the coefficient of restitution e, the mass ratio (M/m) and the velocity ratio (V_1/v_1) can be seen in Equation (2.11).

Equations 2.1 to 2.11 are simple but have one major setback : they can only be applied to an isolated one-to-one collinear impact situation and not to any system with inter-connected multiple-bodies.

2.2.2 Vehicle size and crashworthiness

Assume that a long, tubular structure collides end-on with a rigid wall and experiences a uniform resisting force 'σA', where 'σ' is the mean collapse stress for the structure and 'A' its cross sectional area (assuming 100% full face collapse). The mass of the structure is 'ρAL' where 'ρ' is its density and 'L' its length. Thus the uniform retardation 'a' is :

$$a = \frac{\sigma A}{\rho AL} = \frac{\sigma}{\rho L} \tag{2.12}$$

Hence if structures differ only in length, the retardation arising in collisions, with this idealized approach, would be inversely proportional to their length [12, 2]. If passenger injury is assumed to arise from a retardation that is too high, then ships could be considered fairly safe, aircraft somewhat less so, railway coaches even lesser so and motor cars most dangerous [2]. Johnson *et al.* attributed this size effect to the much lower fatality rate (fatality per one million passenger-miles) for passengers in buses and trains as compared to motor cars, for the accidents recorded in the USA during 1970-72 [13]; but obviously other factors affect the observed fatality rates.

The effect of the size of a vehicle on its crashworthiness can also be expressed in terms of its mass. Suppose two vehicles M (heavy) and m (light) approach and impinge head-on at velocities V_1 and $-v_1$ respectively. Assuming a fully plastic collision and the two

vehicles adhere after impact, then by rearranging Equation 2.9, the post impact velocity V_3 or v_3 is :

$$V_3 = v_3 = \frac{[(\frac{M}{m})V_1 - v_1]}{[(\frac{M}{m}) + 1]} \tag{2.13}$$

Note that m is initially moving in the opposite direction of the heavier vehicle and after the impact the final velocity of both vehicles is in the direction of the heavier vehicle. Now a typical mass ratio for a truck to a motor car would be 20 and assuming both were travelling at an equal and opposite 40mph, then the reduction in speed for the combined truck and car is to 36mph. The truck 'feels' an impact of only 4mph whereas the car 'feels' 76mph [3]! Hence, incompatibilities of mass between road vehicles makes a large contribution to all categories of road user casualties [3]. Increasing the mass of a vehicle could thus be viewed as its rudimentary level of enhanced crashworthiness, but this is of course carried out at the expense of its running cost.

2.2.3 Structural crashworthiness performance indicators

To design a component that performs appropriately in a vehicle crash, a number of measures of its energy absorption efficiency (as derived from its collapse load-deflection characteristics, see Figure 2.3) can be defined [14] :

$$\text{Load efficiency } E_L = \frac{P_m}{P_u} = 1 - \frac{P}{2P_u} \tag{2.14}$$

$$\text{Geometric efficiency } E_G = \frac{d}{l_o} \tag{2.15}$$

$$\text{Energy efficiency } E_e = \frac{A}{P_o l_o} \tag{2.16}$$

$$\text{Specific energy per unit length } E_S = \frac{P_m}{\rho A_x} \tag{2.17}$$

where :

P_u = Mean value of maximum loads during collapse;
P_L = Mean value of minimum loads during collapse;
} $P = P_u - P_L$

P_m = Mean collapse load;
P_o = Maximum load observed during collapse;
d = Total compression experienced by specimen of original length l_o;
A = Area under one cycle of the load/deflection curve;
ρ = material density;
A_x = Cross section area of the collapse section.

These efficiency indicators are mainly for evaluating the energy absorbing performance of a component or element that forms part of an overall structure. E_L is a measure of the smoothness of the deceleration produced for a given amount of energy dissipation. E_G is a measure of how much of a given mass or volume of material can be crushed to limit the deceleration forces. E_e is a measure of the deviation of an energy dissipating device from the ideal constant force plastic collapse behaviour, and E_s compares the weight efficiency of various energy absorbers. It must be noted that the energy absorption that accompanies structural collapse is governed by three factors : material properties, structural geometry and collapse mode. Thornton *et al.* together with various other workers [14], have attempted to combined these three factors in a simple empirical expression which fitted reasonably well with a wide range of the experimental data :

$$\eta = m\phi^n \tag{2.18}$$

where the parameter η is known as the structural effectiveness and is the ratio of the specific energy absorption to the specific ultimate tensile strength. The parameter $\varnothing$ is known as the solidity ratio and is the ratio of the actual cross sectional area of the energy absorber to the area enclosed by its cross section. m and n are constants depending on the collapse/failure modes. As a general guide, it is better to have plastic folding rather than fracture or local bending during the energy absorbing process and for the same solidity ratio and material, circular tubes were found to be better than square tubes in terms of energy absorption capacity [14]. Over a wide range of material properties, provided the structural geometry and collapse mode are the same, the specific energy absorbed is proportional to the ultimate tensile strength [14].

2.3 Energy dissipating systems

2.3.1 A general review

There are many literature reviews on energy dissipating systems for applications in structural crashworthiness by workers such as Rawlings [15], Johnson and Mamalis [2], Johnson and Reid [16], Johnson [3] and Jones [17]. In general, an energy absorber is a once-only device since it irreversibly absorbs energy through plastic deformation or fracture while cushioning a collision. Many workers have conducted experimental and theoretical studies on the collapsed behaviour of tubular and cellular structures when subjected to different modes of loading. The following Sections briefly describe some of their findings and discussions.

2.3.2 Axial crushing of tubes

General

The buckling of cylindrical shells under axial load is a classical problem in solid mechanics and due to the seemingly countless amounts of published work on this subject, it is impossible to discuss it extensively. On the basis of energy absorption

capacity and available stroke, cylindrical tubes under axial compression provide one of the best energy absorption devices. Used beer cans have proved to be effective energy absorbers in low-speed car collisions as shown by Wirsching and Slater [18]. This is due to the combination of bending and/or stretching modes of deformation and the progressive nature of collapse along a tube. A tube wall buckles into either an axisymmetric-ring mode as shown in Figure 2.4 or into a mode of multiple diamond lobes as shown in Figure 2.5. The mode into which a tube collapses depends on its thickness to mean diameter ratio (t/D), its axial length to mean diameter ratio (L/D) and its material properties. In general tubes with a high t/D ratio will deform into axisymmetric rings, whereas low t/D tubes will adopt the diamond fold mechanism. Horton *et al.* [19] have carried out some experiments on copper, aluminum and stainless steel tubes with various diametrical and axial dimensions and suggested that for a particular D, t/D and material, there is a critical length at which there is a high probability of a compressed tube changing its failing mode from axisymmetric ring to multiple diamond lobes. Andrews *et al.* [20] also conducted an extensive experimental study on aluminum alloy tubes and managed to construct a classification chart to determine a particular collapse mode with a prescribed pair of t/D and L/D for the tubes. The classification chart is reproduced in Figure 2.6. It seems clear that for tubes that are sufficiently long would fail by the Euler bucking failure mode. The collapse mode of a tubes is an important aspect here since it affects the energy absorption capacity.

Figure 2.7 shows some typical load-deflection curves, each curve obtained by compressing a cylindrical tube between parallel rigid platens. The various deformation modes of the tube are also indicated in Figure 2.7 [19]. A general trend of behaviour is observed from these curves : after an initial peak load (the critical buckling load for the tube), which starts the collapse process and marks the formation of the first plastic collapse ring or diamond, the subsequent buckles fold flat in succession along the tube length giving a load that oscillates about a mean value, known as the mean post-buckling load (P_m). Thornton and Magee [21] have commented that the average collapse load remains constant throughout the entire collapse process despite the fact that buckling, which is an unstable phenomena, has taken place. The initial peak load could be removed by crimping the end of the tube [21] if so desired, but Wirsching and Slater [18] have suggested that the peak load would assist in maintaining the structural integrity of, for example, the beer-can car bumper during very low speed bumps, thus 'preserving' the beer cans for deformations in higher velocity collisions where an energy absorber is required.

Theories for predicting initial buckling load or mean post-buckling load

The initial buckling stress for an axially loaded tube was derived by Timoshenko and Gere [22] based on the theory of elastic instability :

$$\sigma_{cr} = \frac{Et}{R\sqrt{3(1-\nu^2)}} \tag{2.19}$$

where σ_{cr} is the predicted critical buckling stress, R is the tube radius, t is the tube wall thickness, E is the Young's modulus and ν is the Poisson's ratio for the material of the

tube. This predicted critical stress (load) was never achieved experimentally and the deviations are usually ascribed to the imperfections (material or geometrical) in the tube wall [18, 19, 21, 23].

A number of theories have been developed by various authors for predicting the mean post-buckling load (P_m) during the steady state collapse phase. It is important to predict P_m since the majority of the impact energy is dissipated during the post-buckling phase.

Alexander [24] gives a rigid-plastic analysis for axisymmetric plastic buckling of a tube of diameter D and thickness t which resulted in the following expression :

$$P_m = K\sigma_y t^{1.5} D^{0.5} \tag{2.20}$$

where K is a constant approximately equal to 6 and σ_y is the uni-axial yield stress in tension and compression (assumed equal). Due to its simplicity, Equation 2.20 has been widely used for axial tube buckling in the context of energy absorption. Abramowicz and Jones [25] have recently improved Alexander's theory by considering a more realistic deformation mode of the tube with linear hardening. Alexander's solution assumes that a circumferential section of the tube of the original length 2H, fully collapses into a flat disc of thickness negligible compared to 2H (Figure 2.8). The improved version introduced a correction for the effective crushing distance of the axisymmetric mode of deformation as shown in Figure 2.9. The final expression as obtained by Abramowicz and Jones is :

$$\frac{P_m}{\sigma_y t^2 / 4} = \frac{20.79(D/t)^{0.5} + 11.90}{0.86 - 0.57(t/D)^{0.5}} \tag{2.21}$$

A similar rigid-plastic analysis for the diamond folding mode of deformation was developed by Pugsley and Macaulay [26]. Their analysis involved a division of the work done in crushing the tube into the energy dissipated by the rotation of plastic hinges and the energy absorbed due to large scale plastic shearing effect. A semi-empirical estimate of the mean crushing force is given by :

$$P_m = P_y\left[C_1\left(\frac{2t}{D}\right) + C_2\right] \tag{2.22}$$

where P_y is the yield stress multiplied by the cross-sectional area of the tube. C_1 and C_2 are constants with the value 1.6 and 0.12 respectively for the three diamond-lobe collapse mode, and 2.1 and 0.15 respectively for the four diamond-lobe collapse mode. They did not consider the two diamond-lobes collapse mode because it rarely occurs in metallic tubes. Johnson *et al.* [27] have recently developed a better method for determining the mean collapse load of tubes collapsing in the diamond folding mode. Two inextensional analyses were undertaken. The first analysis included the work done in flattening the tube and in the forming the diamond-lobe plastic hinges which were assumed to form simultaneously, see Figure 2.10. The second and more realistic analysis was an extension of the first and it included the work done by a travelling

hinge mechanism, see Figure 2.11. The first analysis or stationary theory led them to the following expression :

$$\sigma_m = \frac{\sigma_y}{\sqrt{3}}\left(\frac{t}{D}\right)\left[1 + n.cosec(\tfrac{\pi}{2n}) + \tfrac{(m-1)}{m} n.cot(\tfrac{\pi}{2n})\right] \qquad (2.23)$$

The ratio $\frac{\sigma_m}{\sigma_y}$ in Equation 2.23 is exactly the same as $\frac{P_m}{P_y}$ in Equation 2.22, and n is the number of circumferential diamond lobes and m is the number of axial lobes. The trigonometric terms in the square bracket can be interpreted from Figure 2.10. The second analysis or travelling hinge theory resulted in the following expression :

$$\sigma_m = \frac{\sigma_y}{\sqrt{3}}\left(\frac{t}{D}\right)\left[\frac{\frac{D}{r} - n.cot(\frac{\pi}{2n}) + 1 + n.cosec(\frac{\pi}{2n})}{(1 - \frac{2r}{h_1})}\right] \qquad (2.24)$$

where r is the radius of the travelling hinge (Figure 2.12), h_1 is the length of a diamond lobe in the axial direction.

The study of axial crushing of PVC tubes by Soden *et al.* [28] has revealed that for cases with thicker tube walls ($t/D \geq 0.04$ for the PVC tubes which collapsed into the two diamond-lobes mode), the initial peak buckling stress was independent of the t/D ratio and was taken as the compressive yield strength of the material. Johnson *et al.* [27] tested thinner tubes ($t/D < 0.04$) and found that they buckled into three or four diamond-lobe modes with initial peak stresses lower than the tube's compressive yield stress, the initial failure for these thinner tubes appearing to have been due to elastic buckling. The two-lobe mode appears to be a very stable and repeatable mode of collapse for PVC tubes. Crushing tests by Horton *et al.* [19] with metallic tubes supports such contention by confirming that relatively thin tubes which collapsed into higher number of diamond lobes have a clear tendency for "snapping" to occur during the initial buckling phase, i.e. a sudden steep drop of load-deflection characteristics during the initiation of the collapse process. Such initial "snapping" action is elastic in nature and has the effect of greatly reducing the post-buckling load which is a plastic behaviour.

Square or rectangular tubes

Much work has also been done on square or rectangular tubes since in the transport industry, sheet metal structures are usually of rectangular cross-sections, e.g. car bodies, railway coaches etc. [12, 29-32]. The static load-deflection characteristics for metallic square tubes has a similar pattern to that of cylindrical tubes and a common collapse mode is shown in Figure 2.13. Pugsley [12] has compared the static mean post buckling load for a square tube (Equation 2.25) and a cylindrical tube (Equation 2.26) :

$$\text{For square tubes } \frac{P_m}{P_y} = 3.75\phi \qquad (2.25)$$

$$\text{For circular tubes } \frac{P_m}{P_y} = 5\phi + 0.03 \qquad (2.26)$$

where ∅ is the solidity ratio as previously introduced in Section 2.2.3 and was proposed as a means of comparing the mean load for tubes having different cross-sections. It seems clear that for a fixed ∅, circular tubes have an advantage in the mean resistance and hence energy absorption for a given shortening. Tubes with rounded corners have been shown to behave somewhere in-between Equation 2.25 and 2.26. Test results have also shown that longitudinal stiffening (by reinforcing an internal stringer on the mid-side of each tube wall for the whole tube length) has approximately the same effect as rounding the corners and increased Equation 2.26 by 20% [12] to :

$$\frac{P_m}{P_y} = 6\phi + 0.04 \qquad (2.27)$$

Equation 2.27 was meant for coach-like tubular structures which are actually internally stiffened square tubes. Such coach-like tubular structures were also used by Macaulay and Redwood [29] for representing the small scale model railway coaches in impact tests. The dynamic behaviour of a tubular structure is quite different from the quasi-static one, due mainly to the effects of the strain rate on the yield strength of the material and the longitudinal inertia of the tube. This will be addressed later in Section 2.3.7.

Reid and Reddy [33] have compared the axial crushing performances of rectangular and square tubes and found that the rectangular tubes (with an aspect ratio of 0.5) are relatively unstable and often failed in a global Euler buckling mode, but otherwise they provide about 20% higher mean crumpling load than a square tube with the same periphery dimension, i.e. same weight. One way of stabilizing the rectangular tubes is to fill them up with polymeric foam.

Stiffened tubes

A summary of test results by Jones in [17] has highlighted that the addition of a small number of external stringers to a circular tube longitudinally has a bigger effect on reducing the permanent axial deflection than increasing the *T/D* ratio of the stiffened tubes. *T* is the stringer protrusion on the external tube surface and *D* is the mean diameter of the tube, the stringers have the same thickness as the tube wall. Whereas the effect of increasing the number of internal stringers causes the deformation mode to change from a modified axisymmetric ring mode to a double concave shape. Jones [17] also commented that the axial plastic collapse behaviour is modified by the addition of stringer stiffening on the inside or outside surfaces of square tubes. A value of *T/c* (where *T* if the stringer protrusion and *c* is the side length of the square tube) may exist below which there is little improvement in the energy absorbing capacity of the thin-walled tubes with four stiffeners (one on each tube wall). However, he cautiously remarked that more experiments are required to confirm this observation and to better understand the behaviour for a larger number of stiffeners on square tubes. Stiffened tubes have been used quite extensively for impact tests since they bear close resemblance with actual vehicle structures [12, 29, 30, 32].

Conical tubes

Mamalis *et al.* [34] have investigated the crumpling behavior of conical PVC tubes and found that for a particular thickness, the tubes collapsed at rising load-deflection characteristics with a 2-lobe diamond mode initiating at the smaller ends progressively spreading to a 3-lobe diamond mode at the larger end. This was not surprising since the smaller end has a larger *t/D* ratio than the larger end and one would expect the smaller end to collapse with a smaller number of diamond lobes than the larger end. Furthermore, the stiffer section modulus in the larger end together with the formation of more plastic hinges (due to more diamond lobes) would demand a higher collapse load than the smaller end. In reference [35], it was found that if a tube wall is sufficiently thick, collapse is initiated at the smaller end with axisymmetric-ring collapse mode and spread along the tube length to change to a diamond lobe collapse mode.

2.3.3 Other forms of loading configurations for tubular components

Other loading modes on tubular structures with plastic deformation have potential as energy dissipating systems.

Uni-axial tension

This is the simplest type of energy-absorber and involves the uni-axial plastic extension of ductile wires, strips or tubes. According to Thornton and Magee [21], the maximum energy that can be absorbed per unit mass prior to necking, E_s^T, takes the form :

$$E_S^T = \frac{\sigma_u \varepsilon_u}{\rho(1+\varepsilon_u)} \tag{2.28}$$

where σ_u and ε_u are the ultimate tensile stress and strain respectively and ρ is the density of the tension element. Equation 2.28 agrees well with their experimental results and they also employ it as a criteria for the ranking material for use as energy absorbing media [21]. The main advantage of tensile deformation is the insensitivity to the actual load direction. The energy absorbing stroke of such a device is however limited by ε_u of the material, and would be catastrophic once such failure occurred.

Lateral compression or flattening of cylindrical shells

Thin walled tubes can be crushed laterally such that the cross-section becomes flat. A single tube of length L with a circular a circular cross-section of diameter D, crushed between flat parallel platens with a reduction in platen separation δ, gives the typical load-deflection curve shown in Figure 2.14 [5]. Without considering strain-hardening, the crushing load P_L is approximated by :

$$P_L = \frac{\frac{4}{\sqrt{3}}\sigma_y t^2 L}{D\sqrt{[1-(\delta / D)^2]}} \tag{2.29}$$

Tubes can also be arranged in arrays. If these are stacked in layers such that tubes in alternate layers are at right angles to each others, with the tubes in each layer at about one tube diameter apart, deformation is uniform along each tube and behaviour is identical to that for a single tube. If they are wider apart then the deformation is concentrated at the points of contact and the overall energy dissipation efficiency is considerably reduced. If however the tubes are closer together the lateral expansion is restrained and if the tubes are not initially touching each other, the tube array could absorb up to three times the energy of a similar number of single tubes [5]. A Typical load-deflection curve for the crushing of a three-layer cross tubing array is as shown in Figure 2.15. The array arrangement has upset the smooth load-deflection characteristics offered by crushing a single tube as seen in Figure 2.14. Johnson and Reid [16] compared the energy absorbed by lateral compression and axisymmetric buckling for tubes with the same *t/D* and obtained :

$$\frac{E_L}{E_A} = 0.39\frac{t^{0.5}}{D} \tag{2.30}$$

where E_L is the energy absorbed by lateral compression with a typical stroke of $0.7D$ and E_A is the energy absorbed by axisymmetric buckling with a stroke of $0.7L$. This simple expression underestimates E_L because of the neglect of strain hardening which is an important feature for laterally loaded tubes, but nevertheless it illustrates the superior capacity of the axial loading devices.

Tube inversion

Tube inversion devices consist of a thin tube made with ductile material being pushed onto a 'radiused' die to achieve either internal or external inversion, see Figure 2.16. Energy is dissipated in both plastic bending and stretching in the vicinity of the die. Its effectiveness as an energy absorber depends upon a suitable choice of the fillet radius on the die. If it is too small the tube will tend to buckle as an axially loaded tube, and if it is too large the tube will tend to fracture at the die rather than be rotated to form plastic hinges. The process of tube inversion was analyzed by Al-Hassani *et al.* using the rigid-plastic simplification and obtained the following expression [36] :

$$P_I = K_2 \sigma_y t^{1.5} D^{0.5} \tag{2.31}$$

where K_2 is approximately 7.5. Note the similarity between 2.20 and 2.31. Tube inversions were widely discussed in connection with the idea of collapsible steering columns [2] but shortcomings such as difficulties in securing axial loading, have directed attention to other devices. A typical load-deflection curve for a tube inversion procéss is shown in Figure 2.17. A tube inversion process has a typical stroke of 95% of the tube length and also a comparable mean collapse load to the axial crumpling of

the tube and hence its excellent specific energy absorption performance makes it a very attractive option for energy absorbers.

Plastic bending

For energy absorbers which utilize plastic bending there is frequently a mechanism which converts other types of loading into bending. A simple device is the W frame, first demonstrated by Rawlings [37] and shown in Figure 2.18. When compressed from the ends this has a load-deflection characteristics as shown in Figure 2.19.

Ductile strips can be bent by pulling them through a four-roller device as shown in Figure 2.20. The strip goes through cyclic bending and straightening actions. Such a device is likely to be massive but can be incorporated into a componènt which serves other purposes [5]. The load per unit width is approximated by :

$$P_B = \frac{4\sigma_y}{\sqrt{3}}\left\{t - 2D\left[\sqrt{\left(1+\left(\frac{t}{D}\right)\right)} - 1\right]\right\} \qquad (2.32)$$

for each roller, where t is the thickness of a strip and D is the roller diameter [5, 2].

2.3.4 Cellular structures

The behaviour of hexagonal cell structures under post-buckling axial load was investigated by McFarland [38]. This analysis has since been updated by Wierzbicki [39] recently. Such structures can be considered as an assemblage of hexagonal cylinders undergoing axial buckling and hence the usual rigid-plastic theoretical analysis in [38] has shown good correlation with the experimental data. Such a cellular structure has been used for the protection of a nuclear-powered ship [2].

2.3.5 Metal cutting

Metal-forming and metal-working processes involve substantial amount of energy absorption as noted by Johnson and Reid [16]. They mentioned that a perusal of any standard textbooks on the mechanics of metal-processing operations would suggest to a reader devices for plastically absorbing energy and provide mechanics adequate for design calculation. Reference [2] describes a metal skinning device which was design by Kirk [40]. It dissipates energy by pulling a circular rod through a smaller diameter circular cutting too as shown in Figure 2.21. The device was designed for dissipating the energy of an overshooting U.S. Capitol subway train. Clearly many possibilities exist for absorbing energy using metal processing operations such as extrusion, plastic torsion of bars and columns, tube-expansion, billet-compression etc.

2.3.6 Material selection

Energy absorption per unit mass is an important criterion for an energy absorber if it is to be used in the transport industry. As mentioned earlier, the specific energy E_S^T absorbed by tension elements could be expressed by Equation 2.28 [21]. Tests on tension elements have suggested that the density, ultimate tensile strength and elongation were important in the ranking of materials for tensile energy absorption. A simple power law relationship (i.e. $\sigma = K\varepsilon^n$) between the true stress σ and the true strain ε would lead to the following for E_S^T :

$$E_S^T = \rho \int_0^{\varepsilon_u} \sigma d\varepsilon \tag{2.33}$$

where ρ is the density of the material and ε_u is the ultimate tensile strain. At the ultimate tensile stress (where $n=\varepsilon_u$) of the material, the above integral would give Equation 2.28 for E_S^T. Comparison with experimental data showed this equation to be adequate for predicting tensile energy absorption provided the ultimate tensile strength and uniform elongation were known. It is obvious that a material with a large area under the true stress-true strain curve would made a good tension element which implies that a high work hardening rate associated with high elongation and a high tensile strength are required from the material. All these point to the fact that the material has to have sufficient strength and ductility.

The specific energy for axial collapse of tubes E_S^C, regardless of whether the collapse mode axisymmetric ring or diamond, can be empirically expressed as [21] :

$$E_S^C = A\left(\frac{t}{D}\right)^m \tag{2.34}$$

where A and m are experimentally determined constants for each material. No correlation has been found between E_S^T and E_S^C [21]. A material which makes a good tensile energy absorber may not necessary be efficient in dissipating energy as an axially crushed tube. This could be attributed to the different demands on the material in each of the tensile and compression cases. The tension process requires a material to possess sufficient work hardening to counter act the diminishing specimen cross-sectional area. This geometric instability lead to a low energy absorption in a material which had sufficient strength and ductility to demonstrate a high specific energy absorption in situations where the geometric instability does not come into play, such as in axial tube compression [21]. Observing Equations 2.20 to 2.27, it could be concluded that the maximization of specific energy in axial collapse can be achieved by maximizing the tensile strength alone (in this Section we are only concerned with the material properties of the tubes and not geometrical factors). In this case, the elongation would not be significant provided that the ductility of the material was sufficient to allow the formation of plastic hinges and not to fail by fracture. Strain hardening is also thought to be insignificant since the total deformation of a tube was determined by available space rather than the uniform strain.

2.3.7 Dynamic response

In reference [30] and [31], both quasi-static and impact tests were carried out on scale models of bus and railway coaches. These contained cut outs for the windows, doors, wheel arches etc. It was found that in quasi-static tests, the models always failed at the cut out region but in the dynamic tests they failed at the impacted end as long as the cut out portions were within half of the periphery of the models. See Figure 2.22 Similar observations were made in [29] with dynamically loaded square tubes and rods, see Figure 2.23, and also with circular tubes [31]. In reference [31], it was found that tapered circular tubes of up to 20° axial offset produce very similar impact results to parallel tubes. Macaulay and Redwood [29] also observed that oblique impact tests of up to 10° 'non-axiality' on circular tubes made little difference to the results. Geometrical changes in the deformation mode between static and dynamic loading condition are more pronounced for slender rods and thin walled square tubes, but circular tubes have essentially the same mode of deformation in both situations [16].

Enhancement of yield stress at high rate of strain and the longitudinal inertia of the tubes are the two most important factors that divide the quasi-static and dynamic behaviour for structures. The former changes the material properties and the latter alters the mode of deformation. Generally it is the order of magnitude of a strain rate that is important and minor changes in strain rate can be ignored. Some strain rates of practical interest are shown in Figure 2.24.

The implication of designing an impact energy-absorbing device on the basis of its quasi-static loading behaviour is that inertia effects within the device itself are insignificant and so the kinetic energy is considered to be converted into plastic work in a quasi-static deformation mode. When the mass of the body being decelerated is much larger than that of the energy dissipating device, a mass-spring system would be a reasonable representation of their response and a quasi-static approach would suffice. However, if the mass of the body is of the same order as that of the device, stress wave activities can no longer be ignored and quasi-static analysis will not produce the correct deformation profile for the device under the dynamic loading situation.

There are some empirical and theoretical formulae for expressing the relation between the static and dynamic crumpling loads of axially loaded tubular structures. Based on experimental knowledge of the crumpling of circular and square tubes, Pugsley [12] has proposed a simple formula to account for the effect of impact velocity when predicting the dynamic crumpling load of a circular or non-circular tubular structure :

$$\frac{P_d}{P_s} = \left(1 + \frac{V}{15.2}\right) \tag{2.35}$$

where V is the impact velocity in m/s. P_d is the dynamic crumpling load and P_s is the static crumpling load which is the same as P_m in Equation 2.27. So according to Equation 2.35, an impact speed of 15.2m/s would double the quasi- static crumpling load for an axially loaded tube. Equation 2.35 was an empirical expression based on limited experimental data and Pugsley [12] stated that too little was known about the dynamic behaviour of crumpling structures for confident predictions.

Based on experimental observations, Redwood [41] has described that during high velocity impact tests on square tubes, a stress front of magnitude σ is propagated from the impacted end along the tube wall at sonic velocity c and after it has traversed a length of the tube which is equal to the static instability wavelength corresponding to σ, buckling will occur. This buckling is necessarily located near the point of impact. The relation between impact speed V and σ could be expressed as :

$$\sigma = \frac{VE}{c} \tag{2.36}$$

where E is the Young's modulus. At low impact velocity, buckling occurs anywhere within the tube length in the manner as for static buckling because the stress front is not strong enough to cause short-wave buckling and has time to build up after several traverses of the stress wave allowing the tube to be almost uniformly stressed along its length. There is thus a velocity range that divides the static behaviour from the dynamic one. Let t_1 be the time for the compressive wave-front to travel the length of the tube and t_a be the time with which an appropriate unstable buckle reaches a lateral amplitude for buckling to occur [41]. It seems clear that :

- For $t_a > t_1$, the whole length of the tube will be uniformly stressed and low speed behaviour will occur;
- For $t_a < t_1$, higher speed behaviour will occur.

To account for the effect of impact velocity on the mean crumpling load, Macaulay and Redwood [29] proposed :

$$\frac{P_d}{P_s} = n\left(1 + \frac{nKV}{\lambda}\right) \tag{2.37}$$

where P_d is the dynamic load, P_s is the static load, n is a factor depending on the variation of buckle wavelength with velocity, K is a factor dependent upon the variation of material strength with impact velocity, λ is the geometric scaling factor and V is the impact velocity.

More recent approaches to account for the dynamic effects involve the use of constitutive equations which describe the strain rate sensitivity of a material. The one due to Cowper and Symond [42] has been used almost universally in theoretical and numerical studies. This equation may be written in the form :

$$\frac{P_d}{P_s} = 1 + \left(\frac{\dot{\varepsilon}}{S_y}\right)^{\frac{1}{q}} \tag{2.38}$$

where $\dot{\varepsilon}$ is the uni-axial strain rate, S_y and q are experimentally derived material constants. For hot rolled mild steel, S_y is 40.4/sec and q is 5. For aluminum alloy S_y is 6500/sec and q is 4. These conform to the well established fact that mild steel is more sensitive to strain rate than the aluminum alloys. Equation 2.38 could adequately be

applied to a large class of practical structural impact problems, but the situation is less satisfactory for problems with large plastic strains. This is so because the strengthening influence of strain rate on the plastic flow stress of mild steel is greatest for small strains, decreases as the plastic strains increase and is lowest for the strain at the ultimate tensile stress [43]. So Jones [17] has suggested a modification to Equation 2.38 :

$$\frac{P_d}{P_s} = 1 + \left(\frac{(\varepsilon_u - \varepsilon_y)\dot{\varepsilon}}{(\varepsilon_u - \varepsilon_y)S_u + (\varepsilon_u - \varepsilon_y)S_y} \right)^{\frac{1}{q}} \tag{2.39}$$

where $\varepsilon_y \le \varepsilon \le \varepsilon_u$ and ε_y and ε_u are the yield and ultimate tensile strain respectively, S_y and q are the same as in Equation 2.38 and S_u is a material constant evaluated from the strain rate sensitive properties at the ultimate tensile strength of the material. Equation 2.39 is approximate and without proper experimental foundation, and assumes that q is independent of strain.

Equation 2.39 ignores the influence of material strain hardening. Perrone [44] suggested that material strain-hardening and strain-rate-sensitivity effects should be decoupled and the corresponding constitutive equation expressed in the product form :

$$\frac{P_d}{P_s} = f(\dot{\varepsilon})g(\varepsilon) \tag{2.40}$$

where $f(\dot{\varepsilon})$ could be the right hand side of Equation 2.38 or 2.39 and $g(\varepsilon)$ caters for strain hardening. A form of Equation 2.40 was suggested by Rawlings [15] :

$$\frac{P_d}{P_s} = \left(1 + \left(\frac{\dot{\varepsilon}}{S_y} \right)^{\frac{1}{q}} \right)(1 + \psi\varepsilon) \tag{2.41}$$

where ψ is a material constant to account for strain hardening and the first bracketed term on the right hand side is the same as Equation 2.38.

2.4 Structural crashworthiness for rail vehicles

2.4.1 BR database on structurally significant accidents

British Rail Research (BRR) maintains an accident database covering all structurally significant train accidents (involving structural strength, i.e. excluding fires and a miscellaneous category) occurring after 1973. The update and statistical analyses of this data has been an ongoing process with frequent reports published [45-47]. These reports contain the results of statistical analyses of the past accidents in a decade and such analyses greatly assist BR in formulating the design input (such as identifying the most common loading mode on those coach bodies involved in accidents, selecting the appropriate impact velocity for structural crashworthiness design with maximum

benefit in enhancing passenger and staff safety, the accident type that cause the worst casualties etc.) for future rolling stock. These statistical analyses for structurally significant accidents have been an integral part of BR's crashworthiness research and development programme.

In the references [45-47], casualties are separated into three categories in line with the definition provided in the Notice of Accidents Order : (1) Fatalities; (2) Serious injuries; (3) Minor injuries. Serious injuries are those that require hospital detention for treatment and minor injuries are minor cuts and bruises but excluding shock. Note that these are entirely different from the Abbreviated Injury Scale (AIS) widely used by the medical professions which will be discussed later in Section 2.6.1. The direct causes of fatalities and serious injuries can be classified as [47] :

- Loss of survival space;
- Ejection from the vehicles, usually through broken windows;
- Secondary impact (passenger interactions with the interior fittings or other passengers).

The latest study of the BR accident statistics is reported by Lewis and Rogers [47], which includes the structurally significant accidents that occurred during the period 1984 to 1993. The following accident types were identified from a pool of 1424 accidents involving 1797 trains :

- End-on collisions : Passenger and freight trains.
- Side-on collisions : Passenger and freight trains.
- Collisions with buffer stops : Passenger trains only.
- Collisions at level crossing : Passenger and freight trains.
- Derailments : Passenger trains only.
- Miscellaneous : Collisions with large, heavy objects such as rail crane.

Some of the major conclusions in reference [47] are as listed below :

- 82% of reportable accidents subject the coach(es) to some form of longitudinal loading confirming that the principal design effort for improving the overall vehicle crashworthiness should be directed towards longitudinal structural integrity.
- 63 out of a total of 91 fatalities (about 70%) and 220 out of a total of 372 serious injuries (about 60%) are caused in end-on collisions. The other fatalities and serious injuries are predominantly due to derailments (constitute 24% of total fatalities and 12% of total serious injuries) and a single accident in which a crowded ten-coach train hit some hydraulic buffer stops in Cannon street station with overriding occurring between the 5th and 6th carriages (2% of total fatalities and 15% of total serious injuries). See Figure 2.25a and 2.25b for the casualty distribution. Hence, maximum benefit in terms of reducing fatalities and serious injuries is achieved by concentrating the crashworthiness development effort on end-on collisions.
- Having identified that the main target of BR crashworthiness improvement programmes is to reduce the casualty rate in end-on collisions, it is useful to identify the characteristics of this type of accident. Almost 98% of all end-on

collisions occurred below 40mph and prevention of vehicle overriding is the most important single factor in reducing passenger and crew fatalities. The probability of fatal injury being 38 and 27 times greater for passenger and crew respectively if overriding occurs. Vehicles built to current the International Union of Railways (UIC) loading specifications and vehicles with projecting noses such as Class 37, 40, 45 etc. locomotives offer cab occupants more protection then non-UIC flat fronted vehicles. Note that a vehicle front with a projecting nose would collapse with a rising load-deflection characteristics due to its conical structural shape.

- Derailment is generally known as a high speed phenomena (see Figure 2.26.). As suggested in Figure 2.25a and 2.25b, next to end-on collisions this type of accidents caused the second largest proportion of fatalities and serious injuries. Loss of survival space and ejection from the coaches are the principal causes of casualties. Serious and fatal injuries tend to be confined to those incidents resulting in trains splitting, overturning or "jack-knifing"; few casualties occur when derailed trains remain upright and in line which allows the kinetic energy to be absorbed in a controlled manner.

2.4.2 BR specifications on the structural loading requirements for trains

The origin and its rationale

The longitudinal loading requirements (proof loads, i.e. loads to be sustained without permanent deformation) at various positions of the coach is explicitly incorporated in a UIC pamphlet and is illustrated in Figure 2.27 [48]. The values used were determined by the ORE B7 Committee after static and dynamic tests involving 12 main-line coaches and after a study of 15 accidents to similar vehicles. The longitudinal loading specification seeks to achieve two aims :

(1) In service, the provision of a sufficient margin on normal loading (due to coupling, buffing) so that some degree of heavy shunting or even abuse (fly-shunting) is possible without damage.

(2) In accidents, the protection of passengers and crew and the limiting of damage to the vehicles.

In an attempt to encompass both of the above objectives, rather high loads have been specified as seen in Figure 2.27. In designing for accidents, however, the 'no permanent deformation' becomes difficult to apply and impossible to justify, since a controlled deformation in the coach ends would enhance the protection of the passenger compartment and limit the overall damage to the coach [48]. A clear distinction is required between proof loads, which could be used to cover extreme service conditions without a reduction of serviceability, and the design requirements for unplanned collisions.

An alternative rationale

The traditional "the stronger the better" philosophy using proof loads to specify the end load requirements for rail vehicles was reviewed in the early eighties [49]. In reference [48], Scholes presents a strong case for an alternative philosophy based on the ability to absorb energy in a controlled manner during train crash situations. He further proposed a three-stage rail vehicle crashworthiness design based on a progression of severity (for a collision between two similar vehicles), in which the maximum impact velocities increase by a factor of 2 :

Stage	Maximum velocity (m/s)	Maximum longitudinal force	Acceptable responses
1 : Heavy Shunt	2.5	P (to be set by the designer)	Energy absorbed by the coupling system without loss of future serviceability (self-recoverable).
2 : Light Accident	5	$1.25P$	Energy absorbed irreversibly by the coupling system within a prescribed stroke and an anti-climbing device is to engage.
3 : Heavier Collision	10	$1.5P$ for vehicle ends, $2\text{-}2.5P$ for passenger compartments	Energy absorbed irreversibly by the vehicle-end structures within the interfaces of the colliding rakes of trains.

Table 2.1 : The acceptable responses for the collision between two similar crashworthy vehicles, as proposed by Scholes. After [48].

The main assumption made is that the bogies (which usually constitute one third of the whole vehicle mass) are flexibly mounted and that the effective mass for calculating the energy dissipation in stages 1 and 2 comprises the vehicle body only (i.e. excluding the bogies). However in stage 3 the energy to be dissipated involves the whole train. Note that similar progressive-severity responses for the collisions of crashworthy rail vehicles was proposed earlier by Pugsley [12] in a more conceptual form. Table 2.1 is only a conceptual proposal without detail quantitative specification for the force P, the energy absorbed or deformation. However, it clearly specifies the collapse load of passenger compartment must be at least 30% higher than the vehicle end structures, The vehicle end structures could thus be viewed as crumple or crush zones. Past experience with accident vehicles also has suggested that only the end structure would suffer any substantial deformation. Note also that in stage 2 (and thus stage 3) the proposed engagement of an anti-climbing device simply emphasizes the importance of the prevention of overriding of vehicles.

Eight years after the publication of reference [48], Scholes and Lewis have demonstrated the feasibility of the proposed design philosophy for crashworthiness through a series of static and dynamic tests on actual rail vehicles [50]. Static tests included the experimental crushing of three vehicle ends of unmodified BR vehicles and a modified vehicle end designed to conform to a proposed standard. Only one

dynamic test was conducted and it was a combined effort by several European Railway Operators presided by the ORE B7 committee. The dynamic test involved a fully instrumented collision between one moving coach and another identical stationary coach and the vehicle ends at the impact interface were of a similar crashworthy design as the one proposed by BR. The unmodified vehicle ends tested have been designed to follow the UIC standard for end loading but their crushing test results confirmed the need for modifications to suit the acceptable structural response beyond that required to satisfy proof loads. Hence a new design specification was proposed and applied to a vehicle of 24 tonne tare mass for the purpose of experimental verification. The acceptable responses for the various severity level of collisions with the new design are tabulated in Table 2.2 [50] :

Stage	Maximum velocity (m/s)	Maximum acceleration (m/s^2)	Acceptable responses
1 : Heavy Shunt	4	30	Energy dissipated over 150mm in drawgear without loss of serviceability.
2 : Light Collision	8	50	Anti-climber engages. Energy dissipated in self contained easily replaceable device.
3 : Heavy Collision	16	60	Energy of 1MJ absorbed by structural collapse over a total stroke of no more than 1m. Damage restricted to vehicle end.
4 : Higher-speed Collision	>16	Not defined	Damage will result to passenger compartment can be minimized by making full use of structural energy absorption.
---	12	30	Maximum amount of structural integrity while absorbing over a total distance of no more than 1m.

Table 2.2 : Idealized collisions and responses with the new crashworthy design vehicle ends. After [50].

Table 2.2 is basically the same as Table 2.1, except that actual numerical figures have been assigned to the appropriate columns. Note also that the deformation at various stages has been specified. The new specification explicitly requires the structure to absorb 1MJ within a metre of deformation so as to mitigate any collision below the impact velocity of 16m/s. To satisfy the stipulated structural responses in Table 2.2, the load-deflection characteristics of the proposed vehicle end structure must take the form shown in Figure 2.28a, and the completed prototype of the designed end structure is shown in Figure 2.28b. Scholes and Lewis [50] have assumed that the vehicle body weighing sixteen tonnes is resiliently mounted on the eight-tonnes bogies, allowing both to achieve maximum accelerations at different times and so only the body mass was taken into account when determining the forces (in Figure 2.28a) based

on the stipulated acceleration levels. However, in calculating deformation (in Figure 2.28a) the total kinetic energy of the vehicle including that of the bogies was used. Quasi-static crushing tests (full face and overriding) of the prototype structures showed slightly higher structural collapse forces than the design values and the expendable GRP tubes (see Figure 2.28b) did not meet their specified requirements; further sourcing of replaceable energy absorbers was required. There was no failure of principal structural joints for the crashworthy prototype structure which was an improvement over the unmodified end structures since fractured joints absorbed little energy [50].

The vehicle end structures for the full scale dynamic collision test were of similar design except that higher loads were specified since the tested vehicles were of heavier build. The prototype is shown in Figure 2.29a (grafted on one of the tested vehicles) and the load-deflection characteristics (both designed and experimental) are shown in Figure 2.29b [50]. Dynamic collapse forces were approximately 15% higher than design values with displacements similarly lower. The full scale collision test has fully validated the design philosophy for a "one coach to one coach" collision, in that the collision energy was absorbed under graduated and controlled conditions with the cab structure collapsing in the prescribed manner.

Following the static and dynamic testing of crashworthy end structures, BR issued a mandatory specification for structural design which specifies vehicle performance beyond proof loading : All passenger carrying vehicle ends must absorb a minimum of 1MJ over a collapse distance of no more than 1m and the collapse force not exceeding 3MN for multiple units [51].

Another important conclusion drawn from reference [50] is that the UIC specification of proof loads on vehicle's end walls imparts sufficient longitudinal strength to the vehicle body and offers reasonable protection to passengers and crew in an end-on collision, but more can be achieved by specifying collapse distance and thus the required energy absorption.

The full scale collision test in reference [50] has successfully demonstrated the feasibility of the proposed design philosophy based on energy absorption, but it was done with a "one vehicle to one vehicle" collision. The behaviour of vehicles in colliding rakes and how such behaviour alters the energy distribution among the interfaces has to be known in order to confirm whether the design philosophy may be applied universally in the railway environment. This is discussed next.

2.4.3 Dynamic behaviour of vehicles in rakes

Train crashes are energy intensive events. The kinetic energy involved in a train collision is typically 16-20MJ as compared to 0.09-0.14MJ for motor-car collisions. How the large amount of kinetic energy should be distributed as energy is absorbed among all the interfaces within 2 colliding rakes of trains is of great interest to rail-vehicle designers. The concept of absorbing impact energy in a predetermined manner along the entire train's length as it slows down is known as Energy Management. Two distinct philosophies of energy management have been developed [52] :

- Energy dissipation is spread as evenly as possible along the entire length of the colliding trains.
- The leading vehicles are designed to absorbed most of the collision energy.

The first strategy is aspired to by BR, and basically requires each coach to look after itself and not to influence the neighbouring coaches during collisions. This is only possible if there is a gap between adjacent coaches with such a size that the time for a trailing coach to close the gap coincides with the time taken for the completion of crushing by the front vehicle. Hence the collision energy is absorbed by a series of sequential and independent collisions of the coaches. See Figure 2.30 [52].

The second approach has been dominated by studies in SNCF involving the TGV, due partly to the massive power cars with projecting noses in the leading end of these trains and also partly to the articulated bogies at all intermediate interfaces which compact the inter-vehicular distances, thus limiting the scope of sequential collisions [52]. With these constraints, the TGV has been developed with a capability of absorbing as much as 6MJ at the front end and first interface. The main characteristics of this approach is that the leading vehicle would suffer severe deceleration pulse and endanger its occupants, but passengers in the remainder of the train will be subjected to much less injurious secondary collisions [53].

As noted in reference [50], the high cost and low number of vehicles in the railway industry (relative to the automotive industry) makes iterative testing for achieving a specified crashworthy behaviour impractical. Hence great emphasis has been placed recently by many railway operators on the development of non-linear and large deflection analysis capabilities.

Computer modelling for an actual structural collapse of a rail vehicle body in a given impact scenario is a formidable task which approaches the capability limits of the most powerful and versatile computer software codes currently available [54]. Many countries (railway operators) have been using finite-element (FE) computer modelling to predict load-deflection characteristics for body structures. Initially these models had to be 'tuned' using feedback from experiments, but knowledge and experience in dealing with structural-joint collapse and other buckling behaviour have now built sufficient confidence for the FE models to make reasonable blind predictions [52].

At the other end of the modelling spectrum is the use of mass-spring models for simulating the crashes of two rakes of trains. Rail vehicles are modelled by single masses (representing the inertia properties of the vehicles) connected by non-linear springs (representing the crush zones) and the problem is to solve a set of simultaneous second order ordinary differential equations. The difficulty lies in the fact that spring stiffnesses are not a linear function of displacements and unloading of a spring takes a different path in the load-deflection curve. The main advantage of these models is that they are economical to run. The accuracy of the models depends on the knowledge of the non-linear collapse characteristics of the springs (i.e. the crush zones) which is usually obtained by a separate structural analysis or by a full scale test.

The recent development of commercial software codes for the macroscopic simulation of rail vehicle behaviour in rakes (mass-spring models) and the microscopic simulation of the actual collapse of a rail vehicle end structures (FE models) has been reviewed by Tong [55] and Carney [54]. DYNA3D and PAMCRASH are the two most popular non-linear FE codes in use nowadays for crashworthiness analyses and they are used almost universally by the transport industry.

A major part of the content of this thesis is directed towards the use of non-linear mass-spring models for simulating the behaviour of vehicles in rakes. It is useful to see what others have done and discovered in this aspect of rail vehicle crashworthiness.

Sutton and Lewis [56] applied the Continuous System Modelling Program to conduct a study of the major parameters affecting rail vehicle buffing loads using the characteristics of the BR Mark III coach as a datum. The code allows the user to define a dynamic system in terms of the differential equations governing its motions and then formulates and solves the simultaneous set of equations of motion using one of a number of numerical integration schemes. Their main conclusions are summarized below [56] :

- The peak impact force is governed by the characteristics of the impacting vehicles (e.g. mass, coupler type etc.) and impact velocity.
- When a heavy vehicle collides with a rake of lighter vehicles, the force between the first and second vehicle is lighter than the impact force.
- In collisions involving a rake of vehicles with a heavier vehicle at its head, the peak force between the first (heavy) vehicle and the second is less than those at subsequent interfaces.
- The simple rubber-stack coupler spring generates a much higher buffing force than the constant force spring and Oleo 5SC type coupler. This point will be re-addressed later in Section 2.4.4.
- For collisions of identical rakes of vehicles, the computation suggested that although the majority of the permanent deformation occurs adjacent to the point of impact, some will occur at subsequent vehicle interfaces along the rake.

By using non-linear mass-spring models, Ohnishi *et al.* [57] have also performed a series of numerical parametric studies on the impact behaviour of rakes of trains. The trains were composed of homogeneous coaches, i.e. all coaches shared the same physical properties. The parameters they chose to studied were : the mass of the coach, the coefficient of dry friction for the wheel/track interface, the number of coaches in a rake, the impact velocity and the magnitude of the spring (i.e. the crush zone) collapse load. Similar load-deflection curves to those shown in Figure 2.28a were used and all their models adopted a symmetric impact configuration which consisted of a rake of N moving coaches hitting another stationary rake of N coaches. They did not specify the codes they used for the solution of the set of non-linear second order equations and did not disclose the coupler characteristics. Their main conclusion was that within the range of parameters considered, the number of coaches in a rake and the dry frictional effect could be safely ignored as they have little effect on the final impact energy distribution along the two colliding rakes. Impact velocity, coach mass and the spring collapse load were the main parameters governing the behaviour of coaches in rakes during an impact [57].

Revan [58] was the first to derive the theoretical tuned gap (previously mentioned) between adjacent coaches :

$$x_g = \frac{MV_0^2}{8P_c} \tag{2.42}$$

where M is the coach mass, V_0 is the impact velocity, P_c is the plastic collapse load for the rigid perfectly plastic spring, x_g is the optimum gap for the given impact configuration. It can be seen that all the physical variables that appear on the right hand side of Equation 2.42 are the important parameters discovered by Ohnishi *et al.* for their mass-spring models. Revan has performed an extensive parametric study for a rake of four moving coaches hitting another similar stationary rake, using the non-linear FE code DYNA3D to create the mass-spring models. Each lump mass in his models is 35 tonnes (typical for a multiple unit coach) and the spring characteristics is as shown in Figure 2.31. Note that the impact interface has a larger dissipative capacity of energy than the intermediate interfaces since Revan has predicted the impact interface would absorb twice as much energy as the intermediate interfaces. The main conclusion he drew was [58] :

- The idealized collision behaviour of vehicle rakes, where each vehicle independently absorbs its own energy in a sacrificial zone, is achievable if the gaps between coaches in the two rakes are set to a specific value determined by Equation 2.42. Such gaps are equivalent to very loose coupling systems which don't exist in practice. One of the effects of having couplers between coaches is to modify the even distribution of energy with the consequence of over-crushing the impact interface. An ideal coupler should breakaway as early as possible during a collision so as not to upset the even distribution of energy along the colliding rakes and this can be achieved by designing the couplers to shear-off at a prescribed force. Once a coupler breaks away, the trailing coach is required to close the remaining inter-vehicular gap before hitting the front vehicle structurally.

The following conclusions are based on models incorporating breakaway couplers [58] with the inter-vehicular gap :

- It is essential that the coupler breakaway force is less than the vehicle end collapse load.
- The inter-vehicular gap of a train could be tuned to a particular impact velocity according to Equation 2.42, but at low velocities it would be too large. However this is offset by the lower amount of energy to be absorbed and essentially a fairly even energy distribution along the rake is achieved with no collapse beyond the crush zone. At higher impact velocities the leading interface tends to be over-crushed and the damage throughout the rakes is higher since more impact energy has to be absorbed.
- An increasing crush characteristic is beneficial to the distribution of energy absorbed in the rakes, but only if there is adequate margin between the initial collapse load and the coupler break-away force.

- An initial 'spike' on the collapse load-deflection characteristics, typical of current aluminum alloy body designs, causes disruption to the timing of the sequential collisions but does not significantly affect the concept of each vehicle absorbing its own energy.
- Hydraulic couplers, with some energy absorption, can be incorporated into vehicle rakes with no detrimental effect to the overall collision performance at higher speeds. However they must have a breakaway device designed to limit the load they can withstand.
- The longitudinal flexibility of bogies has a negligible effect on the collision behaviour.
- A single heavy vehicle, second in the rake from the impact plane, disrupts the timing of the collisions if the gaps are left unchanged. If sufficient energy absorption is provided at the same load level as the interface in front of the heavy vehicle, no collapse beyond the crush zone occurs, even if the gaps are calculated on the basis of the lighter vehicles.

Chatterjee and Carney [59] have extended Revan's work, and in their prolific study, the following parameters were investigated for rake behaviour :

- Number of coaches in the impacting and impacted rakes;
- Impact velocity;
- Gap size between coaches in the impacting and impacted rakes;
- Yield ratio of coaches in the impacting and impacted rakes;
- Crush zone yield force of coaches in the impacting and impacted rakes.

There was a need to differentiate between impacting and impacted rakes in some of their models because collisions of non-symmetric rakes were modelled. Yield ratio is defined as the ratio between the yield force of the passenger compartment to that of the crush zone, both of which are constant. They also used DYNA3D for their non-linear mass-spring analyses, but no coupler or damping action was modelled (Revan's models had 'small' dampers for enhanced numerical stability). The main findings of their work in [59] are :

- Instead of having large crush zones in all train compartments, each designed to resist large amounts of energy, crush zone length can be reduced to a calculated minimum and designs implemented to distribute the remaining energy to crush zones in other compartments along the rakes. The passenger compartments must be stronger than the crush zones for this concept to work. A yield ratio of 1.5 proves very effective in distributing the crush in the rake.
- The inter-vehicular gap plays an important role in the impact event. A gap greater than or equal to the tuned value results in a significant reduction in the plastic deformation sustained by the lead vehicle resulted in a more even distribution of plastic deformation along the colliding rakes.
- For symmetrical impacts, no effect on energy distribution along the colliding rakes should be expected if the gap size of the trains is greater than the tuned gap and unloading is suppressed. For gap sizes greater than the tuned gap, the two vehicles in the front interface have sufficient time to complete their impact and unload (if allowed) thus creating a velocity gradient between them (i.e. they are separating).

This happens whilst the second vehicle in the rake is still approaching the front one. Since there is a velocity gradient between the two vehicles in the front interface, they will experience another smaller scale 'follow-up' impact activated by its trailing neighbour once the gap has been closed up. Such follow-up impacts would not be possible if the coefficient of restitution was exactly zero.

- For a given crush zone length, increasing the yield force results in a more concentrated energy dissipation at the impact interface (the leading interface) and less dissipation in the intermediate interfaces. Given a specific yield force level, an increase in crush zone length also tends to increase the deformation and energy dissipation in the impact interfaces. These tendencies are most pronounced when the inter-vehicular gap is less than the tuned value.
- When two trains containing an equal number of identical vehicles with different gap lengths collide, more energy will be dissipated in the rake containing the larger gaps (i.e. the longer train).
- When rakes with different numbers of coaches and different masses collide, more energy is dissipated in the larger rake. Impacting coaches suffer essentially equal damage, but the following coaches in the smaller rake suffer less plastic deformation than those in the larger rake.
- When two trains with different yield ratios collide, the train with the lower yield ratio will dissipate the most kinetic energy. This is applicable only if the passenger compartments have been infringed (i.e. the crush zones fully 'consumed').

Note that Revan [58] and Chatterjee and Carney [59] have modelled train collisions with one-dimensional mass-spring models which implies that the possibilities of vertical mis-alignment (overriding) and the lateral mis-alignment (jacknifing) between coaches have been ignored. Also the springs represented two crush zones linked back to back, i.e. two identical non-linear springs connected in series, so the characteristics of the spring are actually the combined characteristics of the front coach end, the couplers, the gap and the trailing coach-end in an interface. This technique of using averaged characteristics in an interface is not applicable when the connected vehicles have different parameters.

In reference [53] Chatterjee and Carney continued their parametric studies and arrived at the following conclusions :

- The ideal gap size for deformations and accelerations have apparent conflicting requirements. The gap size that minimizes the deformations maximizes the duration of the accelerations and visa-versa.
- The duration of crash pulses reduces with increasing yield forces because the collision events become more intense with larger quantities of energy being dissipated per unit time.
- For symmetric collisions, the number of vehicles in a rake has no significant effect on the duration of the acceleration pulses.
- The duration of the crash pulses may be significantly longer when the impact velocity is higher.

The advantages of adapting a crash energy management approach over traditional design (the stronger the better!) have been evaluated numerically by Tyrell *et al.* in

reference [60] for high velocity collisions (35mph to 140mph). Mass-spring analyses were carried out by a FORTRAN computer program. Their models have stronger cabs and first intermediate interfaces with larger dissipative energy capacities than the subsequent interfaces, which seem to be a mixture of what BR and SNCF adapt. They applied the deceleration pulses derived from their mass-spring models to a forward facing occupant model as shown in Figure 2.32 and arrived at the following summary results :

Speed	Conventional design			Crash energy management design		
	Fatalities due to loss of survival space	Fatalities due to secondary impact	Total predicted fatalities	Fatalities due to loss of survival space	Fatalities due to secondary impact	Total predicted fatalities
140mph	76	0-4	76-80	67	0	67
110mph	25	0-5	25-30	13	0-1	13-14
70mph	2	0-5	2-7	2	0-1	2-3
35mph	0	0-5	0-5	0	0-1	0-1

Table 2.3 : Predicted fatalities for conventional and crash energy management designs. After [60].

Fatality predictions were based on a probability curve expressed in terms of 'Percent-life-threatening injuries against head injury criteria (*HIC*) as shown in Figure 2.33. *HIC* can be computed from the deceleration-time history of an occupant's head during a secondary collision and this will be re-addressed later in Section 2.5.2. It isn't clear what method or code they used for simulating the occupant kinematics during collisions.

2.4.4 Couplers

A coupler is an essential component in any crash energy management scheme and it has always been an integral part of BR's crashworthiness programme. Many types of energy absorbing principle have been employed by modern couplers, e.g. as Rocholl has noted [61] :

- by radial expansion/contraction of a tube;
- by compressing a metal tube axially;
- by hydraulic principle;
- by hydro-elastic principle.

All of the above are shown in Figure 2.34 [61]. It should be noted that the load-deflection performance of hydraulic and hydro-elastic systems are velocity sensitive.

Until recently, little consideration has been given to couplers in BR beyond the requirement to satisfy the required proof loads [62]. In collision conditions, loads considerably in excess of proof are transmitted through the coupler with resultant damage to the underframe - including the coupler mounting. This often leads to local bending of the underframe with a subsequent tendency for vehicles to override. It has been established that reducing the peak loads arising from heavy coupler contacts would reduce the likelihood of overriding [62].

Scholes has highlighted in reference [48] that the proposed structural crashworthiness design concept to substitute the traditional 'the stronger the better!' philosophy must be capable of providing a sufficient margin on normal-service loading so that some degree of shunting or even abuse is possible without any loss of serviceability to any component. In reference [50] the maximum impact velocity of 4m/s has been set for such requirement with the body acceleration not exceeding 3g. This implies that couplers must be able to withstand minor shunting impacts in a self-recoverable manner up to the velocity of 4m/s with a fairly constant force and this requires energy absorption.

On the other hand, Revan [58] has found from the studies of rake behaviour that couplers can upset the ideal energy distribution along colliding rakes, thus identifying an important need for the couplers to break away once a prescribed limit force is reached. This is also to protect the underframe from excessive loading [62]. It is also desirable that during higher velocity impacts (greater than 4m/s) the couplers absorb as little energy as possible before breaking away, thus minimizing their effects on the overall energy distribution along colliding rakes [58].

The ideal candidate to fulfill all the above specifications is a hydro-pneumatic coupler or a hydro-elastic coupler. These velocity sensitive couplers are well established in their ability to absorb energy for low velocity collisions and at the same time produce a smooth and fairly constant force. In high velocity collisions, the force rises quickly and reaches the breakaway limit rapidly, thus absorbing only a limited amount of energy prior to breaking away. New crashworthy vehicles will be installed with hydro-pneumatic couplers supplied by Oleo Pneumatic Ltd. The breakaway force for 35 tonne vehicles is set at 1.2MN and the selected Oleo couplers are capable of absorbing 0.07MJ per coupler for a 4m/s collision. A detail description of this type of coupler is given in Section 4.3.1 of Chapter 4.

2.4.5 Full scale impact tests of a moving five-coach rake to an identical stationary five-coach rake

BR conducted two full scale collision tests on 24th and 28th October 1994. These were five-to-five collisions with a closing velocity of 11km/h (3m/s) and 60km/h (the metric equivalent of 40mph) respectively on a straight track. Redundant Mark I vehicles were used modified with a crashworthy end structures and Oleo couplers, and each vehicle was ballasted to 35 tonnes. The couplers were designed to shear off at 1.2MN and then push back into an allocated space in the underframe structure allowing the ribbed anti-climber pads of adjacent coaches to engage. One such vehicle is seen in Figure 2.35 in its pre-test condition [63].

For the slower velocity test, the collision energy was absorbed by the Oleo couplers with no structural damage to the vehicle at all. The peak acceleration experience by the leading vehicles of the two rakes was 1.6g. The maximum compressive force in the couplers at the impact interface was 0.95MN and this was progressively reduced down each rake to 0.12MN at the last interface. A scheduled test with a collision velocity of 15km/h (4m/s) was not attempted because the Oleo couplers didn't perform as expected; the supplier was approached and rectifying action was forthcoming [63].

For the high velocity test, full validation of BR crashworthiness philosophy was achieved. The collision energy was distributed along the vehicle interfaces of each rake. The maximum permanent deformation following the collision was slightly more than 1m shared between the two impacting vehicles (0.5m per vehicle), there was no derailment and the anti-climber had effectively engaged without vehicle overriding. There was good agreement between one-dimensional mass-spring models and test indicating the usefulness of such models in predicting rake behaviour. The models, if used without strain-rate enhancement of the collapse structure, over-predict the collapse distance and hence provide some degree of conservatism in the design. Comparison between static and dynamic tests indicate an increase in average force of 21% at the impact interface and 13% at intermediate interfaces due to strain rate effects at 60km/h [63].

2.5 Injury criteria of passengers

2.5.1 General

The ultimate aim for any crashworthiness programme is to safeguard passengers. Hence the study of secondary collisions for passengers in an interior train setting has been an important aspect of BR's crashworthiness research. Some requirements are obvious such as the elimination of sharp protrusions, corners and grab handles etc. Furthermore, seat stiffnesses and head rests need careful design, as do tables and luggage storage spaces. Seating layout, with its many possible variations, is a primary determinant of possible flail distance [52].

Several means of defining injury and injury severity have been established. The Railway Inspectorate (RI) classify injuries as fatal, serious or minor; serious injuries are those requiring overnight hospitalization or broken limbs. Vehicle Safety Consultants Ltd. (VSC), to whom BR has contracted some of the recent interior crashworthiness research programmes, have used the Abbreviated Injury Scale (AIS) extensively in examining road traffic accidents. The scale ranges from 0 (no injury) to 6 (medically untreatable condition) for all body parts. This is shown in Figure 2.36. Both the RI and VSC definitions are not entirely consistent. In most of the BR internal reports on casualty analyses of past accidents or interior crashworthiness, the Railway Inspectorate definitions (i.e. fatal, serious or minor) were used for presenting summary results of casualties, but when considering the detailed injury of bodily parts, the AIS score system was used [64].

In order to improve vehicle interior crashworthiness, sled tests have been conducted with various seating configurations and interior fixtures using instrumented dummies. These dummies are anthropomorphic and anthropometric so as to resemble closely a living person. The Hybrid III dummy developed by General Motors represents the best state of the art for frontal impact simulations at the current level of technology [65]. A more detail description of the Hybrid III dummy is described in Section 7.3 of Chapter 7. FE datasets are now available for the Hybrid III dummy to be meshed as an FE model. Many software codes are now capable of modelling an actual dummy as FE articulated rigid-bodies, such as MADYMO, PAMCRASH, DYNA3D etc. The FE models of dummies will be elaborated later in Section 2.6.

The Hybrid III dummy has 44 standard data channels, taking measurements of accelerations, forces, bending moments, deflections etc. relevant to various parts of the body during a sled test. Many of these measurements have generally accepted injury criteria associated with them which are widely applied within the automobile industry. A re-assessment of these criteria appropriate to the railway environment has been undertaken [66] and these are discussed in the next Section 2.5.2.

It must be emphasized that the Hybrid III dummy represents the size of a 50th percentile male and is universally used in the transport industry. Other sizes have also been used in North America. If a man is 5th percentile in height, it means that 5% of men are shorter than he is and 95% are taller. Percentile values may vary with the population studied. The injury criteria about to be discussed are in relation to measurements taken from the size of a 50th percentile male dummy. European legislation currently requires testing to be carried out only with the 50th percentile male dummy [65, 66].

2.5.2 Injury criteria applicable to the railway environment

Head

It has been well established that 75% of fatalities in all car accidents involved head injuries [3]. A recent medical study in the United States, which involved nearly 50,000 trauma patients in 95 trauma centres, discovered that although patients with head injuries accounted for only a third of the total cases, they represented two thirds of the trauma deaths [54]. Recent hospital records and accident statistics (all kinds) in Canada, England, Scotland, United States and Wales have also shown that the commonest single site of injury is the head [67]. Head and facial injuries formed the majority of fatal and serious injuries due to secondary impacts in seven recent major BR accidents analysed by VSC recently [64]. Thus the study of head injury criteria has always been given a high priority in the field of interior crashworthiness and medical science.

The 'Wayne State University Cerebral Concussion Tolerance Curve' is a boundary plot relating the effective acceleration and the duration of that acceleration as shown in Figure 2.37 [68]. The plot's data was derived from tests conducted by impacting animal and cadaver foreheads against plane unyielding surfaces. Another set of tolerance data was based on exposing restrained seated military volunteers and

anaesthetized animals to constant-magnitude acceleration pulses with various pulse duration. The resulting three levels injury are reproduced in Figure 2.38 [68]. Note that although it is plotted in log-log coordinates, it is otherwise analogous to the Wayne State findings in Figure 2.37. It can be seen that very intense head acceleration is tolerable if it is very brief, but much less is tolerable if the pulse duration exceeds 10 or 15msec.

A proposal has been made by Gadd [69] for a criterion based on the Wayne State data. It is expressed in the following form :

$$GSI = \int_0^T a^{2.5} dt < 1000 \tag{2.43}$$

where *GSI* means Gadd Severity Index for head, '*a*' is the resultant acceleration in 'g' and *T* is the duration of impact in sec. Versace [68] modified Equation 2.43 to include a timing window :

$$HIC = \left\{ (t_2 - t_1) \left[\frac{1}{(t_2 - t_1)} \int_{t_1}^{t_2} (a) dt \right]^{2.5} \right\} < 1000 \tag{2.44}$$

where *HIC* means Head Injury Criteria and $(t_2\text{-}t_1)$ is less than 36msec and is chosen to maximize the *HIC*. Equation 2.44 with the threshold value of 1000 is widely used in the automobile industry [65,66]. A *HIC* above this threshold value is indicative of a threat to life. However, tolerance limits have also been statistically expressed as likelihood of death against *HIC* as shown earlier in Figure 2.33. The probability of fatality for a $HIC \leq 1000$ is 15%, and for $HIC \leq 500$ is about 3%. Thus recently there have been strong contentions about replacing the traditional threshold value of 1000 by 500 [65]. However, the standard threshold *HIC* used by the Motor Industry Research Association (MIRA) [66] and the Federal Motor Vehicle Safety Standard (FMVSS) is 1000 [59].

The United Nations Agreement Regulation No. 21 specifies the limit of maximum head acceleration as 80g for no more than 3msec. This is an achievable target in the motor industry and was recommended for use in the railway environment [66].

Neck

Neck injuries are one of the most common complaints in rail accidents and can lead to spinal damage and paralysis. Neck bending is a major mode of injurious loading and is commonly encountered by rearward facing passengers in low-back seating (Figure 2.39). Robinson [66] recommended two criteria for neck bending : a maximum of 190Nm for a chin-up motion (neck extension) and a maximum of 57Nm for neck flexion. According to Robinson, these are limits based on test results derived from volunteers and do not imply serious injury. These criteria have been in use for some time and have been widely adopted by other industries [65].

Other modes of injury loading include neck compression and neck shear. These are less well known and not directly outputted from the Hybrid III dummy. Robinson strongly recommended that these be studied and incorporated as part of the neck injury criteria and urged that the development of the dummy dataset be carried out soon [66].

Chest

The likely types of chest injury incurred during train accidents are broken ribs and internal organ damage. The most commonly-used measure of injury potential for the chest is the maximum compression of the chest cavity. Test data has suggested that a chest compression of 44mm (for 50th percentile male) results in no fractures to the ribs, whereas compression of 65 to 75mm leads to serious multiple fractures of the ribcage [66]. So the compression limit is to be determined from a value between 44mm and 65mm for use in railway environment.

Another very common chest injury criteria used in the automobile industry is that the limitation for chest acceleration should be 60g for no more than 3msec [66]. Bowmer [65] has recommended to use a stricter limit of 40g so that injury levels could be significantly reduced but no scientific reason was offered.

Although chest compression is obviously an important factor in thoracic injury, recent experiments with physiology models confirm the significance of loading velocity. The tolerable level of compression decreases as the velocity of loading increases due to the viscous nature of thoracic tissues. So the Transport Research Laboratory (TRL) recommends that the use of Viscous Criterion (VC) to assess chest injuries. This is the product of the instantaneous normal velocity of chest compression and the fraction of the allowed chest compression (65mm for 50th percentile male). For 25% expectation of serious injuries the VC should be less than 1.0. This criterion is accepted to some degree internationally and Robinson recommends that a development in the use of the VC be given consideration as a possible future addition to the chest injury criteria [66].

Abdomen

Due to the development of seatbelts and airbags for the motor transport, this body region has not received as much attention as the rest of the body. However, impact of the abdomen with table edges is a potentially serious problem for train passengers in an open-bay interior with a low-level table in between the bay-seats [66].

- Hybrid III dummies could be equipped with abdomen compression measurements, and a value of 40% compression (74mm for 50th percentile male) has been used in car testing for assessing the injury potential due to excessive lap belt loading. Bowmer [65] has recommended the use of 20% compression (37mm for 50th percentile male) on the basis that the 40% compression is equivalent to a 10% risk of sustaining an abdominal injury of AIS 4 or greater. 20% would reduce such high AIS scores. Robinson [66] proposed the inclusion of the Viscous Criterion (identical to that for the chest) into the abdomen injury criteria.

Femurs and hips

Current US regulations, which require femur loads to be below 10kN, are believed to be derived from considerations of the strength of the femur at its neck where it has turned through a right angle to enter the hip joint. However the femur is not the weakest part of the skeleton in this region but the pelvis at the hip joint. Accident investigations at the TRL suggest that the femur load above which the pelvis might be injured is in the region of 4kN. Bowmer concurred with this criterion [65].

Knees

Research has shown that 15.2mm is the limit of rearward tibia movement relative to the femur, beyond which the ligament damage is likely to occur. It was intended to protect the knee ligaments from rupture when the lower leg struck a surface. From the past accident records, knees impacting on the seat in front are common occurrences in uni-directional seating layout and so adoption of knee injury criteria is important [65].

Lower legs

Accident investigations at the TRL have shown that a normal force of 4kN can be tolerated in the tibia plateau (just below the knee).

For forces acting at a lower tibia region, bending moments and axial compression may coexist and the following mathematical criterion has been proposed [66] :

$$\frac{M}{M_c}+\frac{P}{P_c}\le 1 \qquad (2.45)$$

where M and P are the bending moment at the knee or ankle joint and compressive force of the tibia respectively. Also M_c and P_c are 225Nm and 35.9kN respectively for a 50th percentile male. The contact loads on the tibia are sensitive to the stiffnesses of the opposite seat-back (uni-directional seat layout) or seat-edge (open-bay seat layout) where the contacts are likely to be made, and these stiffnesses should thus be carefully studied for establishing a desired standard to be included in future codes of interior crashworthiness practice [66].

Summary

Table 2.4 summarizes the discussed injury criteria for a 50th percentile male :

Body region	Recommended threshold injury criterion [65,66]
Head	• *HIC* ≤ 500 for 3% likelihood of fatality (recommended). • *HIC* ≤ 1000 for 15% likelihood of fatality (MIRA in use). • 3msec exceedance limit : 80g
Neck	• 190Nm in flexion [F] • 57Nm in extension [E]
Chest	• Less than 44mm deflection. • 3msec exceedance limit : 40g. • Viscous Criteria (VC) should be studied and considered.
Abdomen	• Less than 37mm deflection. • Possibility of adopting VC should be considered.
Femurs & Hips	• 4kN Femur load.
Knees	• Less than 15.2mm deflection.
Lower legs	• 4kN on Tibia plateau. • $\frac{M}{M_c}+\frac{P}{P_c}\leq 1$

Table 2.4 : Threshold injury criteria for sled tests and FE analyses.

2.6 Interior crashworthiness for rail vehicles

2.6.1 Conclusions from VSC studies on six recent major BR accidents

The following major conclusions pertaining to passenger-injury trends were drawn by VSC studies on six major rail accidents occurring during recent times [64] :

- Impacts with seats, other passengers and the floor account to 76% of all injuries due to secondary collisions, the most common being with the seats (40%);
- Smaller numbers of injuries arose as a results of impacts with luggage, luggage racks, tables and partitions (21% in total). Transverse luggage racks were identified as a potential hazard;
- The percentages of injuries to parts of the body for all the accidents combined were as follows :

Head and face	34%
Neck	11%
Chest	13%
Arms	14%
Abdomen	8%
Legs	20%

- Injuries to arms and legs tended to be minor cuts, bruises and abrasions. Fractures were less common;

- Although not responsible for a significant number of injuries, VSC highlighted the potentially hazardous areas for passengers during secondary collisions such as loosely fitted components, open-space overhead luggages and wheeled items such as prams, buggies, wheelchairs etc.

2.6.2 The effect of impact pulses, sitting positions, interior seat layout, grab handles and seat belts on the injury potential of passengers

In response to the recommendations made by the Public Inquiry into the rail accident at Clapham Junction on 12 December 1988, BR initiated some interior crashworthiness research programmes with MIRA and VSC and at the same time developed its own in-house expertise in FE dummy simulations of secondary collisions using the dummy dataset of DYNA3D. The initial modelling works were parametric studies for investigating the behaviour of selected input parameters to the FE models. Experience gained in these FE models was then applied to models replicating actual dummy responses during certain MIRA sled tests [70].

The sled tests carried out by MIRA subjected occupants to four BR designated deceleration pulses known as C2, C3, C6 and C7 [71] and represent :

- C2- Two Mark I vehicles colliding at 18m/s.
- C3- Two Crashworthy vehicles colliding at 18m/s.
- C6- Two Mark I vehicles colliding at 13m/s.
- C7- Two Crashworthy vehicles colliding at 13m/s.

The C2 and C3 pulses represented the limits of old and proposed passenger vehicles at the impact speed of the Clapham collision; the C6 and C7 pulses represent collisions with half the energy of C2 and C3 respectively.

These BR specified pulses are shown in Figure 2.40 together with those achieved by MIRA in their HyGe sled facilities. It is clear that MIRA were unable to accurately represent the specified pulses; their principal aim was to achieve the required velocity change within the specified time span (i.e. areas under the specified pulses) [71].

The MIRA sled tests also studied the effect of occupant seating position and three seating positions were considered [71]:

- Single occupant seated opposite an empty seat and facing the impact (forward facing occupant).
- Single occupant seated opposite an empty seat with back to impact (backward facing occupant).
- Double occupants seated opposite each other with slight diagonal-offset so that their legs do not cross (double occupant).

Figure 2.41a and 2.41b show a single dummy (occupant) sitting on an open-bay seat in pre-test and post test positions [75] during the real full scale collision test (not a sled test).

The seating layout for the sled tests was of an open-bay type (face to face seating with a 2m seat pitch) without tables, similar to the interior of the vehicles involved in the Clapham collision.

The main conclusions drawn from the sled tests were [71] :

- Unacceptable levels of 3ms head acceleration occurred when the forward facing occupant was subjected to the C2 pulse and collided with the opposite vacant seat. The tests with other pulses and dummy seating positions all achieved acceptable head injury potential.
- Neck injury criteria were exceeded when forward facing occupants impacted the opposite vacant seats with all the impact pulses.
- Forward facing passengers opposite vacant seats suffered severe leg impacts, just below the acceptable value of 4kN at medium velocity (C6, C7) and exceeding the limits at high velocity (C2, C3).
- Backward facing occupants opposite vacant seats showed acceptable head and neck injury potential.
- For occupants striking another opposite occupant, the head impact severity was increased and increases in neck bending limits were also recorded.
- Lower leg injuries of striking occupants were reduced by interaction with a second occupant seated opposite.

These conclusions from the sled tests were fairly well correlated to the accident statistics.

Another type of interior seating layout in the BR passenger carrying fleet is the uni-directional seat arrangement (e.g. the Regional Railways Class 323 coach) with every seated passenger facing the back of the seat in front with a seat pitch of 0.76m. Swindell [72] performed many FE computations using this seating layout with the C3 pulse and studied the effect of grab handles and seat belts on the injury potential of occupants. Seat belts are unlikely to be recommended for rail travel and the study was merely to assess the likely benefits that could be gained. Two types of belt systems were modelled : the lap belt and three-point chest belt currently used in motor cars. His main conclusions can be found in reference [72] and are highlighted as follows :

- The FE model predicts no injury potential for a passenger seated in an uni-directional seat without grab handle and subjected to a C3 pulse. Head accelerations, lower leg contact loads and head/neck bending are all below the recommended limits. Serious head injury was predicted however, for the model with a grab handle fitted on the top edge of a seat (See Figure 2.42).
- DYNA3D is capable of predicting the effects of various configurations of seat belt restraint on passenger kinematics. The use of seat belts (particularly the three-point chest belt) can lead to significant reductions in injury potential.

Uni-directional seat has offered a safer seating configuration than the forward facing occupant in the open-bay seats. This is not surprising as studies have shown that minimizing the flail distance of an unrestrained occupant during secondary collisions could help to reduce the injury potential of the occupant [71]. An obstacle (preferably

soft-surface and energy absorbing) close to the occupant and on his flail path could act as a partial restrained system. This could be any interior furniture (such as a table or a partition wall) and is the next topic discussed.

2.6.3 Secondary collisions with interior tables and partitions

Swindell [73] has conducted FE studies using the DYNA3D Hybrid III 50th percentile dummy and a headform (the FE representation of the dummy head only) on secondary collisions with tables and partitions. For the study on impacts with a partition, a head form was modelled to move with an initial velocity (as a variable parameter) and collide with a partition wall in front. The partition surface stiffness is another variable parameter of his studied models. He extended the FE modelling works to include the effect of a bay table (a low level table between two open-bay seats) for a forward facing occupant in a Class 423 interior and also a fold-down table in a Class 323 interior, both of which were subjected to the C3 pulse. The potential injury caused by a bay table is on the abdomen and for a fold-down table is on the chest. Important findings of his works published in reference [73] may be summarized as follows :

- Surface stiffness for a partition wall should be between 10MN/m and 50MN/m in order for the *HIC* of an un-restrained passenger to score below 500. The soft coating thickness over the partition was recommended to be 7mm with the structure behind the coating designed to be deformable (i.e. energy absorbing).
- Bay tables with small mass and a mounting to provide a constant 6kN longitudinal reaction force are suitable for the striking occupants with a size of 50th percentile or smaller, but large sizes may cause the table to move excessively and collide with the occupant seated opposite the striking occupant.
- A space exists at the rear of a uni-directional seat into which a fold-down table could be mounted with low chances of adult occupants making contacts during impact. The space available depend largely upon the occupant size and initial position. A table 200mm deep mounted 140mm above the seat-base cushion was found not to contact any of the occupants modelled (See Figure 2.43). This is about 60mm lower than a typical design for fold-down tables as currently used in Class 323 vehicles. Implications on passenger comfort during normal operation for such lowering of fold-down table should be studied before making any firm recommendation.

BR has also been considering the development of a crashworthy bay table. Existing bay tables have inflicted numerous casualties (due to chest and abdomen injuries) in past rail accidents [74]. Two proposed designs were considered.

The first has a bolster built into the underside of the table top and the principle behind this design was that the knees close to the bolster would make first contact with it at the initial stage of the secondary collisions and restrain the occupant from travelling any further forward hence preventing an impact between the table edge and the abdomen or chest. The main disadvantage of this design is that the occupant leg room would be considerably reduced [74].

The second design involved the addition of an energy absorbing edge to the table top and energy absorption engineered into the bodyside fixing bracket [74].

Sled test results on both designs have shown that [74] :

- A bolster table increases the risks of occupant injuries by creating a rotary body mechanism which caused the head to collide with the table top on the far edge, and hence this design was rejected.
- On the other hand, a table with an energy-absorbing edge has shown to be effective in reducing abdomen injury risks and so this design was recommended for implementation.

2.7 Summary

2.7.1 Crushing of tubular components

A vast amount of theoretical and experimental work have been done on plain tube crushing due to the simplicity in their geometry. However, the main concern for the structure of a real vehicle is the collapse behaviour of the joints. This is obvious as a structure consists of an assembly of engineering components which are usually of different shapes and sizes (beams, tubes, plates, shells etc.), and all of which are joined by rivets, welds, bolts or adhesives. Very little information concerning the collapse behaviour of joints has appeared in the literature.

The theories as proposed by various authors for predicting the mean crushing load of tubular structures are only approximations and many of them 'modified' their theories to suit experimental results.

Some thermoplastic tubes, such as HDPE, have the attractive ability to 'recycle' upon re-heat. A crushed HDPE tube would partially recover its original uncrushed geometry by simply submerging in boiling water for some time. No comprehensive studies has yet been conducted to investigate the crushing performance of tubes that made of such recycled materials.

It is difficult to find literature that concentrate on comparing the energy absorption and mean crushing load of tubular components of different materials. Most importantly, how differently structures of different materials behave in their joints' collapse should be comprehensively studied. These studies could be formulated into a materials' database for future designers to use as a crashworthy material selection guide.

2.7.2 BR past accident statistics

The major conclusion drawn from the past BR accident statistics is that maximum benefit in terms of reducing fatalities is gained by concentrating development effort on end-on collisions below 40mph.

The statistics also has shown that the prevention of vehicle over-riding is the most important single factor in reducing passenger and crew fatalities.

Since full scale dynamic and static tests for rail vehicles are expensive and time-consuming, it is beneficial to extract as much information as possible from real accidents. This approach has already generated much useful information.

2.7.3 Structural crashworthiness

BR has adopted a crashworthiness philosophy for rail vehicles, which requires coaches to be disconnected at each interface as soon as possible during a collision, allowing each coach to absorb its own kinetic energy. This concept is sound for multiple units with coaches having similar mass. For this concept to work successfully during collisions, the designed trains must fulfill three requirements :

(1) Vehicles end-structures must be designed as sacrificial zones so as to collapse plastically in a controllable manner, thus safeguarding the main passenger compartment. Sufficient energy dissipative capacity must be incorporated into these vehicle end-structures to absorb the collision energy;

(2) The couplers must break away at a set load and push back into an allocated space within the end-structures, so as to create an interface gap for trailing coaches to close up before making contact with the leading vehicles;

(3) Coaches must not derail or override each other.

A full scale collision test between two similar rakes of trains conducted by BR during October 1994 has validated this philosophy. This philosophy has replaced the old 'the stronger the better' code-of-practice.

The incomplete understanding of the collapse behaviour of structural joints has obstructed the incorporation of these joint failure mechanism into FE models. However, recent work carried out at the University of Sheffield and Cranfield University has made some progress concerning the understanding of joint behaviour and the FE simulation of the successive stages of failure of the joints. This work is important to designers and would be of benefit during the early design phase.

2.7.4 The behaviour of rakes of vehicles

The inter-vehicular gap plays an important role for colliding rakes of vehicles. A gap greater than or equal to the tuned gap size results in a significant reduction in the plastic deformation sustained by the impact interface and achieves a more even distribution of energy along the colliding rakes.

When two trains with different numbers of coaches collide, more energy is dissipated in the larger train. The intermediate interfaces for the larger train thus sustained more plastic deformation than those in the smaller train. Similarly, when trains with equal

number of coaches but different gap sizes collide, more energy is dissipated in the rake containing the larger gaps (i.e. the longer train).

The one-dimensional mass-spring models have demonstrated their capability in achieving good correlation with actual full scale collision test. However, without strain-rate enhancement on the static load-deflection characteristics of the springs, they over-predict the interface crush distances and this could serve to provide some degree of conservatism for the design of train.

Rake behaviour was exhaustively studied by Chatterjee and Carney [59], but their models did not include couplers and dampers. Couplers and damping make important contributions to the behaviour of vehicles in rakes and so extensions of their studies to include couplers and dampers are deemed necessary.

2.7.5 Interior crashworthiness

Impacts with seats, other passengers and the floor are identified to be the major causes of all injuries due to secondary collisions, the most common being with the seats. Smaller numbers of injuries arose as a results of impacts with luggage, luggage racks, tables and partitions.

Fatal injury is seldom as a result of secondary impact with the vehicle interior. The majority of injuries caused by secondary impacts are confined to the upper body with the head and face being the most vulnerable.

BR has done a lot of research works on interior crashworthiness using DYNA3D dummy models. Sled tests have also been conducted using the facilities provided by MIRA. Summaries of these studies are highlighted below :

(1) Forward facing passengers in open-bay seats experienced forces in excess of neck injury criteria but acceptable head accelerations and leg contact forces in collisions against vacant opposite seat. If a passenger sat opposite, both might receive severe head injuries, although neck and leg injuries might be reduced.

(2) Rearward facing passengers in open-bay and unidirectional seats sustained head accelerations and neck bending moments well below limiting values.

(3) Forward facing passengers in uni-directional seats were liable to sustain neck injuries caused by hitting the seat in front, possibilities of inflicting these injuries reduced if the seats deformed locally.

(4) Forward facing occupants sitting in open-bay seats are more vulnerable to serious head and neck injuries than those in unidirectional seats.

(5) Partitions mounted features, telephone areas, wheelchair areas, grab handles and toughened glass partitions were all identified as potential hazards.

(6) Results of sled tests and mathematical modelling were fairly well correlated.

(7) Installing bay tables with energy absorbing capability could benefit the forward facing occupants in open-bay seats.

(8) Little work has been done on investigating the behaviour of standing passengers.

References

[1] Pugsley, A., "The Safety of Structures.", Edward Arnold (Publishers) Ltd., London, 1966.

[2] Johnson, W. & Mamalis, A. G., "Crashworthiness of Vehicles.", Mechanical Engineering Publications Ltd., London., 1978.

[3] Johnson, W., "The Elements of Crashworthiness : Scope and Actuality.", Proc. IMechE, Vol. 204D, p. 255, 1990.

[4] Jones, N., "Structural Impact.", Cambridge Univ. Press, Cambridge, 1989.

[5] Macaulay, M. A., "Introduction to Impact Engineering.", Chapman and Hall, London, 1987.

[6] Jones, N. & Wierzbicki, T. (eds.), "Structural Crashworthiness.", Butterworth & Co. (Publishers) Ltd., London, 1983.

[7] Davies, G. A. (ed.), "Structural Impact and Crashworthiness : Volume 1.", Elsevier Applied Science Publications, London, 1984.

[8] Morton, J. (ed.), "Structural Impact and Crashworthiness : Volume 2.", Elsevier Applied Science Publications, London, 1984.

[9] Calladine, C. R., "The Teaching of Some Aspects of the Theory of Inelastic Collisions.", Int. J. Mech. Engng. Edu., Vol. 18, p. 301, October 1990.

[10] Lewis, J. H., "Literature Survey.", Technical Memorandum no. TM EST 27, BRB Research & Development Division, Derby, August 1984.

[11] Carney, J. F., "Rail Vehicle Crashworthiness Simulation : State of the Art Practice.", Internal Report, Vanderbilt Engineering Centre for Transportation Operations and Research (VECTOR), Vanderbilt University, Nashville, Tennessee, March 1993.

[12] Pugsley, A. G., "The Crumpling of Tubular Structures under Impact Conditions.", Symposium on the Use of Aluminium in Railway Rolling Stock, Paper 4, Inst. Loco. Engr., London, p. 33, November 1960.

[13] Johnson, W., Mamalis, A. G. & Reid, S. R., "Aspects of Car Design and Human Injury.", Chapter 4, Human Body Dynamics (Ghista, D. N. ed.), Oxford Univ. Press, p. 164, 1982.

[14] Thornton, P. H., Mahmood, H. F. & Magee, C. L., "Energy Absorption by Structural Collapse.", Chapter 4, Structural Crashworthiness (Jones, N. & Wierzbicki, T. eds.), Butterworth & Co. (Publishers) Ltd., London, p. 96, 1983.

[15] Rawlings, B., "Response of Structures to Dynamic Loads.", Proc. Conf. on the Mechanical Properties at High Rates of Strain, Institute of Physics, Bristol, p. 279, 1974.

[16] Johnson, W. & Reid, S. R., "Metallic Energy Dissipating Systems.", Appl. Mech. Rev., ASME, Vol. 31, p. 277, March 1977.

[17] Jones. N., "Some Fundamental Studies in Structural Crashworthiness.", Proc. IMechE. Congr. on Safety and impact : Legislation, Liability and Lesson (Autotech 1991), Paper No. C427/4/116, Status Print Media Ltd., London, 1993.

[18] Wirsching, P. H. & Slater, R. C., "The Beer Can as a Shock Absorber.", J. Eng. Mat. and Tech., Vol. 95, p. 224, 1973.

[19] Horton, W. H., Bailey, S. C. & Edwards, A. M., "Non-symmetric Buckle Patterns in Progressive Plastic Buckling.", Exptl. Mechs., Vol. 6, p. 433, 1966.

[20] Andrews, K. R. F., England, G. L. & Ghani, E., "Classification of Axial Collapse of Cylindrical Tubes under Quasi-static Loading.", Int. J. Mech. Sci., Vol. 25, p. 687, 1983.

[21] Thornton, P. H. & Magee, C. L., "The Interplay of Geometric and Materials Variables.", J. Eng. Mat. and Tech., Vol. 99, p. 114, 1977.

[22] Timoshenko, S., "Theory of Elastic Instability.", McGraw-Hill, New York, 1936.

[23] Donnell, L. H. & Wan, C. C., "Effects of Imperfections on Buckling of Thin Cylinders and Columns Under Axial Compression.", J. Appl. Mech., Vol. 17, p. 73, 1950.

[24] Alexander, J. M., "An Approximate Analysis of the Collapse of Thin Cylindrical Shells Under Axial Loading.", Quart. J. Mech. Appl. Math., Vol. XIII, p. 10, 1960.

[25] Abramowicz, W. & Jones, N., "Dynamic Axial Crushing of Circular Tubes.", Int. J. Impact Engng., Vol. 2, No. 3, p. 263, 1984.

[26] Pugsley, A. G. & Macaulay, M., "The Large Scale Crumpling of Thin Cylindrical Columns.", Quart. J. Mech. Appl. Math., Vol. XIII, p. 1, 1960.

[27] Johnson, W., Soden, P. D. & Al-Hassani, S. T. S., "Inextensional Collapse of Thin Walled Tubes Under Axial Compression.", J. Strain Anal., Vol. 12, p. 317, 1977.

[28] Soden, P. D., Al-Hassani, S. T. S. & Johnson, W., "The Crumpling of Polyvinylchloride Tubes Under Static and Dynamic Axial Loads." Proc. Conf. on the Mechanical Properties at High Rates of Strain, Institute of Physics, Bristol, p. 327, 1974.

[29] Macaulay, M. A. & Redwood, R. G., "Small Scale Model Railway Coaches Under Impact.", The Engineers, No. 25, p. 1041, December 1964.

[30] Lowe, W. T., Al-Hassani, S. T. S. & Johnson, W., "Impact Behaviour of Small Scale Model Motor Coaches." Proc. IMechE., Vol. 186, p. 409, 1972.

[31] Postlethwaite, H. E. & Mills, B., "Use of Collapsible Structural Elements as Impact Isolators, with Special Reference to Automotive Applications.", J. Strain Anal., Vol. 5, p. 58, 1970.

[32] Jones, N. & Birch, R. S., "Dynamic and Static Axial Crushing of Axially Stiffened Square Tubes.", Proc. IMechE., Vol. 204C, p. 293, 1990.

[33] Reid, S. R. & Reddy, T. Y., "Static and Dynamic Crushing of Tapered Sheet Metal Tubes of Rectangular Cross-Section.", Int. J. Mech. Sci., Vol. 28, p. 623, 1986.

[34] Mamalis, A. G., Manolakos, D. E., Viegelahn, G., Vaxevanidis, N. M. & Johnson, W., "On the Inextensional Axial Collapse of Thin-walled PVC Conical Shells.", Int. J. Mech. Sci., Vol. 28, No. 9, p. 323, 1986.

[35] Mamalis, A. G., Manolakos, D. E., Saigal., S., Viegelahn, G. & Johnson, W., " Extensional Plastic Collapse Thin-wall Frusta as Energy Absorbers.", Int. J. Mech. Sci., Vol. 28, p. 219, 1986.

[36] Al-Hassani, S. T. S., Johnson, W. & Lowe, W. T., "Characteristics of Inversion Tubes Under Axial Loading." J. Mech. Engng. Sci., Vol. 14, p. 370, 1972.

[37] Rawlings, B., "Energy Absorption of Dynamically and Statically Tested Mild Steel Beams Under Conditions of Gross Deformation.", Int. J. Mech. Sci., Vol. 9, p. 633, 1967.

[38] Mcfarland, R. K., "Hexagonal Cell Strcutures Under Post-buckling Axial Load.", AIAA Journal, Vol. 1, p. 1380, 1963.

[39] Wierzbicki, T., "Crushing Analysis of Metal Honeycombs.", Int. J. Impact Engng., Vol. 1, p. 157, 1983.

[40] Kirk, J. A., "Design of a Metal Skinning Energy Absorber for the U. S. Capitol Subway System.", Int. J. Mech. Sci., Vol. 19, p. 595, 1977.

[41] Redwood, R. G., "Buckling of Thin Walled Tubes Under Axial Impact.", J. Roy. Aeronaut. Soc., Vol. 68, p. 418, June 1964.

[42] Symonds, P. S., "Viscoplastic Behaviour in the Response of Structures to Dynamic Loading.", Proc. Conf. on the Behaviour of Materials Under Dynamic Loading (Huffington N. J. ed.), p. 106, ASME, New York, 1965.

[43] Campbell, J. D. & Cooper, R. H., "Yield and Flow of Low-carbon Steel at Medium Strain Rates." Proc. Conf. on the Physical Basis of Yield and Fracture, Inst. of Physics, London, p. 77, 1966.

[44] Perrone, N., "A Mathematically Tractable Model of Strain-hardening, Rate-sensitive Plastic Flow.", J. Appl. Mech., Vol. 33, p. 210, 1966.

[45] Lewis, J. H., "An Analysis of Casualties, Vehicle Damage and Repair Costs in Railway Accidents.", Technical Memorandum no. TM EST 034, BRB Research & Development Division, Derby, March 1986.

[46] Lewis, J. H., Rogers, T. C. & Allison, D. M., "Crashworthiness Development : An Analysis of Accidents, Casualties and Vehicle Damage in Train Accidents 1982-1991.", British Rail Research Report, No. LR/VST/93/017, Derby, March 1993.

[47] Lewis, J. H. & Rogers, T. C., "Crashworthiness Development : An Analysis of Accidents, Casualties and Vehicle Damage in Train Accidents 1984-1993.", British Rail Research Report, No. RR-STR-95-029, Derby, April 1995.

[48] Scholes, A., "Passenger Vehicle Design Loads and Structural Crashworthiness.", Proc. IMechE. Conf. on Railway Vehicle Body Structures, paper no. C294/85, p. 147, Mechanical Engineering Publications, London, 1985.

[49] Scholes, A., Lewis, J. H. & Rasaiah, W. G., "Crashworthiness Collision Tests.", British Railway Research Report, No. RR-STR-95-037, Derby, March 1995.

[50] Scholes, A. & Lewis, J. H., "Development of Crashworthiness for Railway Vehicle Structures," Proc. IMechE., Vol. 207F, p. 1, 1993.

[51] British Railways Board, "Structural Design Load Cases for Passenger Carrying Vehicle Bodies.", Group Standard GM/TT0079, Issue 1 Rev. A, July 1992.

[52] Smith, R. A., "Crashworthiness Moves From Art to Science.", Railway Gazette Int., p. 227, April 1995.

[53] Chatterjee, S. & Carney, J. F., "Occupant Protection and Interior Crashworthiness in Trains.", Internal Report, Vanderbilt Engineering Centre for Transportation Operations and Research, Vanderbilt University, Nashville, Tennessee, May 1995.

[54] Carney, J. F., "Rail Vehicle Crashworthiness Simulation : State of the Art Practice."; Internal Report, Vanderbilt Engineering Centre for Transportation Operations and Research (VECTOR), Vanderbilt University, Nashville, Tennessee, March 1993.

[55] Tong, P., "Rail Vehicle Structural Crashworthiness.", Chapter 14, Structural Crashworthiness (Jones, N. & Wierzbicki, T. eds.), Butterworth & Co. (Publishers) Ltd., London, p. 397, 1983.

[56] Sutton, A. & Lewis, J. H., "Elastic/Plastic Interaction of Rakes of Rail Vehicles.", Structural Impact and Crashworthiness Vol. 2 (Morton J. ed.), Elsevier Applied Science Publications, London, p. 783, 1984.

[57] Ohnishi, T., Kawakami, N. & Sano, A., "Crashworthiness of Trains.", Proc. Int. Conf. on Speedup Technology for Railway and Maglev Vehicles, Vol. 1, JSME, Tokyo, p. 2, 1993.

[58] Revan, A. J., "Crashworthiness Development : Parametric Study of Vehicles in Rakes.", British Rail Research Report, No. LR/VST/93/010, Derby, March 1993.

[59] Chatterjee, S. & Carney, J. F., "Crash Energy Management and Interior Crashworthiness in Passenger Trains.", Internal Report, Vanderbilt Engineering Centre for Transportation Operations and Research, Vanderbilt University, Nashville, Tennessee, December 1994.

[60] Tyrell, D., Severson-Green, K. & Marquis, B., "Analysis of Occupant Protection Strategies in Train Collisions." Proc. ASME Winter Annual Conf. on Crashworthiness and Occupant Protection in Transportation Systems, December 1995. (To be published).

[61] Rocholl, H., "Energy Absorption in Automatic Couplings and Draw Gear.", Proc. IMechE. Conf. on Railway Vehicle Body Structures, paper no. C288/85, p. 137, Mechanical Engineering Publications, London, 1985.

[62] Gregory, W. P. & Lewis, J. H., "Crashworthiness Development : Vehicle Couplers.", British Rail Research Report, No. LR/VST/93/018, Derby, March 1993.

[63] Lewis, J. H. & Rasaiah, W. G., "Dynamic Tests on Rakes of Crashworthy Vehicles.", British Rail Research Report, No. RR-STR-95-026, Derby, May 1995.

[64] Griffin, T., Carey, W., Ashburner, E. & Lewis, J. H., "Summary of Interior Crashworthiness Studies.", British Rail Research Report, No. LR/VST/94/008, Derby, March 1994.

[65] Bowmer, C., "Report on the Proposed Levels of Injury Criteria for Use in Rail Passenger Vehicle Interiors.", The Engineering Link Technical Report, No. 95/XXX/6461/01, Derby, February 1995.

[66] Robinson, K. P., "Injury Criteria for Use in a Railway Environment.", British Rail Research Report, No. LR/VST/94/001, Derby, May 1994.

[67] Kihlberg, J. K., "Head Injury in Automobile Accidents.", Proc. Conf. on Head Injury (Caveness, W. F. & Walker, A. E. eds.), p. 27, J. B. Lippincott Co., Philadelphia, 1966.

[68] Varsace, J., "A Review of the Severity Index.", Proc. 15th Stapp Car Crash Conf., p. 771, SAE, New York, 1971.

[69] Gadd, C. W., "Use of a Weighted-Impulse Criterion for Estimating Injury Hazard.", Proc. 10th Stapp Car Crash Conf., p. 164, SAE, New York, 1966.

[70] Swindell, M., "Crashworthiness Development : Theoretical Methods for the Assessment of Vehicle Interiors & Occupant Kinematics.", British Rail Research Report, No. LR/VST/92/042, Derby, November 1992.

[71] Hewitt, G. G., "Post-Clapham Programme : Review of MIRA & V.S.C. Studies.", British Rail Research Report, No. LR/VST/92/003, Derby, February 1992.

[72] Swindell, M., "Crashworthiness Development : Further Assessment of Vehicle Interiors & Occupant Kinematics.", British Rail Research Report, No. LR/VST/93/007, Derby, March 1993.

[73] Swindell, M., "Crashworthiness Development : Investigation of Occupant Impact with Vehicle Partitions and Tables.", British Rail Research Report, No. LR/VST/94/004, Derby, February 1994.

[74] Bowmer, C., "Report on the Development of a Crashworthy Table.", The Engineering Link Technical Report, No. 95/XXX/6461/03, Derby, March 1995.

[75] Robinson, K. P., "Occupant Behaviour in Train Collision Tests", British Rail Research Report, No. RR-STR-95-027, Derby, July 1995.

Chapter 3

Non-linear mass-spring models for studying the behaviour of colliding rakes of trains

3.1 Introduction

3.1.1 General

The traditional structural requirements for passenger rail vehicles have been based on a 'the stronger the better!' philosophy, in that various parts of the vehicle body are required to sustain a specified longitudinal load without permanent deformation [1]. Recent work in British Rail Research (BRR) has led to the development of crashworthiness requirements for rail vehicles based on the concept of collision energy dissipation management [1-3]. Trains should now be built with crush zones at each vehicle end and designed to withstand collapsing forces over some defined crushing distance in order to control the absorption of the collision energy. Hence restricting the damage to the end of the vehicle with the aim of providing the required survival space for the passengers.

It was recognised that instead of having large crush zones in all train compartments each designed to absorb a large amount of collision energy, the crush zone lengths could be optimised by distributing the rest of the energy to the other sacrificial zones along the rake of vehicles. This means that during a collision between two crashworthy trains, each vehicle should, ideally, absorb its own impact energy. This could only be accomplished if all the coaches within a train were loosely coupled and no such train exist in practice. The interaction between resiliently coupled coaches would cause uneven distribution of dissipated energy along the rake during a collision. The search for a method to enable an even distribution of dissipated energy across all the interfaces along the rakes of colliding trains is a major objective of rail vehicle crashworthiness studies. To achieve this objective, it is important to understand the behaviour of coaches connected in rakes during a collision.

This Chapter, an introduction to the study of the behaviour of rakes of coaches, begins by studying a simple colliding situation using the DYNA3D version of non-linear spring-mass-damper elements. Each pair of back to back coupled vehicle end crush zones (an interface) is represented by a piece-wise linear spring, such as that shown in Figure 3.1, and the main passenger compartment is represented by the lump mass with the required translation inertia properties. Subsequently in Chapter 5, the models is improved to include gaps, couplers and damping. In Chapters 6 and 7, the effects of the shape of the spring's load-deflection curve on the behaviour of collisions of symmetric rakes of trains is investigated.

The next Section 3.1.2, introduces the theoretical foundations of the non-linear Finite Element (FE) code, DYNA3D, used in this Chapter. Section 3.1.3, explains more about the spring which represents the vehicle end-crush zone. Section 3.2 highlights the limitations of using mass-spring models to simulate the collision of two symmetric rakes of trains. Section 3.3 determines whether the stress wave typically experienced by a dynamically loaded structure can be ignored as in a mass-spring model. This is done by comparing the effects of the deceleration pulses derived by a mass-spring model and its equivalent bar-spring model on the passengers. Section 3.4 selects some input parameters for the mass-spring models, such as coach mass, crush zone collapse load, impact velocity etc., and performs a mathematical investigation concerning their influence on the performance of the non-linear mass-spring-mass models (representation of a one-coach to one-coach impact configuration) in terms of the time rate of energy dissipation ($\dot{E}$, or energy dissipative power). The use of $\dot{E}$ for train crashworthiness study is novel and offers some useful insight into the study. Section 3.4 also performs actual numerical experiments to verify the derived mathematical results. Section 3.5 studies the effects of introducing a pair of compressive external impulses to a mass-spring-mass model on its energy dissipative power.

3.1.2 DYNA3D non-linear mass-spring models : Basic theory

As mentioned earlier in Chapter 2, the lumped mass & spring modelling has been a traditional tool during the early design stages in the transport industry for studying the dynamic response and crashworthiness of both motor vehicles and trains. Tong [4] has highlighted that the overall dynamic interaction of a train in the principal impact direction could be estimated by a one-dimensional model in which each rail-coach is represented by a single mass or an assemblage of a series of masses. The dampers and springs that connect the masses in a series may have linear or non-linear force-deflection relations to represent the elastic-plastic, buckling, and collapse behaviour of the vehicle structures. The dynamic equations are solved by a standard numerical integration procedure. The analyses of such lumped mass-spring models can be carried out and post-processed quite quickly on a SUN/C SPARC work station, and are thus well suited for parametric studies.

Non-linear mass-spring analysis in the current work were undertaken using the OVE ARUP systems version of the DYNA3D code [5]. DYNA3D offers a complete set of linear, non-linear, elastic and elasto-plastic springs and dash-pots elements, and lumped masses can be completely defined as nodal masses. The dynamic system governing equations are solved by using the explicit time integration scheme, and such a scheme is conditionally stable, i.e. the time step has to be controlled to prevent numerical instability.

Consider a moving three-coach train approaching a stationary three-coach train at an approach velocity of V_0, as shown in Figure 3.2. We are interested in relatively high speed collisions of heavy coaches which directly implies that the interfacial deformations for these coaches (at the impact end) will be permanent and non-recoverable. The analysis thus requires non-linear spring characteristics to model plastic deformations.

The governing ordinary differential equations (ODEs) for the above non-linear mass-spring model are :

$$\begin{aligned}
&M_1\ddot{x}_1 + k_1(x_1 - x_2) + F_1 = 0\\
&M_2\ddot{x}_2 - k_1(x_1 - x_2) + k_2(x_2 - x_3) + F_2 = 0\\
&M_3\ddot{x}_3 - k_2(x_2 - x_3) + k_3(x_3 - x_4) + F_3 = 0\\
&M_4\ddot{x}_4 - k_3(x_3 - x_4) + k_4(x_4 - x_5) + F_4 = 0\\
&M_5\ddot{x}_5 - k_4(x_4 - x_5) + k_5(x_5 - x_6) + F_5 = 0\\
&M_6\ddot{x}_6 - k_5(x_5 - x_6) + F_6 = 0
\end{aligned} \qquad (3.1)$$

where n = sequence number for coach from left to right in Figure 3.2.

M_n = mass of coach n, n=1 to 6;

x_n = displacement of coach n, n=1 to 6, (an over-head dot denote time derivative);

k_n = stiffness of spring n, n=1 to 5, this is a function of x_n (see Figure 3.2);

$F_n = \mu g M_n$, friction force for coach n, n=1 to 6;

μ = coefficient of friction, assume to be constant;

g = gravity acceleration;

The above differential equations are non-linear because the springs' stiffnesses k_n are not constants but are dependent on the relative displacement between two adjacent masses linked by the spring. In addition, plasticity is involved which leads to different loading and unloading load-deflection paths once the springs have yielded. However, the work described here have assumed loading and unloading stiffness to be the same.

The explicit solution for the above set of ODEs advances the solution along the time axis after defining the required initial conditions. The velocities are discretized at half time intervals, $t_{n-\frac{1}{2}}, t_{n+\frac{1}{2}}$,...etc., and the displacements and accelerations at full time intervals, t_{n-1}, t_n, t_{n+1},...etc., where n is the number of the time increment. Accelerations at time t_n are solved and then a central difference scheme is employed to calculate velocities and displacements. The disadvantage of the explicit method is that the requirement for stability puts an upper bound limit on the time step, Δt, namely,

$$\Delta t = \sqrt{\frac{2M}{k}} \tag{3.2}$$

For all non-linear explicit FE packages, the solution time step is governed by the most deformed element during the analysis. Note that explicit codes cannot extract the eigenvalue(s) of a mass-spring system.

3.1.3 More about 'The spring'

The spring is in fact a representation of the coach end crush zone. An example of such an end structure was reported by Scholes & Lewis [2], as shown in Figure 3.3a. This is a new crashworthy cab designed for a 24 tonne passenger coach. Future rail vehicles would strive to attain optimal mass/passenger and 24 tonne (16 tonnes tare mass and 8 tonnes of bogies) was recognised as an achievable target [2, 6]. The proposed cab that was designed to absorb collision energy in a few 'constant-force plateaus' as indicated in Figure 3.3b. A variety of features were designed to encourage initiation of failures and subsequent collapse in a predicted way for achieving the required force-deflection characteristic. These include kinks in the headstock for initiating buckling whilst the solebar had a collapse initiator to promote shearing failures. The designed sequence of events for the various components shown in Figure 3.3a during a full face collapse is as follows :

(1) At 480kN the coupler breaks away;

(2) The GRP tubes collapse at a constant load of 800kN;

(3) At 960kN total applied load, solebar joint shear;

(4) Load is transferred to the 'kinked' diagonals which fail in bending and allow the headstock to be pushed backwards;

(5) Once the clearance between the headstock and the honeycomb is taken up, load is applied through the honeycomb such that the combined collapse load of the honeycomb and cab structure again reaches 960kN. Collapse proceeds with the rest of the structures at a designed constant force of 960kN.

The total designed energy absorption is 952kJ within 1.17m of the crushed end cab structure alone and with a hydraulic coupler that would be sufficient to meet the BR crashworthiness requirement of "at least 1MJ within a metre with maximum force not exceeding 3MN" [2]. Note that the cab was also designed to absorb 0.48MJ within 1m crush distance during an overriding accident with the vehicle staying upright throughout and overriding occurring just above the anti-climber buffers.

A similar crashworthy end cab design was also being considered in North America [7].

3.2 The limitations of non-linear mass-spring models

The current Chapter is restricted to train collisions involving two Electrical Multiple Units (EMUs) hitting each other head-on. EMUs were chosen throughout for the current research work since they constitute the main bulk of the present passenger-carrying fleet and have been commonly involved in past accidents. To represent such a one-coach to one-coach collision using the mass-spring-mass models, the following assumptions were made :

(1) Couplers do not play a significant role in absorbing collision energy and can be ignored. This is justifiable since we do not expect the two EMUs to engage their couplers during the collision and that in high velocity collisions the impact interface couplers shear away very quickly (designed to breakaway at a prescribed longitudinal load) before absorbing any significant amounts of energy. Couplers would have to be included if the model extends to include more coaches because the intermediate interface couplers would have more influence on the overall energy distribution along the rake. This is address later in Chapter 4.

(2) No overriding or derailment. This is in line with the current BR crashworthiness specification which emphasises the importance of prevention of overriding and derailment of trains during collisions. The implication of this assumption is that the models are one-dimensional with multiple degrees of freedom (DOF). In the present Chapter, 2 DOF.

(3) The bogie longitudinal stiffness is ignored. Earlier work carried out by Revan [8] has shown that this can be ignored without significant errors in the present analysis, since the bogies pivots have high stiffness and are designed to travel a maximum of only 3 mm. Hence, during a high velocity impact the bogies rapidly reach the maximum travel permitted and for the rest of the motion, the bogies and the main coach body can be assumed to travel together as one.

(4) Unless otherwise stated, friction and structural damping are ignored. The effects of wheel-track friction and structural damping will be discussed later in Sections 3.4 and 3.5.

(5) Stress wave effects within the coach body are ignored. This means that whatever force received on one end of the coach is immediately 'felt' by the other end, which is essentially, how a lump mass behaves.

For the last point, Carney [3] has, in a recent report, compared the FE analysis between a non-linear one dimensional mass-spring model and a non-linear three-dimensional brick-element model in representing a one to one vehicle collision. His results showed that the difference in the energy dissipation for the two models is small and that the only

major concern came from the high frequency content in the deceleration pulse of the brick model which takes stress wave activity within the coach structure into account. He commented that the high frequency acceleration is unlikely to affect the secondary collisions (passengers inside the coach hitting the interior fixtures) and thus all his later modelling were carried out using the spring-mass model. No attempt has been made to prove his argument. This point is further considered in the next section.

3.3 Coach representation : a bar or a lumped mass?

3.3.1 Introduction

Coach structures have both stiffness and mass and that would imply that they are subjected to stress wave activities when loaded suddenly. This Section compares two one-dimensional models, the first model represent the passenger compartment of a coach with a bar and the second with a lumped mass. This is done so as to consider the effects of the deceleration on passengers sitting within the vehicle. PAMCRASH Hybrid III 50%th Dummy Models are used for simulating the passengers sitting in a Class 423 open-bay seat environment. More elaborating works about dummy modelling are illustrated later in Chapters 7 and 8.

3.3.2 Observations made from the 1983 ORE fully instrumented rail vehicle collision test

In 1983, the Office for Research and Experiments (ORE) which is the research arm of the International Union of Railways (UIC), had formed an International Technical Committee (B165) to investigate the dynamic loading of drivers' cabs. This Committee was formed of representatives of the main European railways with BR taking the chair. One of the major tasks of this Committee was to test a specifically designed cab end dynamically so as to verify the design code for structural crashworthiness. The design specification for the crashworthy cab agreed by the ORE Committee was similar to that used by BR and is highlighted in Reference [9]. The cabs were grafted onto two similar 40 tonnes (30 tonnes body mass and 10 tonnes of bogies) vehicles and a fully instrumented coach to coach collision test was conducted. During the test, one vehicle was propelled onto a stationary vehicle at 16.4 m/s with anti-climbers (to prevent vehicle override) and couplers fitted on both impacting and impacted cabs. This was an expensive experiment which took a lot of time in planning and organisation. In the test, over 100 channels of data, through the use of strain gauges, accelerometers and displacement transducers, were recorded. There was no mention of any dummy being used.

The measured acceleration of the centre of gravity (c. of g.) of the impacted vehicle was shown to contain high frequency content and had to be filtered before interpretation of the results. Similar observations were made for the measured forces within the end cab structures. These are apparently caused by the stress waves within the structure. However, questions remain as to the likely effects upon passengers. This could be investigated by the use of dummies, or as in the automobile industry, made use of animals (mainly apes, dead or alive) or cadavers [10]. Dummies have already been constructed as meshed finite element models in some special FE codes such as MADYMO, DYNA3D and PAMCRASH, and the results found to correlate well with those from experiments. It should be emphasised that the FE dummies are representations of the actual dummy models and not human beings.

For the next stage of work, two parts of modelling work were carried out :

(1) Two models were built for simulating a one-coach train to a rigid wall collision. Both models utilised the piece-wise linear spring for representing the vehicle end crush zone; the first model utilised a nodal mass for representing the coach and the second model used a bar element instead.

(2) The resulting c.o.g. deceleration pulses generated by the two models in (1) were then respectively input to dummy models and the response to the two pulses compared.

3.3.3 DYNA3D train-collision simulations : mass-spring model Vs bar-spring model

Two models were built for simulating a one-coach unit (35tonnes) colliding at 17.5mph (7.78m/s) into a rigid wall. This is the same as two one-coach unit approaching each other at a closing velocity of 35mph (15.56m/s). One model made use of lumped mass, spring and dash-pot elements, the other used elastic bar, spring and dash-pot elements, as shown in Figures 3.4a and 3.4b.

The bar has a Young's modulus E (20GN/m^2), a length l (chosen as 26m for the current study), a cross section area A (0.18m^2) and a density ρ (7800kg/m^3). The Young's modulus was derived from the stiffness of a coach body taken to be 130MN/m [11] and the cross sectional area was chosen to provide the coach body with a mass of 35tonnes. Whereas the lump mass has only a mass of 35tonnes with no associated stiffness properties, it could be viewed as a rigid bar. Each model has a piece-wise linear spring and a small linear damper with 1% damping ratio. The spring's characteristic is shown in Figure 3.1. The impact velocity of 7.78m/s produces a total kinetic energy of 1.06MJ to be dissipated in order to bring the coach to rest and this is achieved through plastic deformation of the spring. The high yield force of the bar ensures that it remains elastic throughout the impact event with all energy absorption taking place in the spring (vehicle end crush zone). The DYNA3D simulations of each of the above models terminates once the system has achieved stability, i.e. the internal energy has reached the

maximum value and the mass is temporarily brought to rest. It was also the time when the springs started to unload and separate from the rigid wall, i.e. rebound.

Figure 3.5 shows the velocity time histories for both models. This graph shows that the bar's centre of gravity (c. of g.) and lump-mass achieved virtually the same velocity profile during the impact with the bar element showing a small amplitude oscillatory motion. A 1% damping ratio was also included in the bar element which damped such oscillation. The velocity of the mass-spring model dropped steadily from the initial 7.78m/s to −0.5911m/s, the negative sign suggesting a rebound. The velocity of the bar-spring model oscillates with a very small amplitude to a final velocity of -0.6128m/s. It is obvious that both the bar and the lumped mass has reached almost the same final rebound velocity. Rebound is possible in these models because the springs have unloading stiffnesses. If the springs are of rigid-perfectly plastic nature then no rebound is possible and the coefficient of restitution would be zero. The coefficients of restitution for the two models considered here are very small, about 0.07, which is typical for high speed collisions of heavy objects. The unloading elastic response in an interface has only minor effects on the energy distribution along the colliding rakes of trains and will be discussed in detail later in Chapter 4.

Figure 3.6a shows the acceleration time history for both models. As expected, the bar exhibits high frequency content in this plot. The lumped mass attained the maximum deceleration very quickly and the constant collapse spring force maintained the deceleration throughout the impact event until the spring started to unload. Figure 3.6b shows the filtered bar's c. of g. deceleration and it becomes clear that the average deceleration in the bar's c. of g. could be represented by the smoother and better-behaved deceleration achieved by the lumped mass. The high frequency deceleration pulse and the smooth deceleration pulse as derived from both models in Figure 3.6a would later be used as input pulses for the dummy models.

Figure 3.7 shows the internal energy and kinetic energy variations during the course of impact for the mass-spring model. Figure 3.8 shows the same plot for the bar-spring model. The close resemblance of these two plots has made it necessary for them to be separately plotted so that they could be viewed individually. Kinetic energy of both models has been effectively converted to the internal strain energy in the springs although there is a very small amount of residual kinetic energy (about 0.6% of the total system energy) at the end of the impact due to rebound of the springs, causing the impacting entities to be separated from the rigid wall and travel in the opposite direction with a very small velocity. These results have shown that the bar stress wave does not significantly influence the energy dissipation activity by the spring. The kinetic energy associated with elastic bar vibration is negligible and so the bar-spring model could be replaced by the simpler mass-spring model where only energy dissipation is concerned.

3.3.4 PAMCRASH dummy analysis : mass-spring model Vs bar-spring model

The two deceleration pulses derived from the previous models are now used in the more complicated dummy models. The PAMCRASH dummy is a finite element model of a Hybrid III 50%th Male Dummy, which has been used extensively in the automobile industry. A more illustrative description concerning these dummy models is given in Chapters 7 and 8. For the current simulations, two dummies sitting diagonally opposite each other in a class 423 open bay sitting environment, as shown in Figure 3.9a, are given longitudinal pulses as derived from the previous models. The seats and floor are 'grouped' as a single rigid body in these models and the pulses are applied directly to these fixtures with the intention to view the dummies' response. The input pulse is not applied directly to the dummies but through the seats and floor. The dummies' interaction with the interior fixtures and with each other are defined by contact surfaces, each with a prescribed load-penetration characteristic. See Chapter 7 for more detail.

As mentioned earlier, the pulses are not directly applied to the dummies since they are 'decoupled' from the coach. Instead the applied pulses act through the soft seats which would be filtered somewhat before reaching the occupants. Comparisons of both pulses to the dummies are made in three areas : the animation sequence of the dummies, their head deceleration time history (for both striking and struck dummies) and their neck bending moment. All these are common assessments for injury potential used in the transport environment. Here after, the term 'dummy' and 'occupant' will be used interchangeably, and the dummy model with the bar-spring derived pulse will be known as the 'bar-spring' dummy model, and the dummy model with the mass-spring derived pulse will be known as the 'mass-spring' dummy model.

The animation sequence of the occupants for the two models is shown in Figure 3.9b. No significant difference could be seen and it seems reasonable to suggest that both input pulses, despite their differences, have produced identical results for both occupant models.

Figure 3.10 compares the head deceleration-time history for the striking occupants. The head of the striking occupant for both models engaged in a crash (which lasted about 80msec) with the struck occupant head from 220msec to about 300msec. There were no major differences between the two model predictions except that the 'mass-spring' striking occupant experienced a slightly higher deceleration towards the end of the simulation.

Figure 3.11 compares the head deceleration time history for the struck occupants. Again the two dummy models have shown similar results in this plot with the 'mass-spring' dummy model achieving a slightly higher deceleration between 280 to 320msec. It should be noted that the struck occupants were in contact with the seats for most of the time during the course of the simulations and thus were being exposed consistently to the input pulses. The similar initial response of both struck occupants (as shown in the first 200msec) of Figure 3.11 has suggested that much of the high frequency content in

the bar-spring model has been effectively filtered through the soft seat cushion before reaching the struck occupant. Note that the mass-spring dummy model has predicted a slightly higher head injury potential for both the striking and struck dummies.

Figures 3.12 and 3.13 show the neck bending moment of the striking and struck occupants for both models respectively. Both models showed very similar results for these plots and that the 'bar-spring' dummy model had a slightly higher neck bending moment for the struck occupant towards the end of the simulation. Otherwise the two graphs suggest that both dummy models have achieved almost the same neck bending results.

3.3.5 Conclusion

Although the bar-spring model could be viewed as an improvement to mass-spring model by considering stress waves in a one-dimensional fashion, both models had shown to produce the same energy dissipation results and the high frequency contents of the bar's deceleration pulse has no significant effects on the dummies' secondary impact. Hence, bar-spring improvement is seen to be superfluous for one-dimensional modelling. With this conclusion drawn, all future simulations of colliding rakes of trains will use the more user-friendly mass-spring models.

3.4 The sensitivity of mass-spring models to some inherent input parameters

3.4.1 Introduction

Revan [8] and Carney [3] have both conducted extensive parametric studies on train collisions using mass-spring models. However they have not considered the energy dissipative power ($\dot{E}$, the rate of internal energy dissipation) when they analysed their models. The extent to which damping, coach mass, wheel-track friction, spring's collapse force etc., influences $\dot{E}$ for a mass-spring model remains unknown. Such a study is required prior to analysing the behaviour of rakes of trains with multiple number of coaches; the important input parameters which govern the system must be identified. The system in this case is represented by a 'mass-spring-mass' model simulating a symmetric one-coach to one-coach impact. The 'behaviour' studied in this section concentrates on the dissipating power $\dot{E}$ of such mass-spring-mass systems during impacts. Figure 3.14 shows the baseline model for the current work.

For a one-coach to one-coach collision at a closing velocity of v, the collision energy absorbed E is described mathematically by Equation 3.3a [1] :

$$E = \frac{M_1 \cdot M_2}{M_1 + M_2} \frac{v^2}{2} \tag{3.3a}$$

where M_1 and M_2 are the coach masses. For this Chapter, M_1=M_2=M, then Equation 3.3a becomes :

$$E = \frac{Mv^2}{4} \tag{3.3b}$$

Substituting M=35000kg and v=15.56m/s and the collision energy to be absorbed for the interface shown in Figure 3.14 is 2.12MJ. For a constant collapse load of 2MN in the vehicle end crush zones connected in series (the spring) their combined collapse stroke should be 1.06m in order to absorb the collision energy at the impact velocity of 15.56m/s. At a higher impact velocity the passenger compartment would be infringed. The spring collapse characteristics are as shown in Figure 3.15.

For a mass-spring-mass impact model as shown in Figure 3.14, the spring absorbed energy at a rate prescribed by its load-deflection characteristics which could be viewed as the springs' dissipating power. Such power (in watts, J/s), will later be shown to be dependent on several parameters such as the coach mass, initial impact velocity, structural damping, spring's collapse force and external impulse. The first four parameters are inherent to the mass-spring-mass system and obviously the external impulse is an external influence to the system.

In order to investigate the effect of various input parameters, parametric studies were conducted. Input parameters were divided into two categories : those that are inherent to a mass-spring system, such as damping coefficient (C), coach's mass (M), spring's collapse characteristic, initial impact velocity (V), wheel-track friction coefficient (μ) etc.; and those that are caused by external factors, such as external impulses. External impulse to an interface could be provided by neighbouring interfaces if the train have multiple coaches and all of which are resiliently coupled together. Since the current section is limited to a one-coach to one-coach impact situation, the external impulse will be simulated by defining a pair of compressive time dependent nodal forces.

This section considers the inherent parameters in some detail. The external parameters would be addressed in the next section, Section 3.5. The baseline model shown in Figure 3.14 is a yardstick since its results will be compared with the rest of the parametric models. All the springs in the current section exhibit the load-deflection characteristic as shown in Figure 3.15, except for those parametric models with higher collapse spring force.

3.4.2 The use of kinematics for studying the inherent parameters.

The baseline impact configuration in Figure 3.14 shows that the constant collapse spring force will cause a constant deceleration for the impacting coach and, accordingly a constant acceleration for the impacted coach. If the initial elastic portion of the spring is ignored for the time being, the impacting coach (mass) would attain a constant deceleration immediately the end structure (spring) engaged with the other coach. Due to the inertia of the impacted coach, any distance progressed by the impacting coach is accompanied by a constant deceleration as a result of the spring's compression. The following mathematical relation will then apply to the coaches during the impact up to the point of time when the spring unloading is just about to occur. This signals the stability of the system and, if elastic unloading was permitted, the two coaches would be separated at this point. A subscript of "1" is adopted for the impacting coach and "2" for that which is impacted. Positive x-displacement direction is from left to right as shown in Figure 3.15. All symbols and notations used were as previously defined in Figure 3.2.

From Newton's second law and neglecting friction & damping for the time being,

$$M\ddot{x}_1 = -P_c$$

or
$$\ddot{x}_1 = -\frac{P_c}{M} \qquad (3.4a)$$

and
$$M\ddot{x}_2 = P_c$$

or
$$\ddot{x}_2 = \frac{P_c}{M} \qquad (3.4b)$$

Where P_c is the constant spring's collapse force. Note that the sign changes because the constant plastic collapse force is retarding the impacting coach but accelerating the impacted one. Recall that no elastic or unloading response is being considered here.

From kinematics & noting that the initial velocity of the impacted coach is zero,

$$x_1 = vt + \frac{1}{2}\ddot{x}_1 t^2 \qquad (3.5a)$$

and
$$x_2 = \frac{1}{2}\ddot{x}_2 t^2 \qquad (3.5b)$$

Internal energy dissipation,

$$E = P_c(x_1 - x_2) \tag{3.6}$$

Substituting 3.4 & 3.5 into 3.6,

$$E = P_c(vt - \frac{P_c}{M}t^2) \tag{3.7}$$

Differentiating 3.7 with respect to t

$$\dot{E} = P_c(v - 2\frac{P_c}{M}t) \tag{3.8}$$

The above analyses demonstrated that for a rigid-perfectly plastic spring-mass model without friction, $\dot{E}$ is linearly related to t, with an intercept of $P_c v$ and a slope of $-2\frac{P_c^2}{M}$. If the initial impact velocity is increased then it will raise the intercept without changing the slope. An increase in coach mass will reduce the slope without altering the intercept. An increase in constant collapse spring force will change both the intercept and the slope; the slope is very sensitive to P_c since a quadratic relationship is involved.

The above analysis could be modified to include wheel-track friction. The study of the wheel-track friction here is based on the assumption that the coefficient of friction remains constant throughout the duration of the impact. Equation 3.5 is still applicable in this case since the deceleration is still a constant. But Equations 3.4a and 3.4b both require a constant friction term, and these become :

$$M\ddot{x}_1 = -P_c - F$$

or

$$\ddot{x}_1 = -\frac{(P_c + F)}{M} \tag{3.9a}$$

and

$$M\ddot{x}_2 = P_c - F$$

or

$$\ddot{x}_2 = \frac{(P_c - F)}{M} \tag{3.9b}$$

Energy dissipation is now divided into two parts :

By the spring : $$E_s = (P_c)(x_1 - x_2) \tag{3.10a}$$

By friction : $$E_f = (F)(x_1 + x_2) \tag{3.10b}$$

Substituting Equations 3.9a,b & 3.5a,b into 3.10a,b gives :

$$E_s = (P_c)(vt - \frac{P_c}{M}t^2) \tag{3.11a}$$

$$E_f = (F)(vt - \frac{F}{M}t^2) \tag{3.11b}$$

Differentiating 3.11a,b gives :

$$\dot{E}_s = (P_c)(v - 2\frac{P_c}{M}t) \tag{3.12a}$$

$$\dot{E}_f = (F)(v - 2\frac{F}{M}t) \tag{3.12b}$$

Combining Equations 3.12a and 3.12b gives the total dissipating power,

$$\dot{E} = (P_c + F)v - 2\frac{(P_c^2 + F^2)}{M}t \tag{3.13}$$

Friction then, increases the intercept and steepens the slope. Inserting typical numerical figures into Equation 3.12 and recalling that $F=\mu Mg$, the sensitivity of the slope and intercept of Equation 3.13 to μ could be checked. Table 3.1 over the page, computes the slopes and intercepts for different μ for the baseline case, i.e. P_c=2MN, M=35000kg, V=15.56m/s, g=9.81m/s^2.

μ	Intercept of Equation 3.13	Slope of Equation 3.13
0	31.12E6	228.57E6
0.01	31.17E6	228.57E6
0.1	31.65E6	228.64E6
0.2	32.18E6	228.84E6
0.3	32.72E6	229.18E6
0.6	34.33E6	231.00E6
1	36.46E6	235.31E6

Table 3.1 : Effects of μ on the slopes and intercepts of Equation 3.13.

It is clear from Table 3.1 that the intercept of Equation 3.13 is more sensitive to μ since by varying μ from 0 to 1 (the two extremes) the intercept changes by about 17%. But the slope only varies 3% for the same variation range of μ. Frictional effects are small due to the difference in the order of magnitude between the spring collapse force and the friction force. Within the range of most practical cases (say $0.05<\mu<0.3$) friction has virtually negligible effect. This justifies the previous assumption that friction could be assumed as constant throughout the impact duration.

Damping is a little more involved mathematically since it depends on the relative velocity between the two coaches, and that introduces a velocity dependent force in Equation 3.4, which invalidates the constant deceleration relation that has been used in this section. For the baseline case with a damper between the coaches, the equations of motion neglecting the elastic and unloading response are :

$$M\ddot{x}_1 + C(\dot{x}_1 - \dot{x}_2) = -P_c \qquad (3.14a)$$

$$M\ddot{x}_2 - C(\dot{x}_1 - \dot{x}_2) = P_c \qquad (3.14b)$$

These could be solved easily by using DYNA3D, even if C is a non-linear function of the relative velocity between the two masses.

3.4.3 The parametric models : to verify previously derived mathematical results.

The previous section has shown that using simplified analyses (rigid-perfectly plastic with no damping), the effects of various inherent input parameters (coach mass, initial impact velocity, spring collapse force, wheel-track friction) on the spring dissipating power of the mass-spring-mass model can be understood. The actual parametric modelling is now performed and this is extended to include the initial spring elasticity. Unloading of springs would occur once the system is settling or has reached stability at the end of the impact process (i.e. exchange of momentum has been completed between the coaches and both move with the same final velocity, unloading of the spring would take place at such an instance which causes separation of the two colliding coaches) but it is not of interest for the current work to analyse results of the models during the restitution phase; only a small amount of energy is being recovered during restitution. Table 3.2 compiles the input variables for the parametric models studied here :

Model	Damping coefficient (kN/m/s)	Coefficient of friction	Mass of coach (Tonne)	Initial impact velocity (m/s)	Spring's collapse force (MN)
1 (Base line)	---	---	**35**	**15.56**	**2**
2	**45.8(1%)***	---	35	15.56	2
3	**22.9(0.5%)***	---	35	15.56	2
4	---	**0.3**	35	15.56	2
5	---	**0.6**	35	15.56	2
6	---	---	**25**	15.56	2
7	---	---	**45**	15.56	2
8	---	---	35	**13.56**	2
9	---	---	35	**17.56**	2
10	---	---	35	15.56	**4**
11	---	---	35	15.56	**8**

* The bracketed percentage shows the damping ratio of the model and the critical damping coefficient for the baseline case is 4.582 MN/m/s.

Table 3.2 : The parametric models for studying the inherent input parameters.

3.4.4 Results and findings

Effects of a damper

Figure 3.16 shows the results of dissipating power $\dot{E}$ against time t and it can be seen that damping increases the initial 'elastic' dissipation power of the system just prior to the yielding of the springs. After this there is a steady drop in dissipating power for all models. It is also clear that damping reduces the dissipating power non-linearly with time after the springs have yielded. Damping, therefore, modifies $\dot{E}$ such that it raises the initial 'elastic' dissipating power before the springs yield and thereafter non-linearly steepens the slope of the $\dot{E}$-t as the spring collapses. This is because damping is proportional to the relative velocity between the two colliding coaches and the initial relative velocity between the two coaches is a maximum, which then steadily reduces as the impact progresses. Such a velocity-dependent force is added to the spring force during the impact and a system without damper has no such additional force to assist the spring. Dampers, therefore assist in raising the initial dissipating power of the system and modify the dissipating power. Note that the area under a $\dot{E}$-t graph represent the internal energy absorbed by the system. Figure 3.17 is a plot of internal energy E against time t and, in this graph, it is clear that damping aids the system in achieving an earlier stability, this is easily understood since the systems with dampers have introduced an extra energy absorbing device to assist in energy dissipation.

If the rate of kinetic energy loss were plotted onto Figure 3.16, it would be symmetrical to the corresponding $\dot{E}$-t curves about the x-axis, showing that the kinetic energy is constantly converted to internal energy until stability is achieved. The stability for this system is attained when E is a maximum with no tendency to transfer any energy ($\dot{E}$=0) within the system. In the present case E=KE at the stable point and eventually the coaches moves with a velocity half that of the initial.

Figure 3.16, for the baseline case, has validated Equation 3.8, although in this graph there is an initial elastic response which 'disturbs' the rigid-perfectly plastic assumption made in the previous analysis. However, this initial elastic response quickly rises to the spring's collapse load and enters the constant load collapse phase which then fully agrees with the previous analysis.

Effects of the wheel/track friction

Wheel-track friction has introduced another means of energy dissipation which is 'extra' to the spring. To check the total energy dissipation power for the models, the rate of loss in KE is referred to instead of $\dot{E}$. Figure 3.18 shows the results of the rate of loss in KE Vs t for cases of various wheel-track friction. By considering only the plastic

collapse part of the curves, it is clear that friction has a negligible effect on the slope but it increases the intercept, which agrees with the previous analysis as summarised in Table 3.1. Note that for cases involving friction, there will be a small amount of 'residual' $\dot{E}$ at the end of the impact. This is because of the friction would continue to consume KE while the vehicles keep moving although the spring has completed its crushing process. An interesting point is observed concerning the amount of energy dissipated by the springs (E_s), as shown in Figure 3.19. All springs dissipated the same amount of energy (1.06MJ as in the baseline case) and all the models in the wheel-track friction parametric study achieved stability at the same time. The wheel/track friction did not aid the spring by saving some of its crushed distance nor did it assist the system in achieving an early stability as the damper does. Friction dissipates KE independently and with no apparent effect on the spring action. This agrees with Equation 12a which contains no friction term and 12b has no spring-force term, indicating mathematically that both are mutually independent as far as energy dissipation is concerned. Based on this point and the fact that friction has very little effects for most practical purposes, future modelling work reported in this thesis will not consider wheel/track friction.

Effects of the initial impact velocity

Figure 3.20 shows the results of $\dot{E}$-t for various cases of initial impact velocity. This graph shows that V has no effect on the slope of the graph during the plastic collapse phase but an increase in V increases its intercept, or increase the maximum elastic dissipating power of the system before plastic collapse, as predicted by Equation 3.8. Note however that because the coach's end crush zone has the capacity to dissipate only 1.06MJ of energy (a total of up to 2.12MJ per interface), any case with initial KE higher than 4.24MJ would imply the infringement of the passenger compartment. The collision energy to be absorbed for the base line case is just sufficient to fully crush the spring, so the lower initial velocity case of 13.56m/s only manages to partially crush the end crush zone. The higher initial velocity of 17.56m/s, however, has an initial KE of 5.4MJ and an extra 0.58MJ has to be dissipated in the passenger compartments. Hence Figure 3.20 shows a sudden 'jump' of $\dot{E}$ for the higher impact velocity case half way along its plastic collapse line. During which the previous analysis (Equation 3.8) could still be applied with a new initial velocity (the relative velocity of the coaches upon fully crushing the spring) and a new constant spring collapse load of 4MN. The collapse continues with a new slope and intercept of Equation 3.8 once passenger compartment is infringed.

Effects of the coach mass

Figure 3.21 shows the parametric effect of the coach mass. As predicted by Equation 3.8, with a slight modification due to initial elastic loading, an increase in the coach mass reduces the negative slope of the $\dot{E}$-t plot but has no effect on the intercept. For the 45

tonne coach collision, which is heavier than the baseline case, the initial *KE* is 5.45MJ and an extra 0.61MJ has to be absorbed by the passenger compartments. Hence, there is a similar jump on its plastic collapse line as previously encountered in the higher initial velocity case.

Effects of the spring collapse force

Figure 3.22 shows the results for various cases of springs' collapse force. As expected, an increase in the constant spring collapse force increases the intercept and slope of the $\dot{E}$-t plot. The slope is very sensitive to such increase in spring force.

To summarise the above : it is clear that the energy dissipating power during a collision is sensitive to the spring collapse force, initial velocity, coach mass and also system damping. Uni-directional wheel-track friction does not affect the spring dissipative power but it consumes kinetic energy independently to the spring. All parametric models have verified the mathematical results derived in Section 3.4.3.

3.5 The sensitivity of mass-spring model to some external parameters

3.5.1 Introduction

The previous section has illustrated the influence of some inherent parameters of the baseline case. The current section is dedicated exclusively to studying the effects of some external impulses on the system's $\dot{E}$-t plots. For two rakes of multiple coach trains involved in a collision, each interface could be represented by a mass-spring-mass model, and if the coaches are coupled resiliently, the neighbouring interfaces will inevitably deliver an impulse to the impact interface upon impact. In the following parametric analyses, the external impulse of an arbitrary force-time curve shape will be introduced to the two masses as a pair of compressive nodal loads. The external impulses investigated include :

(1) Magnitude of rectangular impulse;

(2) Magnitude of triangular impulse;

(3) Raising slope of a ramp impulse.

Note that attention is paid to the shape of the external impulses. This aids the later analyses in Chapter 5 where the different shapes of spring characteristics are studied.

3.5.2 The parametric models

The input variables in this series of parametric study are tabulated as follow :

Model	External impulse descriptions	Inherent input parameters
1 (Base line)	No external impulse	As in the base line case
R1	See Figure 3.23	
R2	See Figure 3.23	
R3	See Figure 3.23	
T1	See Figure 3.24	
T2	See Figure 3.24	
T3	See Figure 3.24	
S1	See Figure 3.25	
S2	See Figure 3.25	
S3	See Figure 3.25	
S4	See Figure 3.25	

Table 3.3 : Input parameters for studying models with external impulses.

3.5.3 Results and findings

Effects of the external rectangular impulses' magnitude

The kinematics analysis used previously can also be applied for cases of rectangular shaped external impulses since constant deceleration is applied to both masses. If the method described previously is followed through, then the following energy dissipating power against time relationship for the spring would be obtained :

$$\dot{E}_s = P_c[v + 2\frac{(I - P_c)}{M}t] \qquad (3.15)$$

here I is the external constant compressive force. The intercept of the plot is unchanged by I but it will modify the slope, considerably if I is of the same order as the spring force P_c. One important point to note is that Equation 3.15 is only applicable when there is a pair of constant-force impulses applied to the baseline model. Figure 3.26 has validated

Equation 3.15 for the various cases of rectangular impulses. Equation 3.15 also implies that the external impulses introduce an additional amount of energy to the system which the spring is expected to dissipate since no other means of energy dissipation is available. This is done by increasing the dissipating power of the spring which flattens the negative baseline slope of the curves as seen in Figure 3.26, both in the vehicle end crush zones and passenger compartments. The rectangular impulses have caused the infringement of passenger compartments due to extra amounts of energy introduced by the external impulses (recalling that the baseline case just managed to fully crush the spring) needed to be dissipated. The general effect of introducing a pair of compressive external impulses is thus seen to overload the spring.

Effects of the external triangular impulses' magnitude

External triangular compressive impulses have also altered the energy dissipating power as with the rectangular impulses, but in a non-linear manner as seen from Figure 3.27. All the external triangular impulses considered here have caused the infringement of their respective passenger compartments. Previously Revan [8] has commented that such short duration triangular impulses will not cause the infringement of passenger compartment as long as the peak force remains lower than the spring collapse force. The study here does not support such finding since model T2 has the same peak force as the spring collapse force and model T1 has a 25% lower peak force, yet both have shown infringement of passenger compartments, although for the model T1 such infringement was not severe due to its relatively small magnitude. It is the magnitude of the impulse (area under the external force-time loading curve) and not just the peak force of the impulse that governs whether the extra amount of energy will cause infringement of the passenger compartment.

Effects of the external ramp impulses' slope of loading

In Figure 3.28, external ramp impulses of various rising slopes are compared. All applications of ramp impulses were terminated before the baseline model's settling time. All of them increased the baseline dissipative power curve and overloaded the spring. An interesting feature is seen in the results of $\dot{E}$-t for model S3. This model applied a ramp load of zero slope which is equivalent to a rectangular external impulse with a constant force of 2MN, which is also the same as the spring collapse force. In Equation 3.15, if $I = P_c$, the slope of the $\dot{E}$-t line is zero! This is what model S3 has obtained in Figure 3.28. If the constant-force impulse has the force magnitude equal to the spring collapse force, then the dissipating power of the spring remains constant as long as the impulse is applied until infringement of passenger compartments occurs. The other ramp external impulses introduced non-linearity to the baseline dissipative power curve.

3.6 Conclusions

The following conclusions can be drawn from Chapter 3 :

(1) Mass-spring models are sufficient for one dimensional simulation of train collisions. Replacing lump masses with elastic bars has negligible effects on the occupant response and the total system energy absorption.

(2) Energy dissipative power of a one to one train collision with constant spring collapse load and without damping is found to be linearly dependent on time according to Equation 3.8.

(3) Damping introduces non-linearity to $\dot{E}$-t curves and cause early settling of the systems. However, it has limited effects on the total energy absorption of the mass-spring-mass system.

(4) Wheel track friction was found to have negligible effects on the springs' energy dissipating characteristics during train collisions.

(5) Coach mass, crush zone collapse load and impact velocity are very important parameters for studying the behaviour of vehicles in rakes because they dominate the energy absorption capacity during train collisions.

(6) The magnitude of the external rectangular impulse alters the dissipative power of a mass-spring-mass system according to Equation 3.15. It flattens the slopes of the $\dot{E}$-t curves but not the intercepts.

(7) The amount of extra energy passed by a pair of compressive external impulses to the mass-spring-mass system is related to the magnitude of the impulses (area under the external force-time loading history).

References

[1] Scholes, A., "Railway Passenger Vehicle Design Loads and Structural Crashworthiness.", Proc. IMechE., Vol. 201D, p 201, 1987.

[2] Scholes, A. and Lewis, J. L., "Development of Crashworthiness for Railway Vehicle Structures.", Proc. IMechE., Vol. 207F, p. 1, 1993.

[3] Chatterjee, S. and Carney, J. F., III, "Crash Energy Dissipation Management and Interior Crashworthiness in Passenger Trains.", Internal report, Vanderbilt Engineering Centre for Transportation Operations and Research, Vanderbilt University, Nashville, Tennessee, December 1994.

[4] Tong, P., "Rail Vehicle Structural Crashworthiness.", Chapter 14, Structural Crashworthiness, p. 397, (Jones, N. & Wierzbicki, T. eds.), Butterworth & Co. Ltd, London, 1983.

[5] OASYS, "DYNA3D Version 5.0.", User Manual, OASYS Ltd, London.

[6] Distin, K. W. and Smith, R. A., "Aspects of the Mass and Capacity of Trains.", Symposium on the Engineering Integrity in Rail Transport Systems (Tunna, J. M. ed.), EMAS, Warley, West Midland, p. 225, 1993.

[7] May, C. and Gray, L. W., "Vehicle Structure for the Intermediate Capacity Transit Vehicles.", Proc. IMechE. Conf. on Railway Vehicle Body Structures, Paper No. C285/85, p. 23, Mechanical Engineering Publications, London, 1985.

[8] Revan, A. J., "Crashworthiness Development : Parametric Study of Vehicles in Rakes.", British Rail Research Report, No. LR/VST/93/010, Derby, March 1993.

[9] ORE, "Dynamic Resistance of Drivers' Cabs to Frontal Impacts.", ORE-B165 Committee Report, No. 10, Utrecht, October 1991.

[10] Robinson, K. P., "Injury Criteria For Use in a Railway Environment.", British Rail Research Report, No. LR/VST/94/001, May 1994.

[11] Sutton, A. & Lewis, J. H., "Elastic/Plastic Interaction of Rakes of Rail Vehicles.", Structural Impact and Crashworthiness Vol. 2 (Morton J. ed.), Elsevier Applied Science Publications, London, p. 783, 1984.

Chapter 4

Preliminary study of the behaviour of rakes of trains including gaps and couplers

4.1 Introduction

The previous Chapter studied theoretically the effects of various input parameters such as coach mass, impact velocity, spring collapse load, wheel/track friction and various external impulses on the energy dissipative power of a one coach to one coach impact situation using a non-linear (piecewise linear) mass-spring model. This Chapter extends the study to include a greater number of coaches, gaps between adjacent coaches and also the couplers which connect these coaches. The current Chapter thus seeks a realistic non-linear mass-spring representation of the actual rakes of trains, paving the way for future works in this area.

Section 4.2 introduces the concept of a "gap" between coaches in a train and determines its theoretical optimum size for a given impact situation. The size of the gap has a strong influence over the collision energy distribution among the various interfaces of the two colliding trains. Section 4.3 includes the modelling of couplers into the non-linear mass-spring models. The couplers used in the models are of hydro-pneumatic design manufactured by Oleo International. These energy absorbing couplers are used extensively throughout the European railway operators both as couplers and buffers due to their superior energy absorbing capability at moderate impact speed and the ability to simultaneously produce almost constant deceleration. Section 4.4 investigates the effects of both impact velocity and gap size between coaches on energy distribution. Optimal gap size is dependent on impact closing velocity and hence this section aims to select the optimal gap for a range of impact velocities. Section 4.5 conducts a parametric study in an attempt to select the optimum damping coefficient for representing the train's structural damping. This is achieved by comparing parametric study results with that of the full scale collision test conducted recently by BR Research. Section 4.6 summarises the findings of this Chapter.

4.2 The "gap" between coaches within a rake

4.2.1 What is a "gap" in the context of rail vehicle crashworthiness?

Traditionally train coaches are connected resiliently by couplers. This enables external impulses to interact between neighbouring interfaces and modify the energy dissipative power of their vehicle end structures (springs) during a collision. This would inevitably cause uneven distribution of collision energy among the interfaces: those closer to the

impact plane would suffer more severely than the interfaces further away. This is not in accordance to the current BR crashworthiness philosophy. What is desirable, is that each coach, as it were, looks after itself. Theoretically, if a perfect gap exists between each connected pair of coaches which allows the energy absorption at the leading interface to be completed before the trailing coaches impact take place, then an idealised collision behaviour would be achieved which ensures that each coach within a rake is able to absorb its own kinetic energy. This in fact is making use of a gap to isolate each mass-spring-mass interface within a rake of train, thus disallowing external impulses to be introduced to each and every mass-spring-mass interface, leaving each interface dissipative power undisturbed. In this sense, such gaps are equivalent to loosely coupled coaches or slacks to be taken up before the vehicles ends engage each other [1] during a train collision. The size of the gaps has a direct bearing on the crashworthy behaviour of colliding trains, they can neither be too big nor too small [2].

4.2.2 The theoretical optimum gap size

The function of a gap is to isolate each interface within a train so that all vehicles absorb their own kinetic energy and thereby evenly distribute the absorbed energy among all the interfaces along the two collided rakes. How big should this gap be in theory for fulfilling this function?

Refer back to the mass-spring-mass impact scenario considered in the previous Chapter. The spring has an initial elastic loading behaviour followed by the constant force (2MN) plastic collapse which is the most important phase for the crashworthiness study since it absorbs the collision energy. Revan [3] has derived a theoretical optimum gap size for a symmetric collision between two rakes of similar multiple-coach train by applying simple kinematics and neglecting the elastic behaviour of the spring. He has shown this to be:

$$x_g = \frac{MV_0^2}{8P_c} \tag{4.1}$$

Where M = coach mass;

V_0^2 = impact velocity;

P_c = plastic collapse load for the rigid perfectly plastic spring;

x_g = Optimum gap for the given impact configuration.

Equation 4.1 could also be derived by interpreting the velocity-time graph for sequential collisions of masses against a rigid wall, this is discussed next.

Consider the vehicles A and B as shown in Figure 4.1a, both separated by a gap x_g and moving at an initial velocity V_0 with B leading a collision against a rigid wall W.

Collapsing of the vehicle structures is assumed to take place in a rigid-linear plastic manner without any elastic unloading when the impact has completed. The ideal situation for even impact energy distribution would be achieved if vehicle A closed up the gap between itself and vehicle B (x_g) at exactly the same moment when B has just completed its impact activity with W. This optimal gap size is in fact the shaded area in Figure 4.1b, which shows the velocity-time history of both vehicles right from the instant when B touches W. The shaded area represents the difference in distance travelled by A and B in time t_g, the time when B has just completed its collision with W. The time t_g could be obtained by the following kinematics relation :

$$0 = V_0 + at_g \tag{4.2}$$

On the understanding that the final velocity is zero for B after the collision with W is completed; 'a' in Equation 4.2 could be calculated directly by Newton's second law :

$$a = \frac{P_c}{M} \tag{4.3}$$

where M is the mass of B and P_c is its constant crushing force. The area x_g of the shaded region in Figure 4.1b is :

$$x_g = \frac{1}{2} V_0 t_g \tag{4.4}$$

Substituting Equations 4.2 and 4.3 into 4.4 gives :

$$x_g = \frac{1}{2} \frac{MV_0^2}{P_c} \tag{4.5}$$

On the understanding that 'a' is negative representing deceleration.

For collisions of two identical rakes with one initially at rest and the other moving with an initial velocity of V_0, the final velocity would not be zero but $\frac{V_0}{2}$. The shaded area would then be :

$$x_g = V_0 t_g - \frac{1}{2}(\frac{V_0}{2} + V_0)t_g \tag{4.6}$$

And this is equal to :

$$x_g = \frac{MV_0^2}{8P_c} \tag{4.7}$$

Which is exactly the same as Equation 4.1 as derived by Revan.

So the theoretical optimum gap is dependent on the coach mass, impact velocity and the magnitude of the plastic collapse force, all of which were found previously to be important inherent parameters that have strong effects on the energy dissipative power of the mass-spring-mass system. It would seem that the theoretical optimum gap is impossible to achieve in practice since it has to vary as according to the impact velocity. Note that such a gap is highly sensitive to the initial impact velocity due to the V^2 term in Equation 4.7. The effects of impact velocity on energy distribution will later be illustrated in Section 4.4.

Equation 4.1 (or 4.7) is applicable only to springs with constant collapse force characteristics. If the plastic collapse force of the spring had not been a constant, e.g. linear hardening or softening characteristics, then a mass-spring-mass model with the respective spring's characteristics would have to be constructed and analysed by DYNA3D or other FE packages so as to check for the timings at which the various systems achieve equilibrium. This settling time will be used in determining the optimal gap size for models with non-constant spring force. The next Chapter would address such cases of non-linear springs.

4.2.3 The effects of the size of a gap on collision energy distribution among various coach interfaces.

To study the effects of gap size on the energy distributions along the interfaces in a rake, the multi-degree of freedom non-linear mass-spring models as shown in Table 4.1 (over the page) were constructed and analysed by DYNA3D.

Model name	Gap size (m)
Gap1	0
Gap2	0.25
Gap3 (optimal)	0.53
Gap4	0.75

Table 4.1 : The models for investigating the effects of gap size on the energy distribution among the interfaces within the colliding rakes of trains.

The spring characteristics, coach mass and impact velocity used for the models are as shown in Figure 4.2 and 4.3. This is a three moving coach to three stationary coach model instead of the previous Chapter's simpler one to one impact situation. By applying Equation 4.1, an optimum gap size of 0.53m is obtained for isolating each interface in Figure 4.2. There are altogether five interfaces in both rakes for this impact configuration. The gap in the impact interface (interface 1) serves only to delay the whole impact event and thus was ignored. The rest of the interfaces have such a gap.

Figure 4.4a shows the force-time histories for the various interfaces of the model Gap3 (the optimum gap size case). It is seen from this graph that due to the "tuned" gap being introduced to the system, all interfaces were self contained and independent of each other resulting in no infringement to any of the passenger compartments with interface 1 just managed to fully "consume" its end structure. Recall from the previous Chapter that the impact velocity of 15.56m/s was calculated so as to fully "consume" the vehicle end structures.

Figure 4.4b shows the energy dissipative power for the three interfaces in the impacting rake. The familiar triangular shape of $\dot{E}$-t is again seen here. In this case the impact interface (interface 1) was the first to complete its collision and did so without any disturbance from its neighbours. Almost immediately after interface 1 has settled and was halfway in unloading, interface 2 started its collision. This occurs at about 0.13sec when Figure 4.4a shows a "dip" in interface 1 force-time history indicating unloading was on its way but interrupted (reloading and return to its yield load of 2MN) by the simultaneous loading up to yield of interface 2. Unloading of interface 1 has the effect of separating the two leading coaches of both rakes and could create a velocity gradient between them and the reloading of interface 1 by its neighbour has caused a follow-up collision between these two leading coaches[2]. The severity of this follow-up collision depends on the velocity gradient. The velocity gradient is zero if unloading is not allowed, i.e. for rigid-perfectly plastic spring and the two coaches stay solidly together after impact. In Figure 4.4b, the tuned gap size for model Gap3 is seen to successfully isolate each interface so that collisions take place in one interface after another. The follow up collisions in each interface caused by its own unloading have incurred negligible additional damage. This is seen from the area under the $\dot{E}$-t curves.

For each interface, this area is much bigger during the main collision (the area under the triangle) than the area in the short "recesses" above the horizontal axis after the unloading of each interfaces has taken place which represents energy absorbed during the followed up collisions. The tuned gap has minimised this small additional damage incurred during the follow-up collisions.

Figure 4.4b has shown that the energy dissipated in interface 1 is about twice that of the rest of the interfaces. If this model was changed to a three-coach train hitting a rigid wall at an impact velocity of 7.78m/s (half that of model Gap3 but such a train is brought to rest after the impact), then all the interfaces including interface 1 in the impact plane would share equal amount of energy. This again could be explained in terms of velocity differential (relative velocity) between coaches. At interface 1, the initial relative velocity between the two leading coaches is 15.56m/s but for the rest of the interfaces the initial impact velocity is 7.78m/s. Figure 4.4c is a plot of "internal energy dissipated against relative velocity between adjacent coaches" for the three interfaces. This is actually a plot of relative displacement against relative velocity which resembles a phase plot (velocity against displacement) used commonly in non-linear dynamic analyses. The curves in Figure 4.4c are the trajectories of the various interfaces in these phase plots. Here it can be seen that the tuned gap actually "forces" the coaches in the intermediate interfaces (interfaces 2 & 3) to collide at an initial relative velocity close to 7.78m/s. The slight difference in path between the trajectory of interface 2 and 3 was due to the previously discussed unloading effect which slightly modifies their energy dissipative power. If unloading is not allowed, the relative velocity between adjacent coaches after the impact would be zero, but unloading and re-loading has caused follow-up collisions which lead to the small spirals towards the end of the trajectories. This has slightly altered the intended perfect even energy distribution pattern. Consider the case of three coach hitting a rigid wall at 7.78m/s, all the three interfaces' trajectories including interface 1 would then follow the trajectory paths of interface 2 and 3 in Figure 4.4c. This is because all interfaces in this case have an initial relative velocity of 7.78m/s between the coaches.

When no gap exists between the interfaces, the energy dissipation activities in these interfaces interact with their neighbours resulting in uneven energy distribution along the two rakes of train. This is shown in Figure 4.5b with $\dot{E}$-t curves demonstrating the disastrous effects of external impulses imposed by the trailing interface to the leading one. These modified both their dissipative powers in such a way that a grossly uneven energy distribution is achieved. The phase plots in Figure 4.5c have shown that for gapless impact between two rakes of resiliently coupled train, the intermediate interfaces do not project their trajectories from an initial relative velocity of 7.78m/s as in the optimal gap case, but from zero relative velocity. This has modified their ideal trajectory paths resulting in relieving those interfaces further away from the impact plane from their energy absorbing task and simultaneously overloading the impact interface. Figure 4.5a shows the force-time histories for the various interfaces of this model. The impact interface in this case has shown to sustain the severest punishment and penetrated about 0.61m into the passenger compartment. About 76% of the total system internal energy is being absorbed in interface 1 with the remaining 24% being shared by the two interface 2 (one in the impacting rake and one in the impacted rake).

Interface 3 has not absorbed any energy for this gapless model. From Figure 4.5a, it can also be seen that interface 3 had not even yielded and thus it was behaving elastically throughout the whole collision process. The unevenness of energy distribution for this model could be improved if a small gap was introduced to the intermediate interfaces such as those in model Gap2.

Figure 4.6b shows the interfaces' $\dot{E}$-t curves for the model Gap2. Still the impact interface has shouldered most of the total internal energy of the system but interface 3 has at least yielded (see Figure 4.6a) and absorbed some portion of the energy. Insufficient gap has again caused external impulses to be imposed by the trailing interface to the leading one which modified both their energy dissipative power as seen in the overlapping of $\dot{E}$-t curves in Figure 4.6b. So far we have seen the uneven energy distribution results from insufficient gap size, what if the gap is bigger than the optimum size (i.e. too big)?

Figure 4.7b shows the $\dot{E}$-t for model Gap4. In terms of energy distribution, this is better than any of the cases which has insufficient gap size. But still an uneven energy distribution is observed. This can again be explained by the follow-up collisions caused by unloading of the interfaces. Due to the large gap between its neighbour (interface 2), interface 1 has dissipated energy independently and was allowed to completely unload after fully crushing its spring (see Figure 4.7a). This introduced a relative velocity between the two coaches in interface 1, which would allow a follow-up collision when an external impulse is delivered by the subsequent impact of its neighbours. Such follow-up collisions are similar to those found in the model Gp3, the only difference is that for the case of Gp3, the unloading interfaces were not fully unloaded when the follow-up collisions occurred and thus these follow-up collisions took place at small initial relative velocities. For the case in model Gap4, full unloading in all interfaces has created a larger relative velocity between the coaches for the follow-up collisions. Since interface 1 has fully consumed its vehicle end crush zones during the main impact, the additional energy dissipation in the follow-up collisions will have to infringe into the passenger compartment. The external impulse came too late in this case due to too large a gap size which also modified the energy distribution along the rakes.

Figure 4.8 shows a bar chart comparing the above discussed models on their energy distribution performance. This chart suggests that for a particular impact velocity, it is better to have a larger than optimal gap size rather than a smaller one. This has prompted the idea of allocating a fairly low strength region at the ends of coaches for parking bicycles and prams. However, such arrangement entails a longer train and which inevitably incur extra cost to the railway operators. Figure 4.8 also supports the contention that intermediate interfaces absorb no more than half of the energy absorbed by interface 1 for symmetric collision. So to economise on train length, all future models (with constant collapse force) considered in this thesis will have their intermediate interfaces crush zone lengths half as long as those in interface 1.

4.3 The modelling of couplers

The introduction of a gap between the coaches is purely a theoretical aspect of the current crashworthiness philosophy for rail vehicles. No account has been taken of the effect of vehicle couplers which form an essential element of train longitudinal behaviour. For every intermediate interface, each of the two back-to-back vehicle ends has a coupler extended out to be matched and pivoted midway between them. As a service requirement, apart from satisfying the UIC proof load cases (see Chapter 2), these couplers should be able to cushion the coaches against the impacts during normal slow speed shunting operations and they must also provide longitudinal elasticity during traction and braking. Recently the BR fleet had been equipped with couplers which are of typical rubber stack design. This is a resilient drawgear which comprises of a series of rubber pads mounted between steel plates. By stacking the rubber pads on either side of a stiff mounting plate on the underframe, resilience in both buff and draw is achieved. The rubber stack design has typical exponential incremental force-displacement characteristics which makes them become almost solid beyond a compression of 50mm absorbing about 15kJ of collision energy. Such a coupler is adequate for slow speed collisions up to 2m/s but subject the vehicle underframe to high loads beyond this speed. For a fairly high speed collision, these couplers produce a resiliently connected effect which resembles the gapless articulated coaches as in the model Gap1. This was seen earlier to produce extremely uneven energy distribution along the colliding rakes having disastrous consequences for the coaches and passengers nearer the impact interface.

A compromise between the ideal perfect gap case and the resiliently rubber coupling case is found using hydro-pneumatic couplers which are designed to break away at a set load. This load is set at 1.2MN for the current research. The hydro-pneumatic couplers are manufactured by Oleo International which specialises in design and making of industrial buffers and couplers. The use of break away coupling design allows the Oleo coupler to absorb the necessary collision energy for its cushioning function at slow impact velocity : less than 4m/s absorbing 0.07MJ per coupler or 0.14MJ per interface. At higher impact speeds the load rises rapidly causing the coupler to break away, thus creating a temporary inter-vehicular gap which allows a short period of interface isolation before the vehicles ends come into contact.

Figure 4.9 shows the recent analytical energy distribution obtained by BRR[4] for a moving five-coach train colliding with a stationary five-coach train at 16.67m/s (60km/h). Due to symmetry, only the results of five interfaces in the impacting rake are shown. This figure demonstrates the superiority of the break away Oleo couplers over the traditional rubber stack couplers in providing a much more even distribution of energy along the two colliding rakes of trains.

4.3.1 The Oleo hydro-pneumatic couplers

Oleo coupler is one of the results of BR's "Post-Clapham" crashworthiness research programmes. Figure 4.10 shows the schematic construction of such coupler. The working principles are highlighted as follows :

(1) During collisions, the plunger is compressed into the cylinder displacing oil through the orifice into the reservoir;

(2) The oil filling up the reservoir moves the separator piston towards the buffer heads compressing the nitrogen gas contained in the chamber behind the separator piston;

(3) The squirting of oil through the orifice causes a pressure difference between the entrance and exit sides of the orifice thus developing a resistive force across the orifice wall to slow down the plunger movement. The intensity of this pressure difference (and thus the resistive force) is dependant on the relative speed of closure of the plunger and the shape (change of diameter along its length) of the metering pin. This produces a soft buffer to cushion low speed impacts gently and a high resistance to buffer closure required to cushion the impact at high speeds;

(4) After the slow speed collision (less than 4m/s) is completed, pressure at both sides of the orifice wall has sufficient time to attain equilibrium and recoil takes place. This is performed by the compressed nitrogen which returns the plunger to its original position by forcing the separator piston back to its initial location which in turn displaces the oil back to the oil chamber from the reservoir;

(5) At higher speed collisions, the couplers are designed to break away at a set load of 1.2MN. Thereby creating an isolation gap between the coaches before the vehicle ends contact each other.

Note that BR has chosen different types of Oleo couplers for installing in the impact interface (interface 1) and the intermediate interfaces (interface 2 & 3). The one for the impact interface is commercially coded as Oleo type 5SC-105 coupler with a maximum stroke of 110mm. Those in the intermediate interfaces are basically the same type but with the maximum stroke travel modified to a smaller 85mm. These couplers are capable of absorbing 0.07MJ for the impact between two 35tonne vehicles at a closing velocity of 4m/s, or 0.14MJ per interface.

4.3.2 Mathematical modelling of Oleo Hydro-Pneumatic couplers

The mathematical model describing the working principle of Oleo coupler is well documented in [5]. In [5], the Oleo coupler is mathematically described as a highly non-linear damper connected in parallel to a non-linear hydrogen spring. The damper generates a force which is directly proportional to the square of the relative velocity between its two ends divided by a term which is depended on the relative displacement. The hydrogen spring is actually a representation of the gas recoil unit which was found in [5] to have little energy absorption capability, it mainly serves as a recoil mechanism. T. Williams and G. E. Chalk [6] from Oleo International were approached for the detailed mathematical model which describes the couplers' characteristics for the BR trains. The author is obliged to them not to divulge any information regarding the actual couplers' mathematical model.

4.3.3 The PAMCRASH modelling of Oleo coupler

The analyses of non-linear mass-spring models which included the Oleo couplers were carried out by PAMCRASH. PAMCRASH is used here because it is capable of modelling the break away of non-linear dampers and springs. The simulation of breaking away of the element is invoked by a user defined limit of displacement (or force) for the case of spring/damper elements or strain (or stress) for the case of shell/beam/solid elements. When the limit is reached the element is eliminated from the model and the balance of analysis will continue without the participation of the broken elements. The schematic representation of the model is shown in Figure 4.11.

As shown in Figure 4.11, the combined vehicles' ends in each interface are now separated by a small centre mass. The separation of the vehicle end crush zones in each interface is necessary as it was not possible to combine the Oleo couplers' characteristics in series. The value of one tonne for the central mass was recommended by Revan [3]. The springs now have doubled the elastic stiffness and halved the crush zone length of the old "one spring per interface" model. For the old models, the spring actually averages out the structural stiffness of the two connecting vehicle end crush zones. Except in the impact interface, which is the same as the old one spring per interface models, all other vehicle ends now take the new configuration shown in Figure 4.11.

The parallel arrangement is chosen for the vehicle end structure (top spring) and the Oleo damper and hydrogen spring unit because of the presence of a gap between adjacent vehicle end structures. The gap makes the vehicle end crush zone "redundant" until they engage each other after the breaking away of the Oleo couplers and closing up of the gap. This parallel arrangement ignores the elastic force introduced by the vehicle end structures in series with that of the Oleo couplers. This will be addressed later in Section 4.3.6.

Another important feature in Figure 4.11 is the coach (the big mass) in interface 1. There is no Oleo coupler being modelled in this interface. This is justifiable since we do not expect the two colliding trains to engage their couplers at the impact point and that the high relative velocity experienced in the impact interface would shear away these couplers very quickly before they could absorb any significant amount of energy. Analyses would therefore start at the time when the two coaches in interface 1 just made contact. Hence this interface in Figure 4.11 is the same as the old "one spring per interface" models without any coupler. The spring characteristics are shown in Figures 4.12a and 4.12b.

4.3.4 Comparing the modelling configurations in Figures 4.2 & 4.11

To accommodate the modelling of Oleo couplers, the mass-spring model was modified from "mass-spring-mass" per interface to "big mass-spring-small mass-spring-big mass" per interface. Also a swap from the use of DYNA3D to PAMCRASH has to be made to suit the technicality involved in such a modification. So before proceeding further any work with the new modelling configuration with PAMCRASH, it was decided that a perfect gap (without coupler) model of it should be created so as to compare the results produced by those in the old modelling configuration with DYNA3D. Hence a model as in Figure 4.11 was created but without the hydrogen springs and Oleo dampers. This model is known as New1, and its results will be compared with that of model Gap3, the previous optimal gap model as in Figure 4.2.

Figure 4.13 shows the velocity-time histories of the three coaches in the impacting rake of both models. There is no significant difference between the two models except that the new configuration has introduced some small oscillatory motion for each coach just before they settle to the common final velocity. This was caused by the perturbation of the small centre mass in each interface. This has to be carefully interpreted for the future results of the coaches' velocity or deceleration time histories, especially when they are used as input pulses to dummy models. The deceleration pulse derived from these newly configured models needs to be "processed" so that the oscillations caused by the centre small mass are filtered before application.

Figure 4.14 shows the energy dissipation time histories of the two models. The energy dissipation of the two separated vehicle end crush zones in each interface for the model New1 were combined and then compared with the results produced by the model Gap3. Virtually no significant difference could be found as all three interfaces for both models achieved identical levels of energy dissipation at the end of their collisions.

4.3.5 Effects of vehicle structural elasticity on Oleo's coupler performance

The models that include the Oleo couplers studied so far have not considered the effects of the vehicle structural elasticity on the performance of the Oleo couplers. The couplers are mounted on the vehicle ends and hence an elastic media is connected in series with the Oleo damper and hydrogen spring unit. The effect of vehicle structural elasticity on Oleo couplers' performance was studied by Revan [3]. His model involved a more complex set-up to simulate a four-coach to four-coach impact with couplers breaking away at a slightly higher force of 1.5MN. All the interfaces of his model have sufficient energy absorbing capacity so that no infringement of passenger compartment occurred in his analyses. He also made use of contact surfaces in each interface for recording their impulse history. The interfaces' force-time history, as duplicated in Figure 4.15, shows the elastic oscillatory nature of the couplers' forces sustained at the various interfaces before the vehicle end structures engage. This elastic behaviour would not effect the overall energy dissipation pattern between the two colliding trains. Also, such elastic response has negligible bearing on the passenger safety as the previous study in Chapter 3 showed.

The new configuration could now be simulated by PAMCRASH with the cautionary note about the velocity and deceleration results which require special attention and treatment.

4.3.6 Models with Oleo couplers breaking away at 1.2MN

The model with Oleo couplers shown in Figure 4.11 is known as model Cp1. The various interfaces' energy absorption for model Cp1 are plotted against time in Figure 4.16. Each interface result is accompanied by the corresponding interface result obtained from the optimal gap model (model New1). Figure 4.17 shows the bar chart comparing the final energy distribution for the interfaces in the impacting rake (or the impacted rake since they are symmetric) between model Cp1 and New1.

It is clear from Figures 4.16 and 4.17 that the Oleo couplers in model Cp1 have modified the theoretical optimal-gap behaviour such that it produced an uneven energy distribution along the rake which overloaded the impact interface. This is not surprising as the couplers introduce external impulses between neighbouring interfaces. The breaking away of the couplers at 1.2MN has nevertheless created an isolation for all the interfaces to participate in the energy absorption. This break away force for couplers was provisionally studied by Revan [3]. He chose a value for the coupler break away force as 1.5MN for his mass-spring models which are identical to those studied here. The final decision for BR design [4] is to set a smaller coupler break away load of 1.2MN which is currently used in this Chapter. Setting of the coupler break away force has to consider both the normal shunting operation requirements and the high velocity collision requirement. The former needs to provide a sufficient level

of buffing and drafting force and the latter requires the couplers to break away as soon as possible with minimum energy absorption and to create a gap in each interface allowing their collisions to take place in isolation to each other. 1.2MN is the final compromise between the two in the current BR design guides.

Since the impact interface has an energy absorption capacity of only 2.12MJ for all the models considered so far, the extra energy dissipated in the impact interface of model Cp1 has caused the infringement of the passenger compartments. This is clearly seen in the force-time histories of various interfaces shown in Figure 4.18.

The force on interfaces 1 and 2 has on a few occasions reached 4MN during the impact. Such infringements of the high strength passenger compartments not only impose high magnitude deceleration pulses to the passengers within the coach but also may take away the survival space for passengers occupying space near the impact plane. So for model Cp1, its interfaces are required to have additional energy dissipative capacity in order not to infringe the passenger compartments. The length of the vehicle end crush zones would need to be extended or the crush zone collapse force increased with a shorter crush zone. At this stage, modification to model Cp1 is done by extending its crush zone length at interface 1. Increase of spring's collapse force will be discussed later in Chapter 6.

Hence another model, model Cp2, with all the interface end crush zones extended from 1.06m to 10m was created and the analysis repeated. The resulting interface forces for model Cp2 are plotted in Figure 4.19. The extension of the crush zone length for model Cp2 has "saved" the passenger compartment. Figure 4.20 is a bar chart comparing the energy distribution for all the three models. Table 4.2 summarises the various interfaces' crush distance for the three models.

Interface no.	Crush distance (m)		
	Model Cp1*	Model Cp2*	Model New1
Interface 1	1.28	1.33	1.06
Interface 2	0.58	0.51	0.53
Interface 3	0.23	0.23	0.51

*Note : Model Cp1 is the mass-spring-damper model without extension of the impact interface's crush zone length. Model Cp2 is the one with extended crush zone length.

Table 4.2 : The vehicle ends' crush distance for the various interfaces of the three models discussed.

The introduction of the Oleo couplers has caused the crush length for interface 1 in model Cp2 to increase by 26% over the model New1 (the theoretical perfect gap

model). Identical results (almost duplicated) were obtained by Revan [3] with his four to four collision model including Oleo couplers. The results shown in Table 4.2 have also suggested that there is a shift in the energy dissipation from interface 2 to interface 1 when the crush zones are extended. Suppressing the infringement of the passenger compartment in model Cp2 modified the dissipative power of interface 1 and 2 which caused a redistribution of dissipated energy for model Cp1 resulting in interface 1 bearing more share of energy. Interface 3 seems inert to the changes made by extending the crush zones, since interface 3 in both Cp1 and Cp2 have achieved the same crush.

Although model Cp1 has a slightly better evenness in energy distribution along the rake than model Cp2, it achieves this by infringing into the passenger compartment of interface 1. The interface energy dissipative power is governed by the collapse load of the spring. In this case model Cp1 has made use of the high collapse load of the passenger compartment to 'manipulate' the dissipative power of interface 1 and 2 to its advantage, 'forcing' interface 2 to dissipate more energy, at the expanse of some of its passengers' survival space.

Table 4.3 shows the energy dissipation in the couplers for the intermediate interfaces in the model Cp2. There are two couplers per interface and the table has compiled results for only one coupler in the respective interface.

	Energy absorbed in one hydrogen unit (MJ)	Energy absorbed in one hydraulic unit (MJ)	Total energy absorbed in the interface in model Cp2 (MJ)
Interface 2	0.0034(0.3%*)	0.0447 (4%*)	1.07
Interface 3	0.0074 (1.5%*)	0.0470 (9.3%*)	0.51

*Percentages shown in the brackets are the percentage of the total interface energy absorbed.

Table 4.3 : The proportion of energy absorbed by Oleo couplers.

Interface 1 is not included in Table 4.3 because it has no coupler. The average energy absorbed per coupler is 0.051MJ, majority of this is dissipated by the hydraulic action. As for the intermediate interfaces, the energy absorbed by the Oleo couplers does not exceed 10% of the respective interface energy. The hydrogen units do not absorb any significant amount of energy, which confirms the assumption made in [5].

4.4 The relationship between impact velocity, gap size and energy (crush distance) distribution for colliding trains

4.4.1 Introduction

According to Equation 4.1, the theoretical optimum gap size is dependent on the coach mass, vehicle end crush zones' collapse load and impact velocity. For the models considered so far this theoretical optimum gap without any coupler was found to be 0.53m per interface. Coach mass and crush zone collapse load are fixed parameters, however the impact velocity is a variable. The effects on energy distributions by including the Oleo couplers had been discussed, so it would seem timely now to check the relationships between impact velocity, gap size and energy distribution among the interfaces of the rake of train.

4.4.2 The selection of impact velocity range to be studied

The reasons for BR's choice of a limiting impact velocity of 40mph for a crashworthy rail vehicle were discussed in Chapter 2. All the currently designed crashworthy vehicles should absorb at least 1MJ of collision energy per vehicle end below an impact velocity of 40mph (17.88m/s). This limiting velocity of 40mph was derived based on extensive statistical study of the past ten years accident data [7]. To summarise the study, more than 60% of past train accident fatalities were caused during end-on collisions and almost all of these occurred at an impact velocity below 40mph. In fact it was found that if derailments (which usually occur during impacts at higher velocity than 40mph) excluded from the past rail vehicle accidents, then end-on collisions under 40mph were the single most important type of accident that involves fatalities and major injuries, especially to the crew members. Hence, in line with such BR statistical data, maximum impact velocity for crashworthiness studies is set at no more than 40mph (17.88m/s).

One of the early BR research objectives for improving rail vehicle crashworthiness was to install energy absorbing couplers such as the Oleo couplers. All current BR crashworthy vehicles are installed with Oleo couplers which equip them to absorb collision energy up to an impact velocity of 4m/s without any structural damage. The couplers are self recoverable after such low velocity collisions. At a higher impact velocity the couplers would shear away via bolts that designed to shear away at a limit force. The shearing action creates a temporary gap before the vehicle ends come into contact.

The chosen range of impact velocity to be studied is thus between 4m/s to 17.88m/s. Five impact velocities were selected : 13.24m/s (30mph), 14.67m/s (33mph) 15.56m/s (35mph), 16.45m/s (37mph) and 17.88m/s (40mph).

4.4.3 The parametric models

Parametric models for studying the effects of impact velocity and gap size on energy distributions along the colliding rakes are tabulated in Table 4.4 :

Model name	Gap size (m)	Impact velocity	Remark
Iv40Gp70	0.70	40mph (17.88m/s)	All models have their impact interface's crush zone extended to 10m so that no penetration of passenger compartment could take place at any interface in these models.
Iv40Gp59	0.59	40mph	
Iv40Gp53	0.53	40mph	
Iv40Gp47	0.47	40mph	
Iv40Gp38	0.38	40mph	
Iv37Gp70	0.70	37mph (16.45m/s)	
Iv37Gp59	0.59	37mph	
Iv37Gp53	0.53	37mph	
Iv37Gp47	0.47	37mph	
Iv37Gp38	0.38	37mph	
Iv35Gp70	0.70	35mph (15.56m/s)	
Iv35Gp59	0.59	35mph	
Iv35Gp53 (Cp2)	0.53	35mph	
Iv35Gp47	0.47	35mph	
Iv35Gp38	0.38	35mph	
Iv33Gp70	0.70	33mph (14.67m/s)	
Iv33Gp59	0.59	33mph	
Iv33Gp53	0.53	33mph	
Iv33Gp47	0.47	33mph	
Iv33Gp38	0.38	33mph	
Iv30Gp70	0.70	30mph (13.24m/s)	
Iv30Gp59	0.59	30mph	
Iv30Gp53	0.53	30mph	
Iv30Gp47	0.47	30mph	
Iv30Gp38	0.38	30mph	

Table 4.4 : The parametric models for investigating the relationship between impact velocity, gap size and energy distribution.

Before discussing their results, there are some points about Table 4.4 which need to be clarified. Firstly, with the increase in impact velocity from 15.56m/s (which has been studied so far) to 17.88m/s, there is a corresponding increase in collision energy to be dissipated. This will involve the penetrations of passenger compartments in interface 1 if the crush zone of the previous model Cp1 is used. Thus, interface 1 (impact interface) of all models have their crush zone extended to 10m. This is to prevent any infringement of passenger compartments which would then allow the results from all models to be compared on equal footing not involving the passenger compartments. Secondly, the gap size of 0.70m, 0.59m, 0.47m and 0.38m are calculated based on Equation 4.1 for the impact velocity of 17.88m/s, 16.45m/s, 14.67m/s and 13.24m/s respectively. Hence they represent the optimal gap size (without coupler) for these velocities. Thirdly, the term "gap size" will from now on be used synonymously to "inter-vehicular distance" as there are actually no gaps between vehicles since they are connected by Oleo couplers. Finally, the naming of all the models follow the convention of Iv(xx)Gp(yy), where (xx) is the model's impact velocity in mph and (yy) is its gap size to the nearest centimetre.

4.4.4 Models with different gap sizes but the same impact velocity

Figures 4.21 to 4.25 show the crush distributions for the three interfaces of all the models, grouped in the five different initial velocity series : the Iv30, the Iv33, the Iv35, the Iv37 and the Iv40 series.

Figure 4.21 shows the various interface results for the models in Iv40 series. The optimal gap size at 40mph is 0.70m, the two vertical straight lines in the graph are the ideal crush distance for the intermediate and impact interfaces at a 40mph collision. As expected, no model has achieved the ideal energy distribution. This is due to the presence of Oleo couplers. The best model in attaining even energy distribution in this Iv40 series is Iv40Gp59, for which gap size is tuned at 37mph. All models in interface 1 have achieved higher crush distance than the ideal case. It also has a turning point at a gap size of about 0.58m, and as the gap size diverge from this point, the crush increases. This has resulted in the model Iv40Gp38 being crushed the most in this series since its gap size is the furthest away from the turning point, indicating that too small a gap is unsuitable for high speed collision. The crush distance in interface 2 for all the models has approached the ideal line; even the smallest gap model which has deviated the most from the ideal line, has achieved about 85% of the ideal crush. Interface 3 for all models has shown not to crush more than half of the ideal crush distance. The smallest gap model has crushed the least at this interface. Interface 2 for all models has shouldered part of the energy "carried over" from interface 3 and also passed some of its own energy to interface 1. The overall results' comparison in Figure 4.20 for the three interfaces of the models New1, Cp1 and Cp2, has made it possible to suggest that interface 3 has passed some of its kinetic energy to interface 1 by a stress wave through interface 2.

Figure 4.22 shows the various interface crush results for the models in the Iv37 series. The results show similar trends as in the previous Iv40 series. The stationary point in this case is at a gap size of about 0.48m. Although the model Iv37Gp70 has the gap size furthest away from this point, it did not suffer the worse crush and has achieved almost identical results as the smallest gap model Iv37Gp38. Interface 2 again has shown to be the best interface in term of approaching ideal crush. Interface 3 has also shown not to crush more than half of the ideal crush, suggesting interface 3 has passed some of its kinetic energy to interface 1 through a stress wave activity.

Figure 4.23 shows the various interface crush results for the models in the Iv35 series. The stationary point is at a gap size of about 0.4m. The model with the biggest gap size (furthest away from the stationary point) has crush the most in interface 1 and least in interface 2 and 3. Other observations are much the same as the two previous discussed series : interface 2 has attained the closest results to the ideal case and interface 3 has not crushed more than half of the ideal crush distance.

At this point, it is possible to draw a very obvious conclusion from the results of the three series : All 'best behaved' models have their gap size consistently about 0.12m smaller than the tuned gap at the respective impact velocity. With this noted trend, the crush results in the Iv33 series could expect to have a turning point at a gap size of about 0.35m, which is too small to be shown in the current parametric study. Figure 4.24 however did show that the most even energy distributing model for Iv33 series is the smallest gap model and not the tuned gap model Iv33Gp49. This has in a sense supported the above contention that the best behaved model has a gap smaller than the tuned gap. All interfaces show a general trend that as the gap size increases, the crush distances deviate from the ideal lines. So the worst energy distributing model is the biggest gap model Iv33Gp70.

Finally, Figure 4.25 has shown very similar results to Figure 4.24. Again all interfaces has shown a general trend that as the gap size increases, the crush distances deviate from the ideal lines. The worst energy distributing model is again the biggest gap model Iv33Gp70, suggesting that too big a gap is not suitable for fairly slow velocity impact. Note that the best behaved model in this case is the tuned gap model Iv30Gp38, which coincidentally has the smallest gap size. The turning point in this Iv30 series is believed to be about 0.26m. It should be noted that Iv30 series has the lowest initial kinetic energy which made interface 1 of all its models crush considerably less than the other series. Other observations are much the same as previously discussed series.

To summarise the findings, it was found that uneven energy or crush distribution occurs on all models. The theoretical optimal energy distribution is thus not achievable for any model with couplers installed. The couplers have also 'moved' the optimal gap down by 0.12m for collisions within the impact velocity range of 30-40mph. Interface 2 is the best interface for attaining optimal crush results. Interface 3, being at the free end, has suffered the least damage. Too big a gap is not suitable for slow velocity

impact and too small a gap is no good for high velocity impact. The analyses for the above models with different gap sizes but the same impact velocity have shown that a gap size between 0.53m to 0.59m would be suitable for the selected range of impact velocity of 30-40mph. The inter-vehicular distance selected for the BR crashworthy vehicles used in the October 1994 full scale collision test was 0.54m; this would be discussed in detail later.

A repeat analyses of the 25 parametric models by re-categorising them into Gp38 series, Gp47 series, Gp53 series, Gp59 series and Gp70 series led to the same conclusions. It must be noted that the graph of initial velocity against crush distance must be normalised to enable comparison to be made since slower impact velocity would naturally crush less. Normalisation was done by dividing the actual crush to the ideal crush distance. Such analyses had indicated that the couplers has 'moved' the 'tuned velocity' for a particular gap size about 3mph upwards. The normalised plots for models with different impact velocities but the same gap size are shown in Figures 4.26-4.30.

4.4.5 Comparison of the crush distance achieved at impact interface by the various models

It is important for a designer to know the exact crush distance achieved by the various models at interface 1. Figure 4.31 is a graph which provides such information.

This graph has shown the extensive crush distance produced by the model Iv40Gp38, reiterating the unsuitability of having a small gap at high impact velocity. Models with lower impact velocities have enabled lesser kinetic energy to be dissipated as internal energy and thus models with low impact velocities have sustained less crush. The results have shown higher scattering for those data with smaller gaps indicating that the Oleo couplers have exercised much influence on the crush behaviour at small gaps, we have seen that at 40mph the smallest gap size model have produced the worst crush of all.

Figure 4.31 has also indicated that if all interface crush zones are 1.6m long (to be shared by both leading vehicles) with a constant collapse load of 2MN and a gap of 0.53m, a train with 35tonne coaches would be able to withstand any collision without involving the passenger compartments up to the impact velocity of 40mph (17.88m/s) provided no overriding or derailment occur. Maximum energy dissipating capacity per vehicle end is thus 1.6MJ in 0.8m, which is within BR specification. However it has also been shown that the intermediate interfaces could halve this crush zone length thus absorbing 0.8MJ in 0.4m, which also provides an economical design solution for shortening the train. During a recent full scale five-coach to five-coach collision test, BR applied this solution : their leading coaches in both rakes have a full length of a

designed vehicle end crush zone grafted on. The rest of the intermediate interfaces have only half the length of it.

4.5 The modelling of structural damping

The modelling work carried out so far has been ignoring structural damping. To model damping for a partially collapsing structure is very difficult and little is known to enable confident modelling representation in the mass-spring models. Nevertheless, a linear damper is still used here to represent structural damping. This form of representation through previous study (Chapter 3) has shown to alter the spring dissipative power (and hence the system kinematics). Damping ratio (ξ) is defined by :

$$\xi = \frac{C}{C_c} \qquad (4.8)$$

Where C is the damping coefficient (in N/m/s) of the damper and C_c is the critical damping coefficient of the mass-spring system, or $\sqrt{4(k)(M)}$. Typical damping ratio for various structural components and materials are [8, 9] :

Material	Approximate damping ratio
Steel spring	0.005
Natural rubber	0.05
Neoprene	0.05
Metal mesh	0.12
Felt and cork	0.06

Table 4.5 : Typical damping ratio for some components [8].

Construction	Approximate damping ratio
One piece	0.005-0.01
Welded	0.02
Riveted	0.03
Bolted	0.05

Table 4.6 : Typical damping ratio for some structural constructions [9].

From the previous tables, typical damping ratio for metallic structures is within 0.05 (5%) with one-piece component having much less damping than conventionally joined structures. In a crashworthy vehicle end structure, various joints (welded, adhesive, riveted and bolted joints) dominate the overall collapse mechanism and govern the load-deflection characteristics of the structure. Much research effort has been put in to gain a better understanding of this local behaviour and to enable blind computer modelling for simulation of their actual collapse mechanism.

In order to select the "right" amount of damping for the models, a recent BR full scale collision test results was used as a guide. By comparing the parametric computational results with the test results, a suitable damping coefficient was found.

4.5.1 General description of the BR October 1994 full scale collision test

Before proceeding to the parametric modelling, it is necessary to briefly describe the BR full scale collision test conducted on 28th October 1994. The test was conducted at the BR Old Derby test track just south of the old station at Widmerpool. This venue was chosen for a few strategic and safety reasons, the most important of which was that it has a very long straight track (more than 2km). The test track is shown in Figure 4.32. A few check points installed with accurate speed check devices and recorders were established along the test route. Communication was maintained between all test crews involved.

During the test, a stationary rake of five coaches was stationed at the impact point as marked on Figure 4.32. The impacting rake is a similar five-coach train which was located some 4.5km away from the impact point. The impacting rake was coupled to a make-up vehicle with a Class 47 locomotive by means of a quick release coupler. The sequence of events was described in [4] and can be summarised as follows :

(1) The impacting rake was accelerated from the start point to achieve a particular speed V_1 upon entering the tunnel.

(2) Thereafter the train speed was allowed to fall to a second controlled speed V_2.

(3) Once this critical V_2 was achieved, full power was applied to compress the release coupler.

(4) The train then accelerated up to the release speed V_3 at the release point, 1km away from the impact point.

(5) The coupler release mechanism was activated only after final confirmation of achieving the critical V_3 at the release point.

(6) Once releasing the impacting test rake at the release point, the brakes on the locomotive and make-up vehicle were applied and the test rake coasted the final kilometre to collide with the stationary rake awaiting at the impact point at a closing

velocity of 60km/h (16.67m/s). Trail runs were conducted prior to actual test for establishing what V_1,V_2 and V_3 should be in order to achieve this final impact velocity.

Both rakes consist of five Mark I coach each weighing 35tonnes. Their vehicle ends were cut off and replaced with the new crashworthy structures. These vehicle end structures are designed to achieve a controlled collapse characteristic as shown on Figure 3.1 (Chapter 3). This characteristics has an energy dissipative capacity of 2.2MJ in 0.92m. Oleo couplers were used at all vehicle ends and the inter-vehicular distance (gap size) is 0.54m.

4.5.2 Parametric study for the selection of the best structural damping coefficient

The parametric models for the present damping study is tabulated as follows :

Model name	Damping ratio
Dp35	0.0035 (0.35%)
Dp50	0.0050 (0.50%)
Dp75	0.0075 (0.75%)
Note : Other input data are shown in the next paragraph.	

Table 4.7 : The parametric model for damping investigation.

The following information supplement the data as tabulated on Table 4.7 :

(1) Configuration of all models are as shown in Figure 4.11, except the number of coaches has increased to five, see Figure 4.33;

(2) Except for the impact interface, Oleo couplers were modelled for all other vehicle ends;

(3) The load-deflection characteristics for the springs is as shown in Figure 3.1;

(4) Gap per interface is 0.54m (0.27m per vehicle end);

(5) Impact velocity V_0 is 16.67m/s (60km/h);

(6) Damping is represented by a linear damper in parallel to the vehicle end crush zone in Figure 4.11;

(7) Couplers break away at 1.2MN;

(8) Wheel-track friction is ignored.

The labelling and arrangement of the two rakes comprising coach a - e in the moving rake and 1 - 5 in the stationary rake are shown Figure 4.33.

Figure 4.34-4.36 shows the velocity-time histories for the various coaches in model Dp35, Dp50 and Dp75 respectively. Damping is seen to have the effect of shifting the velocity-time curves of various coaches to the left causing early settling of the system. Damping has helped to dissipate energy in the various interfaces resulting in earlier settling for these interfaces. All models have demonstrated a fair degree of correlation to the test data. The best model is Dp35 with all its coaches' velocity curves matching quite closely to those of the test.

Figures 4.37-4.39 show the bar charts comparing the various models' crush results with those obtained from the test. The following observations could be made for these charts :

(1) Interface 1, being in the impact plane, has shouldered most of the dissipated energy in the system, about twice as much compared to interface 2.

(2) Next to the impact interface, the intermediate interfaces (2s, 2m, 3s, 3m, 4s & 4m) constitute a region of fairly constant energy distribution although there is a trend of slight drop in energy dissipation as these interfaces move further away from the impact plane.

(3) The fairly even energy distribution region is terminated once it reaches a free end of a rake, i.e. the furthest interface (interface 5s and 5m) from the impact plane. There is no trailing interface attached to the free ends and hence these interfaces are exempted from receiving any external impulse.

(4) All interface crushing results produced by the models are more than those of the test.

It was seen that raising the damping has the tendency of matching the computational crush results with those of the test. However, care has to be taken not to "over-damp" the system just to correlate these crush results. In this respect, the coaches velocity-time histories in Figures 4.34 to 4.36 can be used to check the suitable amount of damping. Too much of damping would 'veer' the velocity curves away from the actual test results. Hence both crush results and velocity-time curves have to complement one another during this analysis. The best model to correlate with the test results is the model Dp50, which matches reasonably well with both the crush distance and velocity-time history. Dp75 is thought to be a little bit over-damped since its velocity-time

histories for the various coaches have deviated somewhat from the corresponding test curves. Dp35 seems slightly under-damped although it best matches the velocity-time histories but its interface crush distances have not matched those of the test quite as well as the other models.

The unsymmetrical interface crush results in the impacting and impacted rakes has suggested that the actual collapse mode for the coaches during the test did not follow strictly according to the load-deflection curve of Figure 3.1. The irregular velocity curve shapes obtained by the test have also supported the contention that some experimental deviations from the ideal have arisen during the test. Also dry friction which occurred during the tearing and rubbing contacts in the various joints and buckling structures is not easily modelled in the one dimensional spring-mass models. This is thought to be one of the reasons that the computed results of crushing for all models has consistently shown to be higher than the actual test crushing results.

Apart from frictional effects which are difficult to include in the one-dimensional mass-spring models, another reason for the computed crushed results to consistently exaggerate the experimental one, is due to the dynamic enhancement of crush zone collapse forces. The input load-deflection characteristics for the springs in all the models discussed so far had been derived from static crush tests. During impact the crush zones would collapse at slightly higher forces depending on the strain rates involved. It was found in reference [10] that the actual collapse force for the impact interface during the test was 21% higher than the static case and 13% on the average for the intermediate interfaces. With these simplified dynamic enhancement factors as 'corrections' to the relevant input data for the model Dp50, the crush results for such dynamically enhanced model is shown in Figure 4.40. Better correlations to the actual test results for all the computed interfaces' crush are seen, but still the computed results have slightly exaggerated those from the actual test.

Figure 4.41 displays the results of total energy absorbed in the various interfaces shown together with the interface damping energy for the non-dynamically enhanced models. Damping energies for all interfaces are consistently one order of magnitude lower than the corresponding energy dissipated through structural collapse. Interface 1 has the most damping energy dissipated since this is the interface with the highest initial relative velocity in the whole rake.

Damping is an improved feature in the mass-spring models. With the aid of actual BR test results, linear dampers were seen to model structural damping fairly accurately within the range of damping ratio of 0.0035 to 0.005. A suitable damping ratio was seen to be 0.005, and was employed for future investigations in this thesis.

4.6 Conclusions

The following conclusions could be drawn from the material covered in this Chapter :

(1) The optimal gap model with even energy distribution along a rake is a theoretical ideal not achievable in practice. Couplers in a train would deliver external impulses to the neighbouring interfaces thereby modifying their energy dissipative power and cause those interfaces located nearer to the impact interface to sustain more damage than those further away.

(2) Unloading of collapsed springs could lead to subsequent follow-up collisions if the gap size is too big. From a purely energy distribution point of view, it is better to have a bigger gap rather than a smaller one.

(3) Oleo couplers can be modelled as a non-linear spring in parallel with a non-linear damper, but the vehicle ends must now be separated by a small mass. This small mass introduces perturbations in the velocity-time curves for the various coaches.

(4) Vehicle structural elasticity does not influence the Oleo couplers' performance in term of the system's energy dissipation. Elastic effects can be ignored.

(5) Uneven energy or crush distribution occurs in all models with Oleo couplers at any impact velocity and gap size. The couplers also 'moved' the optimal gap down by 0.12m for collisions within the impact velocity range of 30-40mph.

(6) For models with Oleo couplers, interface 2 is the best interface for attaining optimal crush results. Interface 3, being at the free end, has suffered the least damage. Interface 3 has passed some energy to interfaces 1 and 2 through stress wave transmission.

(7) Small gaps such as 0.38m are quite sensitive to impact velocity. At high impact velocity such as 37mph, the impact interface would suffer extensive damage with uneven crush being distributed along the rake. It was found that a gap size between 0.53m to 0.59m would be suitable for the selected impact velocity range of 30-40mph. At lower velocities, kinetic energy to be dissipated is much less (due to the V^2 term) and the vehicles do not sustain much damage even if the gap size is 'out of tuned'.

(8) The models with constant collapse spring force have shown that the intermediate interfaces could be designed to dissipate half the collision energy absorbed in the impact interface. This is because the impact interface has an initial approached velocity twice than that of the intermediate interfaces.

(9) If all the interface crush zone lengths (to be shared by both vehicle ends) is chosen as 1.6m with a constant collapse load of 2MN and a gap of 0.53m, a train with 35tonne coaches would be able to withstand any collision not involving the passenger compartments up to the impact velocity of 40mph (17.88m/s) provided no overriding or derailment occurs. Maximum energy dissipative capacity per vehicle end is thus 1.6MJ in 0.8m. The intermediate interfaces could halve this energy dissipative capacity but such a design would preclude the interchangeability of coaches within a train.

(10) Damping is an improved feature in the mass-spring models. By comparing calculations with actual BR test results, linear dampers were seen to model structural damping fairly accurately within the range of damping ratio of 0.0035 to 0.005. A suitable damping ratio was seen to be 0.005.

(11) Good correlation between the computed and test results has been obtained, indicating the usefulness of the one-dimensional mass-spring models. These models if used without strain rate enhancement of the collapse structure, over-predict the collapse distance and hence provide some degree of conservation in the design.

(12) With the aid of actual collision test results, a realistic model for representing the actual behaviour of collisions between two rakes of trains has been found. This experimentally verified model enhances confidence for future modelling to be carried out.

References

[1] Carney, J. F., III, "Rail Vehicle Crashworthiness Simulation-State of the Practice.", Internal Report, Vanderbilt Engineering Centre for Transportation Operations and Research, Vanderbilt University, Nashville, Tennessee, USA., March 1993.

[2] Chatterjee, S. and Carney, J. F., III, "Crash Energy Dissipation Management and Interior Crashworthiness.", Internal Report, Vanderbilt Engineering Centre for Transportation Operations and Research, Vanderbilt University, Nashville, Tennessee, USA., December 1994.

[3] Revan, A. J., "Crashworthiness Development : Parametric Study of Vehicles in Rakes.", British Rail Research Report, No. LR/VST/93/010, Derby, March 1993.

[4] Scholes, A., Lewis, J. H. & Rasaiah, W. G., "Crashworthiness Collision Tests.", British Rail Research Report, No. RR-STR-95-037, March 1995.

[5] Bradley, R., Gibson, R. D. & Cross, M., "Case Studies in Mathematical Modelling.", Pentech Press Limited, Plymouth, p.57, 1981.

[6] Notes supplied by Mr. T. Williams and G. E. Chalk of Oleo International, after a private communication in 18th. October 1994.

[7] Lewis, J. H., Rogers, T. C., Allison, D. M., "Crashworthiness Development : Analysis of Accidents, Casualties & Vehicle Damage in Train Accidents 1982-1991.", British Rail Research Report, No. LR/VST/093/017, Derby, March 1993.

[8] Baker, J. K., "Vibration Isolation.", Engineering Design Guide 13, Oxford University Press, Oxford, p. 13, 1975.

[9] Middleton, A. H., "Mechinery Noise.", Engineering Design Guide 22, Oxford University Press, Oxford, p. 9 1977.

[10] Lewis, J. H. & Rasaiah, W. G., "Dynamic Tests on Rakes of Crashworthy Vehicles.", British Rail Research Report, No. RR-STR-95-026, Derby, May 1995.

Chapter 5
The shape of load-deflection curves : without couplers

5.1 Introduction

In the last Chapter, the effects of gap sizes, couplers and linear dampers on energy distribution along colliding rakes was studied. This Chapter studies the effects of different shapes of spring load-deflection curves. For a hardening or softening spring, collapse takes place at variable decelerations and so it is necessary to first carry out a theoretical derivation of the optimum gap size. This is described in Section 5.2. Section 5.3 introduces the selected spring characteristics used in this Chapter based on the criteria of maximum force and deflection set by BR research. The model preparations for the parametric study of various spring characteristics are discussed in Section 5.4. Analyses and comparisons of their results are made in Section 5.5. Energy distribution among various interfaces is compared Section 5.6 discusses the findings of this Chapter. The next Chapter improves these models by including Oleo couplers.

Three shapes of spring collapse characteristics were considered in this Chapter :

(1) Springs with constant collapse force;
(2) Springs with an initial high peak collapse force followed by a lower constant collapse force, which is typical of current coach body designs;
(3) Springs with hardening or ramp collapse force characteristics.

5.2 Theoretical gap size for mass-spring models with hardening and softening spring characteristics

Equation 4.1 derived analytically by Revan [1] (and graphically by the author) for the optimal gap between colliding masses is only applicable to springs with constant collapse force, i.e. applicable to cases with a constant deceleration only. If a hardening or softening spring is encountered, a new equation has to be derived based on the same graphical kinematics principle for deriving Equation 4.1.

Consider two vehicles A and B as shown in Figure 5.1, separated by a gap x_g and both moving at an initial velocity V_0 with B leading a collision against a rigid wall W.

Collapsing of the vehicle structures is assumed to take place in a rigid-linear plastic manner without any elastic unloading when the impact has completed. The ideal situation for even impact energy distribution would be achieved if vehicle A closed up the gap between itself and vehicle B (x_g) at exactly the moment when B has just completed its impact activity with W. This optimal gap size is in fact the shaded area in Figure 5.2, which shows the velocity-time history of both vehicles right from the instant when B touches W. The shaded area represents the difference in distance travelled by A and B in time t_g, the time when B has just completed its collision with W. The time t_g could be obtained by running a mass-spring-wall model which is the moment when B is at rest after completion of the impact. The following formula :

$$\int_0^{t_g}(V_B)dt - (V_0 \cdot t_g) \tag{5.1}$$

then gives the required gap. Note that if the deceleration is constant, the velocity V_B would be a straight line in Figure 5.2 and the time t_g could then be calculated instead of running a mass-spring-wall model.

5.3 Selection of the shape of the spring load-deflection curves

It is pointless to study arbitrary spring collapse characteristics without imposing some practical constraints. The following are practical constraints imposed in the current work:

(1) BR specifications stipulate that the maximum collapse force for the end crush zone must not exceed 3MN and 2MN is preferred;
(2) The specifications also restrict the maximum crush distance to 1m with an energy absorption of at least 1MJ;
(3) It was found in Chapter 4 that the energy absorbed at the impact interface is 1.6MJ per vehicle end (each collapsing at a constant 2MN) for 35tonne coaches connected by Oleo couplers during a symmetric collision at 40mph.

Combining the above conditions, one could see that the chosen force-deflection curves must lie in the 'corridor' between the 3MN and 1.6MN constant collapse force curves as shown in Figure 5.3. Note that 1.6MN is the force that allows a 1.6MJ energy absorption in 1m. It is also slightly higher than the 1.5MN minimum compressive force required to be sustained by the vehicle end at its coupler level.

With such an imposed 'corridor', five series of spring characteristics with a total of ten springs as shown in Figures 5.4 to 5.8, were selected for the next stage of research work. The reason for grouping all these curves into five series will soon become clear. Note that a few curves (such as cfy1) are repeated in some of the figures. All the springs shown in the figures are for the impact interface (interface 1) capable of absorbing 3.2MJ of energy before penetrating into the stronger passenger compartments. Previous Chapters have shown that the intermediate interfaces could absorb half this amount of energy. The settling time t_g for individual model was obtained by running the respective mass-spring-wall model. The optimal gap size x_g was then computed using the integral formula as mentioned earlier. Table 5.1 over the page tabulates the optimal gap size for the models considered in this Chapter. All the mass-spring-wall models have one 35tonne nodal mass connected to an fixed node (to simulate the rigid wall) by a non-linear spring with the mass hitting the spring and wall at an approach velocity of 8.33m/s (half of 16.67m/s). It should be noted that the three constant force collapse springs shown in Figure 5.4 could still use Equation 4.1 and hence it was not necessary to run their mass-spring-wall models for determining their optimal gap size. Table 5.1 should be referred to together with the appropriate figures.

Curve's name	t_g (sec)	x_g (m)	Remarks
cfy1 (also as rps1, ipd1 & iph1)*	--	0.760	See Fig. 5.4
cfy2	--	0.529	
cfy3	--	0.405	
rps2 (also as rpy1)×	0.150	0.592	See Fig. 5.5
rps3	0.126	0.478	
rpy2	0.111	0.443	See Fig. 5.7
iph2	0.180	0.757	See Fig. 5.8
ipd2 (also as iph3)▽	0.182	0.759	See Fig. 5.6
ipd3	0.168	0.746	
ipd4	0.146	0.672	

*Also refer to Figures 5.5, 5.6 and 5.8.
×Also refer to Figure 5.7.
▽Also refer to Figure 5.8.

Table 5.1 : The settling time of the mass-spring-wall models and their computed optimal gap size.

5.4 Parametric study of the shape of the springs' load-deflection curves : using mass-spring models with optimum gap size and no couplers

All the parametric models studied here have a three moving coaches to three stationary coaches configuration as in the previous Chapter. The initial impact velocity is set at 16.67m/s (60km/h). This is higher than the 15.56m/s used in the previous Chapters. Naming of coach and interface number remain the same as in Figure 4.2. Each coach is 35tonne. All models have their own gap as shown in Table 5.1. There are no couplers.

The ten models each with a distinct spring characteristic are grouped into five series as shown graphically in Figures 5.4 to 5.8. Each series has only one varying input parameter to the model which enables the parametric effects of the particular variable to be studied. Note that the figures shown are for the impacting interface only, i.e. interface 1. The intermediate interfaces take only half the energy dissipative capacity of these figures. Gaps are not shown on the figures. The gap sizes of various models are tabulated in Table 5.1. Models are identified by the name of its spring.

The constant collapse force series in Figure 5.4 has a variable yield force. All models in the ramp slope series as shown in Figure 5.5 have the same yield point but variable hardening slopes. The models in the softening deflection series in Figure 5.6 also share the same yield point but they collapse with different softening distances. Softening deflection is defined as the collapse-distance of a spring that proceeds with negative stiffness after yielding. A spring with constant yield force could thus be thought as having a zero softening deflection. The two models in the ramp force series in Figure 5.7 shared the same hardening slope but both collapse at different yield force levels. The models in the initial peak force series in Figure 5.8 share the same width of the

initial peak force but their initial peak force magnitudes are different. Note that iph1 (also cfy1) has zero initial peak force since it has a constant collapse force. Table 5.2 tabulates the five series of models with their parametric variables highlighted :

The constant yield force series	
Spring curve--cfy1	The yield force magnitude is the parametric variable in this series.
Spring curve--cfy2	
Spring curve--cfy3	
The ramp slope series	
Spring curve--rps1 (cfy1)	To study the hardening slope of the ramp force.
Spring curve--rps2	
Spring curve--rps3	
The ramp force series	
Spring curve--rpy1 (rps2)	To study the ramp force magnitude in the hardening collapse phase.
Spring curve--rpy2	
The initial peak force series	
Spring curve--iph1 (cfy1)	The initial peak force magnitude is the parametric variable.
Spring curve--iph2	
Spring curve--iph3	
The softening deflection series	
Spring curve--ipd1 (cfy1)	The softening deflection is the parametric variable.
Spring curve--ipd2 (iph2)	
Spring curve--ipd3	
Spring curve--ipd4	

Table 5.2 : The five series of parametric study and their respective parametric variables.

5.5 Results and discussions

5.5.1 The constant yield force (cfy) series

Figure 5.9 shows the bar chart comparing the energy absorbed in the various interfaces for the models in cfy series. The three models showed identical energy distributions among all the three interfaces although there are signs to suggest that a higher yield force tends to slightly overload the impact interface (interface 1). This could be explained by referring to the force-time graphs of the models cfy1, cfy2 and cfy3 as shown in Figures 5.10a, 5.10b and 5.10c respectively. Since all models have 'tuned' gaps the unloading of a leading interface coincides with the loading of its trailing interface and this takes place with a force differential 'F_d' as shown on the figures. A 'dip' is produced on these graphs whenever an interface is unloading. Unloading is allowed since elastic-plastic springs were used instead of the ideal rigid-perfectly plastic springs. The 'dips' on the force-time graphs were caused by the temporary unloading of the leading interfaces which were rapidly reloaded by the trailing

interfaces. Unloading of an interface upon completion of its primary impact sets up a small velocity gradient between its two masses thus making it vulnerable for a follow-up impact. This is what the reloading by its trailing interface offers. The higher the yield force of the spring the larger will be F_d which results in a more severe follow-up impact. Table 5.3 shows the effects of the follow-up impacts on the energy distribution along colliding rakes using the model cfy3 as a sample. Note that if rigid-perfectly plastic springs were used then the energy distribution would approach the ideal case as shown on the fifth row of Table 5.3.

Events	Energy absorbed in Interface 1 (MJ)	Energy absorbed in Interface 2 (MJ)	Energy absorbed in Interface 3 (MJ)
Primary impact	2.43	1.19	1.18
First follow-up impact	2.51	1.20	---
Second follow-up impact	2.53	---	---
Ideal energy absorbed	2.43	1.22	1.22
Percentage loss/gain of the final energy absorbed as compare to the ideal case	+4.1%	-1.6%	-3.3%

Table 5.3 : Energy absorbed during the follow-up impacts for the model cfy3.

It can be seen that interface 1 suffered two follow-up impacts and absorbed slightly more than its ideal share of energy relieving the other two interfaces.

5.5.2 The ramp slope (rps) series

Figure 5.11 shows the interface energy distribution bar chart for the models in the rps series. Again similar energy distribution pattern were observed for all models, although interface 2 has slightly relieved interface 1 by absorbing a little more energy when hardening springs were used.

Figures 5.12a and 5.12b shows the force-time history for the models rps2 and rps3 respectively. Note that the model rps1 is the same as cfy1, i.e. a special case in rps series with zero hardening slope. Oscillatory behaviour could be seen from these graphs with ramp force collapse springs. After interface 1 had completed its primary impact and started to unload, it was reloaded by interface 2 not with a constant but an increasing force. The loading force for interface 2 is always lower than the setting force of interface 1 because interface 2 is expected to absorb only half the amount of energy than interface 1 with a corresponding shorter crush distance. That for a ramp force collapse characteristic would imply a lower force than interface 1. Hence the force in interface 1 during its post-primary impact phase (as indicated in Figures 5.12a and 5.12b) was oscillating about the force produced in interface 2, trying to achieve interfacial equilibrium. While these two interfaces try to achieve equilibrium, energy is constantly being released and absorbed by their springs. When the force in interface 1 is greater than that of interface 2, external impulses will be set up against interface 2

and energy is passed from interface 1 to 2. The opposite applies if interface 2 has a greater force.

Figure 5.13 shows the graphs of dissipative power against time ($\dot{E}$-t) for interface 1. The area of a curve bounded between positive $\dot{E}$ and the t-axis indicates that energy is being absorbed by the spring in interface 1, and between negative $\dot{E}$ and the t-axis indicates energy is being released from the same spring. It can be seen that models with hardening springs had alternating two-way transactions of energy between interface 1 and its neighbour during the post-primary impact period (after 0.12sec for rps3 and after 0.14sec for rps2). The steeper the ramp slope, the larger the amplitude of such $\dot{E}$ oscillation. However, since the total area above the t-axis approximately equals the total area below the t-axis during the oscillating phase of the graphs, the energy released and absorbed by interface 1 during this period was approximately equal for rps2 and rps3. Thus the final energy distribution for these models, like their counterparts in the cfy series, also approaches the ideal case. The perturbations in these models were seen to be self correcting and did not cause any noticeable effects on the even energy distribution among all the interfaces.

5.5.3 The softening distance (ipd) series

Figure 5.14 shows the interface energy distributions for the models in the ipd series. It can be seen that an extended softening deflection has greatly modified the ideal energy distribution even though the models have 'tuned' gaps. All interface 1 and in some cases interface 2 have been crushed more than the ideal case. Infringement of passenger compartments occurred for model ipd3 and ipd4.

Figures 5.15a to 5.15c shows the interface force-time history for model ipd2 to ipd4 respectively. Note that ipd1 is the same as cfy1, i.e. a special case in the ipd series with zero softening deflection.

Refer to Figure 5.15a. The model ipd2 has a softening deflection of only 0.1m, i.e. collapse from the initial yield load of 3MN to the settling load of 1.6MN in 0.1m. The initial peak load of the springs caused the initial loading of the trailing interface to exert a larger force on the leading interface, indicated as ΔF Figure 5.15a. Such ΔF would deliver a triangular external impulse to the leading interface, thus overloading it. However, since the initial peak load settled rather rapidly for ipd2 so the duration of the external impulse was short and the evenness of interface energy distribution for ipd2 was not too greatly effected as seen in Figure 5.14.

The force-time history of ipd3 as shown in Figure 5.15b has more violent responses from the various interfaces. The softening distance is now 0.5m, 4 times larger than ipd2. This prolonged the effective duration of ΔF as indicated by Δt in Figure 5.15b. A prolonged external impulse (now trapezoidal instead of triangular in shape) delivered by a trailing to its leading interface would greatly overload the leading interface and upset the ideal energy distribution pattern. Note that interface 3 did not settle to the final 1.6MN, it was are still within the softening phase of the spring because it had been greatly relieved by interface 1 and crushed much less than the ideal case. Thus we

see that the model ipd3 in Figure 5.14 showed highly uneven energy distribution pattern with interface 1 absorbing 3.21MJ (about a third more than the ideal case) and interface 3 only 0.61MJ (about 50% of the ideal case). Slight infringement of passenger compartment in interface 1 has occurred.

A similar event took place in the model ipd4 as shown in the force-time history in Figure 5.15c, only that Δt (the duration of the external impulse) is made longer by the extensively large softening deflection of 1m, almost 70% of the total length of the crush zone. In this case, both interface 2 and 3 did not settle to the final 1.6MN. Both springs were still in the softening phase of their springs.

Figure 5.16 shows the graphs of $\dot{E}$-t for interface 1 of various models in ipd series. Note that the softening part of the graphs is non-linear and concave towards the $\dot{E}$-axis. These graphs basically confirm the negative effects on energy distribution along colliding rakes introduced by the softening springs.

From the interface energy distribution pattern shown in Figure 5.14 we can conclude that multi-coach trains with vehicle ends that soften extensively, have inherent energy distribution problems : the collision energy can not be evenly distributed along the whole train resulting in the leading coach absorbing most of the collision energy.

5.5.4 The ramp force (rpy) series

Figure 5.17 shows the interface energy distribution chart for the two models in the rpy series. This chart suggests that springs with the same hardening slope but different yield force level have virtually no effect on energy distribution along colliding rakes for no-coupler and 'tuned' gap cases. However, slight overloading in interface 1 can be seen for the model with higher yield force, i.e. rpy2. Note that the model rpy1 is the same as rps2 as discussed previously. This again is due to the greater F_d caused by the difference in force level when the leading interface was unloading and the trailing interface was about to load, causing a slightly more severe follow-up impact for the leading interface. Figure 5.18 which shows the force-time history for rpy2, if compared to Figure 5.12a which is for rpy1, illustrates this point. Both models showed similar force-time response for all the interfaces except that rpy2 achieved an earlier settling due to its higher level of collapse force.

5.5.5 The initial peak force (iph) series

Figure 5.19 compares the interface energy distribution for the models in the iph series. Note that iph1 is the same as cfy1 and is the special case of zero initial peak force. The other two models (one of which is iph3 which is the same as ipd2) have different peak forces but the same softening deflection of 0.1m. This chart suggests that the initial peak load would slightly upset the evenness of energy distribution among the interfaces and the higher the initial peak load the more interface 1 would be overloaded. This is not surprising as the initial peak load determines the magnitude of the force differential, ΔF, which in turn governs the magnitude of the external impulse to be delivered from the trailing interface to the leading one. Figure 5.20 shows the force-

time history of iph2. A comparison of ΔF with the previous Figure 5.15a, which shows the force-time history of iph3, would illustrate this point.

5.5.6 Can the model ipd4 be modified to improve its energy distribution pattern?

We have seen that although ipd4 has a 'tuned' gap, due to the extensive softening deflection in the spring characteristics, it has a grossly uneven energy distribution. ipd4 could easily be improved by the model shown in Figure 5.21.

The interface energy distribution for mod4 is shown in Figure 5.22 with results from cfy16 and ipd4 included for comparison. The modification has virtually rectified the performance of ipd4 to the same level of cfy1. The force-time history for mod4 is shown on Figure 5.23. It is seen here that the settling force in interface 1 is the same as the constant yield force of interface 2. This eradicates the external impulse as observed in the model ipd4. The carefully 'tuned' gap for each interface has also ensured that all interfaces dissipated their collision energy in isolation to each other.

5.6 Conclusions

From the models studied in this Chapter, the following inferences can be drawn pertaining to the behaviour of rakes of coaches during collisions :

(1) It is possible to tune the size of the gap between coach interfaces to optimise the collision energy distribution along colliding rakes. This can be done for crush zones with constant collapse force, initial spike or ramp characteristics, but it cannot be done for crush zones with softening characteristic.

(2) Rakes of vehicles with crush zones that soften on impact have inherent energy distribution problems. Energy is absorbed largely in the leading vehicle. In this respect, it is desirable for softening crush zones to have as short a softening stroke as possible so as to settle to a constant collapse force quickly. Crush zones with this characteristic will have an initial spike.

(3) Higher constant yield force for vehicle crush zones has slightly increased the severity of damages to interfaces 1 and 2, interface 1 being the nearest to the impact plane.

(4) Crush zones with ramp collapse forces achieve a similar share of energy distribution along colliding rakes as those with constant collapse forces.

(5) Crush zones with hardening and constant collapse force behave similarly to an increase in the collapse force. There is an increase in the energy transferred to interfaces 1 and 2 resulting from the follow-up impacts of the other interfaces.

(6) Crush zones with a higher initial spiky peak force will deliver a larger triangular external impulse from the trailing interface to the leading interface when the former

started its primary impact. This has introduced a slight overloading for those interfaces that are closer to the impact plane.

(7) The interface located at the free ends (i.e. interface 3 for all models) only delivered impulses to its leading interfaces without receiving any in return. As a results, damage at the last interface would be reduced. For poor crush zone characteristics, such as one which softened over an extensive collapse distance, only about half of the ideal energy absorption may be expected in this interface.

(8) In a rake, the only interface that could afford to collapse with an extensive softening deflection is the impact interface (i.e. closest to the impact plane). The intermediate interfaces for such a rake should then collapse at a constant force equal to the settling force of the impact interface.

In the following Chapters, this research work will only study springs that collapse with hardening, constant yield force and initial spiky peak force characteristics.

Reference

[1] Revan, A. J., "Crashworthiness Development : Parametric Study of Vehicles in Rakes.", British Rail Research Report, No. LR/VST/93/010, Derby, March 1993.

Chapter 6
The shape of load-deflection curves : with Oleo couplers

6.1 Introduction

This Chapter improves some selected models from Chapter 5 by including Oleo couplers. The selection was based on evenness of energy distribution along the colliding rakes and all chosen models have springs with constant collapse force, ramp collapse force or initial high spiky peak characteristics. Section 6.2 described the parametric models chosen for the study of spring characteristics with Oleo couplers and Section 6.3 highlights the results and findings of these models. Two models are then selected for further study in Section 6.4 from this pool of parametric models based on their capability to provide the most even distribution of collision energy along the rake at moderate collapse force. Section 6.4 discusses the effects of number of coaches on the spring crush distributions for the two selected spring characteristics. Section 6.5 attempts to model a train with a mixture of spring characteristics : an impact interface collapsing with hardening characteristics and the intermediate interfaces collapse with constant collapse force characteristics, both of which have similar average collapse force. This was found to be more crashworthy than any of the trains with equal springs with constant force characteristics. Section 6.6 summarises the findings of this Chapter.

6.2 The parametric study of spring characteristics with Oleo couplers

Chapter 5 has concluded that trains with extended softening deflections are inherently incapable of evenly distributing the collision energy along the rake even if the theoretical optimum gap is used. Hence this Chapter selects 8 models from the cfy, rps, rpy and iph series from Chapter 5 and adds a new one to make up a total of 9 models to be categorized into 5 series for the study of spring characteristics with Oleo couplers. These models are basically the same as those of Chapter 5 except that Oleo couplers are now being included, that is the "mass-spring-mass" representations for intermediate interfaces are converted to a "big mass-spring-small mass-spring-big mass" configuration, see Figure 4.10.

The initial velocity of 60km/h (37mph) was chosen since it is very close to the 40mph limiting velocity as discussed before, it is also the impact velocity chosen by BRR for the October 1994 full scale collision test. The impact configuration for that test was a symmetric five coach train (moving) colliding into another five coach train (stationary), and is also chosen for all the 9 models here. The new model (known as iph2.33) has the spring characteristics shown in Figure 6.1.

The models studied are as tabulated in Table 6.1 over the page :

Model's name	Spring's characteristics*	Initial velocity (km/h)	Mean force P_m (MN)**	Other input parameters***
cf1.6	As in cfy1	60	1.60	As in Figure 4.11 except these are 5 to 5 collisions.
cf2.3	As in cfy2		2.30	
cf3.0	As in cfy3		3.00	
rp1.95	As in rps2		1.95	
rp2.30	As in rps3		2.30	
rp2.65	As in rph2		2.65	
ip1.62	As in iph2		1.62	
ip1.64	As in iph3		1.64	
ip2.33	See Figure 6.1		2.33	

* Impact interface have crush zones (vehicle ends) that absorb 1.6MJ before infringing the passenger compartment, i.e. 3.2MJ per interface, and intermediate interfaces could absorb half this energy. All models have their own inter-vehicular distance (gap size as shown in Table 5.1).

** Mean force is the energy require to cause complete collapse of the crush zone divided by the permanent deformation.

*** All models have Oleo couplers breaking away at 1.2MN as shown in Figure 4.11, except that the number of vehicles has increased to form a five to five collision configuration.

Table 6.1 : The nine models studied.

As in Chapter 5, the above models are again categorized into five series to allow parametric comparisons :

(1) The cfy series, which consists of the models cf1.6, cf2.3 and cf3.0. This series examines the parametric effects of constant yield force level as in Figure 5.4.

(2) The rps series, which consists of the models cf1.6, rp1.95 and rp2.30. This is for studying the parametric effects of ramp slope of the collapse force as in Figure 5.5.

(3) The iph series, which consists of the models cf1.6, ip1.62 and ip1.64. This is to investigate the parametric effects of the initial spiky peak force magnitude as in Figure 5.8.

(4) The rpy series, which consists of the models rp1.95 and rp2.65. This series studies the parametric effects of the mean force magnitude for hardening springs with the same ramp slope as in Figure 5.7.

(5) The ipy series, which consists of the models ip1.62 and ip2.33. This series involves a new model with the sping chracteristic as shown in Figure 6.1. This series is for examining the parametric effects of the mean force magnitude for springs with the same level of initial spiky peak force. By using the method described in Section 5.2, the optimum gap for ip2.33 was found to be 0.528m.

It should be emphasised that all springs characteristics for this Chapter still fall within the '3MN to 1.6MN' corridor as stipulated in Figure 5.3. A small damper with 0.5% damping ratio was included in parallel with all the springs in the interfaces.

The results of energy absorbed in the various interfaces are calculated at the time when the whole system settled, i.e. the system internal energy reached a stationary (maximum) value.

6.3 Results and discussions for the three series of models

6.3.1 The constant yield force (cfy) series

Figure 6.2 shows the various interface energy absorbed for the models in the cfy series. Interfaces 1 and 2 reduces its energy absorption as the collapse force increases while interface 3 does the opposite. In other words, the overall energy distribution for all the interfaces approaches the ideal pattern as the yield force increases. This is due to the Oleo couplers, which are designed to breakaway at 1.2MN. As the yield force of the spring increases, the couplers breakaway at an earlier time with a shorter stroke since they reach the breakaway force sooner. This has resulted in less energy being dissipated in the couplers and the disturbing effect of the couplers on the even energy distribution along the colliding rake is minimised. Note that a model with an optimal gap is equivalent to couplers breaking away immediately upon a collision.

To illustrate the above point clearer, a graph of the force against the coupler breakaway time is plotted for an interface of all the models, not just those in the cfy series. Figure 6.3 shows the graph of mean force in interface 1 (F_{1m}) against the time for interface 2 couplers to breakaway (t_{2b}), for all the parametric models. F_{1m} is the average force in interface 1 prior to t_{2b} and is computed by integrating the force-time history of interface 1 up to the time t_{2b}. to obtain the impulse I_1 for all the models, and then divides I_1 by t_{2b}. Table 6.2 shows the results of t_{2b}, I_1, F_{1m} and P_m for the models :

Model	t_{2b} (sec)	I_1 (MN.s)	F_{1m} (MN)	P_m (MN)
cf1.6	0.106	0.169	1.59	1.60
cf2.3	0.057	0.129	2.26	2.30
cf3.0	0.037	0.107	2.89	3.00
rp1.95	0.083	0.152	1.83	1.95
rp2.30	0.063	0.126	2.00	2.30
rp2.65	0.049	0.119	2.43	2.65
ip1.62	0.105	0.170	1.62	1.62
ip1.64	0.103	0.169	1.64	1.64
ip2.33	0.057	0.130	2.30	2.33

Table 6.2 : The results of t_{2b}, I_1, F_{1m} and P_m for all the parametric models. F_{1m} is obtained by dividing I_1 to t_{2b}.

Table 6.2 shows that P_m is always slightly higher than F_{1m} for those models with constant collapse and initial spiky peak force springs, and considerably higher for the ramp collapse force models. The is because the average force in a hardening spring depends on the collapse distance and P_m was computed on the basis of full collapse of

crush zones (i.e. absorbed 3.2MJ per interface) but the ramp collapse force models only achieved partial collapse of interface 1 crush zones.

Figure 6.3 shows that lower F_{1m} (or P_m since Table 6.2 has suggested that they are proportional to each other) delays the breaking away of the couplers which allows them to travel longer with more energy absorption. This upset the evenness of energy distribution in the colliding rakes.

The model cf1.6 has just managed to fully crushed its crush zone in interface 1 absorbing 3.2MJ even though the impact speed has not reached 40mph. Recall from Chapter 4 that the model Cp2 has shown the ability to absorb 3.2MJ for a 40mph (17.88m/s) uni-directional collision. There are only two modifications made to the model Cp2 for the creation of cf1.6 : the spring collapse load has been reduced from 2MN to 1.6MN and the number of coaches has increased from 3 to 5. It will be shown later that the change of 3 coaches to 5 coaches per rake has negligible effect on interface 1 crush performance, so the extra energy absorbed in interface 1 of cf1.6 is mainly due to the spring collapse load being closer to the couplers' breakaway force allowing the couplers to exercise more influence over the energy distribution of the system.

6.3.2 The ramp slope (rps) series

Figure 6.4 shows the results of the plastic collapse stiffness (ramp slope of the springs) against the various interface energy absorbed for the models in the rps series. It is clear that by increasing the hardening slope of the springs, more even energy distribution could be achieved relieving interface 1 from 'over-energized'. Models in the rps series has the same yield force (at 1.6MN) but different plastic collapse slopes. Hence increasing the plastic collapse slope would increase the mean collapse force which has the effect of breaking the couplers earlier and thus facilitating a more even distribution of energy along the colliding rakes.

Figure 6.5 shows the graph of the mean force (P_m) against the various interface energy absorbed for models in the rps and cfy series. To increase the P_m of the model cf1.6, one can either increase the plastic collapse slope or rise the constant yield force. Figure 6.5 has, however, shown that by increasing the plastic collapse slope to reach the specified P_m, a more even energy distribution along the colliding rakes is achieved than rising the constant yield force.

6.3.3 The initial peak force (iph) series

Figure 6.6 shows the results of the initial peak force magnitude against the various interface energy absorbed for the models in the iph series. It is clear that for the range of initial peak force considered, altering the initial spiky peak force level has practically no effect on the energy distribution along the colliding trains. The previous Chapter has also shown that the level of the initial spiky peak force does not significantly alter the energy distribution pattern for optimally gapped coupler-less models. This is

because the initial peak disturbance rapidly softens which allows the springs to quickly settle at the constant collapse phase for most of the energy absorption process.

6.3.4 The effect of rising the collapse force to a specified value for different spring characteristics on energy distribution.

If the springs cf1.6, rp1.95 and ip1.62 have each increased the yield force by 0.7MN, the springs cf2.3, rp2.65 and ip2.33 would be obtained respectively. Recalling that cf1.6 and cf2.3 are in cfy series, rp1.95 and rp2.65 are in rpy series and ip1.62 and ip2.33 are in ipy series.

In this section, the effect of rising the yield force (thus rising P_m) of these springs with different characteristics by 0.7MN on energy distribution will be discussed. The rpy series (cf1.6 and cf2.3) is used as the baseline yardstick. It is better to compare the energy distribution for these models by normalising the various interface energy absorbed with their respective ideal value. For the current Chapter the ideal energy absorption in interface 1 is 2.430MJ and 1.215MJ for the other interfaces.

Figure 6.7 shows the interface normalised energy distribution results for the models in the cfy and ipy series. Both series have shown similar behaviour as P_m is increased, confirming again that the initial spiky peak force in a spring would not effect the energy distribution.

Figure 6.8 shows the corresponding results for models in the cfy and rpy series. The introduction of hardening springs in the rpy series (both models in rpy series have the same hardening slope of 0.42MN/m) has moved all the interfaces' results closer to the ideal line than those in the cfy series at any P_m within the range shown in Figure 6.8.

All models simulated so far have confirmed that crush zones in the intermediate interfaces could be made to absorb half the energy than that required to be absorbed in the impact interface. This statement could now be applied to hardened collapsing crush zones and crush zones which collapse with a spiky initial peak force.

6.3.5 Maximum crush distance at interface 1

Figure 6.9 shows the bar chart comparing the maximum crush distance in interface 1 for the various models discussed so far. The results are presented in the order of shortest to longest crush in interface 1. The models cf1.6, ip1.62 and ip1.64 have all achieved a crush distance of 2m (1m per vehicle end), the other models have all shown to crush well below 2m for interface 1. All models have also absorbed more than 1MJ in interface 1 and so all models have met the BR's specification of 'absorbing at least 1MJ within 1m'. Note that two out of the three best models for achieving minimum crush in interface 1 have hardening springs.

6.4 'Number of coaches' as a parametric variable

6.4.1 Introduction

There is another input parameter which need to be studied : the number of coaches (N). Would an increase of N overload the impact interface during collisions?

The works reported here are solely concerned with symmetric impact situations, where the number of coaches in both rakes is the same. Chatterjee and Carney [1] have investigated some cases where rakes with different numbers of coaches collide, and have arrived at the conclusion that the impact interface suffers essentially equal damage for these cases, but the following coaches in the smaller rake experience less plastic deformation than their counterparts in the larger rake. It must be stressed that their models did not involve any couplers or damping, only with gaps.

Two spring characteristics are chosen here for comparing their sensitivity to N on energy distribution : cf2.3 and rp2.30. The range of N to be studied is $7 \geq N \geq 2$.

6.4.2 The parametric models

Table 6.4 tabulates the parametric models for the current study :

Model	Number of coaches, N	Other input parameters	Model	Number of coaches, N	Other input parameters
cfn2	2	As in cf2.3	rpn2	2	As in rp2.30
cfn3	3		rpn3	3	
cfn4	4		rpn4	4	
cfn5	5		rpn5	5	
cfn6	6		rpn6	6	
cfn7	7		rpn7	7	

Table 6.4 : The parametric models for studying the effects of number of coaches (N) on energy distribution along colliding rakes.

6.4.3 Results and discussions

The cfn series : Figure 6.10

Figure 6.10 shows the graph of number of coaches (N) against maximum interface crush distance (x_{max}) for various interfaces of the models in the cfn series. The interface crush behaviour in Figure 6.10 could broadly be classified into three regions : The impact interface (interface 1), intermediate interfaces and the free end interface (the last interface of each rake).

Interface 1 : Figure 6.10

For this interface, N Vs x_{max} could be fitted with the curve (shown as 'b' in Figure 6.10) which has an asymptote at x_{max}=1.39m. If the data point with N=2 was ignored, the rest of the data points in interface 1 are well fitted by the line x_{max}=1.37 (shown as 'a' in Figure 6.10). This is very close to the asymptote x_{max}=1.39m of previous curve fit. Based on these two curve fitting results, there is good evidence to suggest that the number of coaches (N) within a rake with constant collapse springs, has no significant effect on interface 1 crush performance for $N \geq 3$.

Intermediate interfaces : Figure 6.10

The intermediate interfaces (excluding the last interfaces) crush results in Figure 6.10 has more data points as N increases and these could be bounded by two fitted curves : one is shown as 'd' in Figure 6.10 and the other as 'c' in Figure 6.10. The former is a curve fit for the second last interface crush results and has an asymptote at x_{max}=0.37m while the latter is a curve fit for the second interface and has an asymptote at x_{max}=0.60m. These imply that as N increases, the crush distances for the intermediate interfaces redistribute among themselves within the two bounded asymptotes of x_{max}=0.37m and 0.60m.

The last interface : Figure 6.10

The free end interface crush results, as expected, are the smallest in the respective models, since they only deliver but not receive external impulses. In Figure 6.10 these free end interfaces crush results could be fitted by the curve (shown as 'e' in figure 6.10) which has an asymptote at x_{max}=0.21m. It can seen that as N reaches a value of 5, x_{max} practically has settled at the asymptotic value which remain quite unaffected by any further increment of N.

Summary : Figure 6.10

To summarise, all crush results in the cfn series have seen to be bounded by the two asymptotic lines of x_{max}=0.21m and x_{max}=1.39m, with the intermediate interfaces crush results sub-bounded by the two asymptotes x_{max}=0.37m and 0.60m.

The rpn series : Figure 6.11

Figure 6.11 shows the graph of number of coaches (N) against maximum interface crush distance (x_{max}) for various interfaces of the models in the rpn series. This graph has shown a different crush patterns than those in the cfn series. Both interfaces 1 and 2 are unaffected by the variations of N, even with N=2, which is unlike the cfn series. This is an indication that the hardening springs have created effective obstacles for further interfaces to influence the overall energy distributions through external impulses. Interface 1 crush results are well fitted with the line x_{max}=1.24m (shown as

'a' in Figure 6.11) and interface 2 with the line x_{max}=0.69m (shown as 'b' in Figure 6.11). The three categories of interface crush behaviour are still clearly visible in Figure 6.11.

Interface 1 : Figure 6.11

Interface 1 crush results were seen earlier to be very well fitted by the line x_{max}=1.24m which is 11% shorter than x_{max}=1.39m for interface 1 crush results in the cfn series. Note that the models in rpn series have a F_{1m} of 2.01MN and those in cfy series have a F_{1m} of 2.26MN. So the effective force acting within the models in the rpn series is slightly lower than those in the cfy series during the simulations.

Intermediate interfaces : Figure 6.11

The intermediate interfaces crush results are bound by the curve shown as 'c' in Figure 6.11 and the line x_{max}=0.69m. The former is a curve fit for the second last interface crush results which has an asymptote at x_{max}=0.51m, and the latter is the curve fit line for the second interface. The crush distances in the intermediate interfaces redistribute among themselves within the two bounded asymptotes of x_{max}=0.51m and 0.69m, which is smaller than the corresponding x_{max}=0.37m and 0.60m asymptotic boundary in the cfn series.

The last interface : Figure 6.11

The free end interface crush results could be fitted by the curve (shown as 'd' in Figure 6.11) which has an asymptote at x_{max}=0.25m. This is 20% higher than the corresponding asymptotic value of x_{max}=0.21m in the cfn series.

Summary : Figure 6.10 & 6.11

Table 6.5 tabulates the values of the asymptotic lines of Figures 6.10 and 6.11 :

Interface	Asymptotes in the cfn series (m)	Asymptotes in the rpn series (m)
Impact interface	1.39	1.24
Second interface	0.60	0.69
Second last interface	0.37	0.51
Last interface	0.21	0.25

Table 6.5 : Comparing the various interface asymptotic crush distances for both cfn and rpn series.

Table 6.5 has suggested that the interface crush distances in the rpn series are more evenly distributed than in the cfn series. Since the springs in both series have a

common mean collapse force of 2.30MN, it confirms that the hardening springs are capable of providing a more even energy distribution than the constant collapse force springs as N increases.

6.5 A train with a hardening spring in its impact interface and constant collapse force springs for its intermediate interfaces

6.5.1 Introduction

The previous analyses have shown that crush zones with hardening characteristics to be better than constant force collapse characteristics in terms of sharing collision energy along the rake. However, it is common for modern trains to have projecting noses at the train ends for aerodynamic streamlining purpose, see for example the Eurostar as shown in Figure 6.12. The projecting noses at the ends will collapse with a hardening characteristic and the rest of the intermediate interfaces has normal crush zones which collapse at a constant force, i.e. a 'rp' spring in the impact interface and 'cf' springs for other intermediate interfaces. How this mixed arrangement behave in term of energy distribution, is the core issue to be discussed next. Numerical experiments would be conducted to investigate the energy distribution performance of such trains with mixed springs.

All the models considered in this section have a six-to-six symmetric impact configuration with initial velocity 16.67m/s. The impact interface (interface 1) has a ramp collapse force characteristic which yield at 2MN and collapses with a hardening slope of 0.51MN/m. This is shown in Figure 6.13. The intermediate interfaces have the same collapse characteristic as the cf2.3 spring, except that the crush zone has extended length just to ensure that the passenger compartments will not be infringed. All the interfaces could absorbed 3.2MJ. One objective of studying such a mixed-springs' arrangement is to check whether the intermediate interfaces still collapse with no more than half the energy absorbed by the impact interface. The results of previous model cfn6 is taken as the baseline comparison for two new mixed-springs' models : one with the same gap size of 0.53m (optimal gap size for cf2.3 springs) throughout the train; the other has a gap of 0.50m for interface 2 with the rest of the intermediate interfaces still having a gap of 0.53. The later has a tuned gap for the new hardening spring. Note that this new spring (in Figure 6.13) has an identical mean collapse force of 2.3MN as in the cf2.3 spring. Hence both springs will collapse at compatible force levels with minimal perturbations. The following table summarises the mixed-springs models studied here :

Model	Spring characteristics for interface 1	The other input parameters
mixn6	Figure 6.13 without tuned gap	As in the model cfn6 with extended crush zones.
mixn6g	Figure 6.13 with tuned gap	

Table 6.6 : Summary of input data for all mixed-springs models. All interfaces have crush zones capable of dissipating 3.2MJ.

6.5.2 Results and discussions

The results for the mixed-springs' models are shown in Table 6.7 :

	Model cfn6 (Baseline)	Model mixn6	Model mixn6g
x_1 (m)	1.37	1.26 (-8.03%)	1.22 (-10.94%)
x_2 (m)	0.57	0.56 (-1.75%)	0.58 (+1.75%)
x_3 (m)	0.53	0.55 (+3.77%)	0.55 (+3.77%)
x_4 (m)	0.50	0.51 (+2.00%)	0.52 (+4.00%)
x_5 (m)	0.41	0.44 (+7.32%)	0.43 (+4.88%)
x_6 (m)	0.23	0.24 (+4.35%)	0.24 (+4.35%)
mx_1	1.30	1.18	1.14
mx_2	1.09	1.06	1.09
mx_3	1.01	1.03	1.04
mx_4	0.94	0.97	0.97
mx_5	0.78	0.82	0.82
mx_6	0.44	0.46	0.46

Table 6.7 : The results of the mixed-springs models with cfn6 as baseline comparison. (Bracketed figures are % difference with respect to the corresponding results in cfn6)

In Table 6.7, x_n represents maximum crush in interface n and mx_n represents normalised maximum crush for interface n, normalisation made dividing the actual crush by its ideal value. Since a mixture of springs were involved, normalisation of results was necessary to enable comparison between the models. The best model should have all mx_n as close to unity as possible.

Figure 6.14 shows the graph of mx_n against interface number for the three models. Both models mixn6 and mixn6g have moved all the interface normalised crush results closer to the ideal case as compare to the model cfn6. The most obvious improvement (closer to the ideal case) is seen in interface 1. This improvement is due to the better resistance to external influence offered by the hardening springs which is equivalent to providing a more isolated environment for the energy to be dissipated in interface 1. The rest of the interfaces have only achieved marginal improvements by both mixed-springs' models.

The tuning of gap made in mixn6g has slightly relieved interface 1 from being over-loaded, this is clearly seen from Table 6.7 : mx_1 for mixn6 is 1.18, and for mixn6g is 1.14, less than 4% improvement is achieved by tuning the gap in interface 2. Little effect is seen here by the tuned-gap model since the specially tuned gap of 0.50m for interface 2 is less than 6% to the 0.53m gap used throughout all interfaces in mixn6.

All the intermediate interfaces, in both mixed-springs' models, have dissipated less than half the energy absorbed in interface 1.

The two mixed-springs' models studied here have shown that a train with mixed-springs are capable of providing a slightly more even distribution of energy than a train with identical constant collapse force springs; provided the collapse forces within the colliding rakes are similar. The improvement is most profound in the impact interface.

6.6 Conclusions

The following conclusions can be drawn from the study outlined in this Chapter :

(1) Oleo couplers exert strong influence over the energy distribution along the rake if they are allowed to absorb sufficiently large amount of energy during the collision.

(2) Crush zones with low mean collapse force (P_m) delay the breaking away of the couplers allowing them to travel longer and absorb more energy.

(3) Higher P_m provides more even energy distribution along the rake. Crush zone collapse force must be higher than the coupler break-away force (F_B).

(4) The bigger the force differential differential (P_m-F_B), the more even energy distribution will be achieved by the colliding rakes.

(5) For a common mean collapse force (P_m), crush zones with hardening characteristics are found to give a better energy distributions along the colliding rakes than constant force characteristics. This is because the slopes of the ramp force in the crush zones have formed obstacles for the Oleo couplers to pass impulses to neighbouring interfaces.

(6) For the range of initial peak force considered in this Chapter, altering the initial spiky peak force level have practically no effects on the energy distribution along the colliding trains.

(7) The number of vehicles (N) in a rake has very little effect on the energy distribution especially if $N \geq 3$. This is applicable to crush zones that collapse with hardening or constant force characteristics.

(8) Modern trains with projecting noses at the ends can be modelled with mixed springs. Provided these springs have similar mean collapse force (P_m), these trains behave in a similar manner as those with constant collapse force springs. A slightly more even energy distribution is achieved along the colliding rakes due to the use of a hardening spring in the impact interface.

(9) All models have confirmed that crush zones in the intermediate interfaces could be made to absorb half the energy (not half the crush distance) than that required to be absorbed in the impact interface. This statement could now be applied to hardened collapsing crush zones and crush zones which collapse with a spiky initial peak force.

Reference

[1] Chatterjee, S. & Carney, J. F., "Crash Energy Management and Interior Crashworthiness in Passenger Trains.", Internal Report, Vanderbilt Engineering Centre for Transportation Operations and Research, Vanderbilt University, Nashville, Tennessee, December 1994.

Chapter 7

Assessment of occupant kinematics, Part I : Parametric study and tuning of a forward facing PAMCRASH's dummy model.

7.1 Introduction

The Public Inquiry into the rail accident at Clapham Junction on the 12 December 1988, recommended that the British Railways Board (BRB) should carry out a review of vehicle interiors, structural crashworthiness study and other passenger safety features.

In respond to that recommendation, programmes of interior crashworthiness study, which included mathematical modelling and full scale sled testing for studying the occupant kinematics during a collision have been initiated. Various current vehicle interior designs and different dummy configurations have been used in this research. Some of this work was carried out by the Motor Industry Research Association (MIRA) and Vehicle Safety Consultants Ltd (V.S.C.) under contracts placed by BRB. The overall objective of these studies is to find out what changes can be made to vehicle interior design to reduce the injurious effects of secondary impacts between passengers and interior fittings (seats, tables, partitions etc.) and other passengers, during a collision.

In 1991, BR Research (BRR) initiated a programme of work with MIRA to study occupant kinematics in a Class 423 Mk I type coach when subjected to a collision retardation pulse and to assess the injury potential due to secondary impacts with interior fixtures. The programme included both HyGe sled tests [1] and MADYMO computing simulations [2]. Then a year later, BRR replicated the same work by using the non-linear finite element code DYNA3D [3], validating its accuracy by comparing with actual HyGe sled test results. It was found that DYNA3D has predicted the results at the same level of confidence as those obtained by MADYMO. However, both software packages have produced results which differ from those occurred in 'real' accidents, especially those results pertaining to the leg which the codes appear to have predicted more severe injuries than occur in practice.

Another non-linear finite element code, PAMCRASH, has been used by the Advanced Railway Research Centre (ARRC) at the University of Sheffield. In order to validate the PAMCRASH dummy model, the same MIRA HyGe sled test results were used for the present work as benchmark comparison. The present Chapter describes this work.

The current work selected one of the dummy models studied previously by MIRA [1,2] and BRR [3]. The chosen model consists of a forward facing Hybrid III 50th% male dummy seated in a Class 423 seating bay and subjected to a specified deceleration pulse. This interior seating arrangement is chosen for study here since it is one of the commonest that would inflict high casualty rate in secondary collisions due to the long flail distance and interactions between occupants. The term 'forward facing' implied that the dummy is facing the direction of travel.

The current work parametrically investigated the effects on dummy trajectories caused by some of the input variables such as the contact friction, the cushion contact stiffness etc. The experience gained in these parametric studies for the forward facing occupant model will allow future similar models to be created with confidence. A point to note is that the current work has made an improvement to all previously reported computational works by MIRA and BRR, in that they had applied the deceleration pulses directly to the dummy while restraining the seats and other fittings not to move or rotate at all. However, the current work applied the deceleration pulses to the seats and floor while observing how these pulses were being transmitted to the dummies. The latter is obviously a better representation of the actual HyGe sled tests.

The main objective for this chapter is to study the PAMCRASH Hybrid III dummy model behaviour parametrically using a sled test result as a yardstick so as to gain an insight of the limitations and capabilities of such a numerical computation model. Section 7.2 highlights the limitations of the dummy model and warns that such FE representation of the dummy although able to predict results similar to those obtained from sled tests, it is not a true representation of an human being; the results thus require careful interpretation. Section 7.3 states some injury criteria used in the railway environment, these are similar but not the same to those used in the automotive industry. Section 7.4 explains in more detail how the FE dummy models are constructed and discusses the parametric variables being studied. Section 7.5 presents the results with analyses and discussions. Section 7.6 summarises the findings of the chapter.

7.2 Some general points about the dummy model

7.2.1 General background

The automobile industry has during the past decades, developed instrumented dummies for use in the standard tests which are conducted to show conformance of the vehicle with increasingly severe legal requirements. The most current versions of these dummies are the Hybrid III family, which have instrumentation catering for head-on collisions. The Hybrid III dummy has 44 standard data channels, recording measurements of accelerations on the skull, upper torso and pelvis, deflections of the chest and knees, and of contact forces in the neck, spine region, arms, thighs, knees

and lower legs. For side-impacts, further dummies have been developed such as the EUROSID series but these are not likely to be of use in the railway environment. Initial development concentrated on a dummy representing a 50th percentile male. Other sizes are now being used as well. If a man is 90th percentile in height, it means that 10% of other men are taller and the remaining 90% shorter. The injury criteria normally correlate to measurements obtained from the 50th percentile male dummy. European legislation currently requires testing to be done only on the 50th percentile male dummy. In North America, further dummies representing small (5th percentile female) and large (95th percentile) persons have also been developed and used extensively in the transport industry.

7.2.2 Limitations of the Hybrid III dummy

The overall dimensions and mass distribution of the dummy are reasonable, which is very encouraging when they are used to simulate articulated rigid bodies and to study the dynamics in deriving the human trajectory path during secondary impact. But once contacts are made by the dummy with other bodies, a number of shortcomings surface due to the non bio-fidelic behaviour of the dummy [4] :

(1) There is no potential for assessing facial injury such as breaking of the nose;

(2) The neck motion is not human-like and does not effectively represent the inclination of head during impacts;

(3) The stiffness of the abdomen is realistic for seatbelts but not for hard table edges;

(4) The rib cage ends too high up the trunk;

(5) The spine is not represented realistically. However, a recent advanced dummy model has a complete representation of the spinal column and vertebrae [5]. It has been used to aid aircraft interior crashworthiness design and also shown considerable potential for automotive safety and biomechanics study;

(6) The lower legs don't break. This could affect the trajectory subsequent to a leg-breaking interaction.

Despite the above shortcomings, the Hybrid III dummy is still a useful tool for assessing the injury potential for occupant secondary collisions. However, care has to be exercised during interpretations of the results obtained from the dummy tests or computer simulations and any conclusion drawn must eventually correlate to the real accident situation.

7.2.3 The meshed computing models for dummies

Almost 32 years have passed since the first mathematical models to describe the dynamic response of a vehicle passenger involved in an accidental collision event was proposed in 1963 [6]. Since then, research studying the behaviour of occupants during secondary collisions within a vehicle interior has become increasingly sophisticated. A historical review of the mathematical simulation methods in this field was conducted by Prasad & Chou [6]. Now, highly sophisticated finite element meshed models of the Hybrid III dummies are available in a number of programs, notably MADYMO, DYNA3D and PAMCRASH. These are reproductions of the dummies, not of the humans on which the dummies are based. As such these meshed models inherited the dummy shortcomings as well. The various parts of the dummy bodies are normally simulated by rigid bodies, inter-linked by joints with the appropriate stiffness and damping characteristics.

These finite element meshed models are very useful in assessing the injury potential of occupant during secondary collisions and offer an inexpensive means of investigating parametric changes. Good correlations have been demonstrated between dummy test results and predictions by computing meshed models.

7.3 Accident injury criteria

The instrumented Hybrid III dummies have been designed to provide fairly realistic simulations in impact testing. During the tests, parameters corresponding to the injury mechanism for various body segments were recorded and compared with established criteria. These criteria were reported in Chapter 2, and are related to measurements taken from a 50th percentile male dummy.

The current study can be used to assess the potential of injury to which the forward facing passenger in a Class 423 coach is subjected. To be consistent with the previous studies in References [2] and [3], the following three injury criteria are used :

(1) Head injury : Head injuries are assessed in two ways. The first assessment is the *HIC*, which is an non-dimensional integral function of the head deceleration and its duration and the threshold value is set at 1000. The second assessment criterion is that the maximum peak acceleration sustained over a period of 3ms should not exceed 80g.

(2) Neck injury : Acceptable threshold limits are set on the basis that head/neck bending moments should not exceed 190Nm in flexion and 57Nm in extension.

(3) Leg injury : A maximum leg contact load of 3.8kN is set as a criteria. This value was first adopted during early 1970s in the automotive industry [4]. More research work is ongoing now at BRR for determining a better injury criteria for lower legs.

7.4 Description of the current modelling work

7.4.1 General description of the models

A forward facing occupant seating on a Class 423 seating bay was modelled. Figure 7.1 (with labels) shows the PAMCRASH dummy model, note that the deceleration pulse is applied in x-direction of Figure 7.1. Only the seats and part of the floor are modelled, the rest of the interior features such as ceiling and side wall/windows are of no interest since only a longitudinal deceleration pulse is applied to the whole coach and thus secondary collisions to the sides and top are not expected.

7.4.2 Contact surfaces

Interaction of the dummies with their surroundings is achieved by the definition of "contact surfaces"; and the contact characteristics between any two contacted parts are defined by a load curve which describe the load against penetration of the contact surface. In the current work, all models have the following contact-surfaces :

(1) head to headrest/seatback;

(2) upper torso to seatback;

(3) spine to seatback;

(4) lower torso to seat cushion;

(5) upper legs (femur) to seat base cushion;

(6) lower legs (tibia) to seat front edge cushion;

(7) foots/heels to floor;

The contact surface stiffnesses for the individual seat components such as the seatbase cushion, seatback, headrest etc., have been obtained experimentally by MIRA and BRR, so their results were directly used for the present models, and are shown in Figure 7.2.

7.4.3 The deceleration pulse and boundary conditions

A longitudinal (x-direction in Figure 7.1) deceleration pulse as shown in Figure 7.3 is applied to both the seats and floor. This is the C3 pulse used by MIRA, which is, as noted in Figure 2.40 (Chapter 2), different from the C3 pulse specified by BR. Note that the seats and floor are constrained to translate only in the longitudinal direction. This is a condition equivalent to non-overriding/derailment collisions. For the previous work done by MIRA with their MADYMO models and BRR with their DYNA3D dummy models, the C3 pulse was directly applied to their dummies and the seats and floor were constrained not to move or rotate at all. This is equivalent to a 100% transmission of the C3 pulse from the coach body to the occupant, which is not a realistic way to model the sled test but may be considered as an 'upper bound' safety condition imposed by MIRA and BRR since the actual pulse would be filtered (and reduced) by the seat joints and cushion stiffnesses before it reaches the occupant. However, imposing motion to the dummies would artificially influence their trajectories. The current modelling technique not only rectifies this shortcoming but also investigates some of the input variables to the occupant model and studies the effects of these input variables on the occupant's head trajectories parametrically.

An important point to note for the dummy models studied here, is that velocity boundary conditions were used to define the C3 pulse instead of acceleration. This is due to a technical shortcoming in the PAMCRASH 1993 version, which did not allow the use of acceleration boundary condition to be defined for the dummy models.

7.4.4 Gravity load

Ideally, the whole dummy is to be loaded with gravitational force from the start till the end of the model run time, i.e. applied as a step input at zero run time, but as a common FE practice for any explicit codes, load curves are never applied as step input. As such gravity rise time (time for the gravity load curve to linearly rise from $0 m/s^2$ to $9.81 m/s^2$) is chosen as an input parameter to be studied here. This is explained later.

7.4.5 The parametric study

The input variables chosen for the parametric study were :

(1) The cushion stiffness of the seat base;

(2) The contact friction;

(3) The rise time for the gravity load curve.

A baseline model was chosen with all the input variables fixed and then 2 parametric models were created for each of the above variables. After analysing the results of these parametric studies and comparing them with the sled test results, a set of 'optimal input parameters' would be derived for the best representation of the sled test.

It was also shown in the previous work by Swindle [3] that the contact stiffness between the dummy body parts and those of the cushions, headrest and seatback can have some influence on the head deceleration responses of the dummies. However, he did not report the effects on dummy trajectories when these contact stiffnesses vary. The current study has chosen the collective seat cushion stiffnesses (shown in Figure 7.2) as a parameter to study the effect they have on the trajectory of the occupant head. The load curves shown in Figure 7.2 are considered as the baseline case. A ±10% change of the baseline stiffnesses means that all the load curves in Figure 7.2 are changed ±10% for the same deflection. The cushion stiffness affects the seating comfort of a passenger and so it cannot be vary without proper restraint, a ±10% variations is thought to be justifiable for the purpose of parametric study.

The contact friction coefficients used by the previous workers [2,3] were 0.66 for the foot to floor contact and 0.45 for all other surfaces. The current study applied the same foot to floor contact friction but for the rest of contact surfaces 3 contact friction coefficients were used as input variable : 0.35, 0.45 (the baseline case) and 0.55.

Gravity is applied to all the nodes in a model according to a user specified load curve. Hence, it is obvious that the load curve would be a step input load curve which 'switches on' once the analysis starts. However, step input involves an initial infinite slope and that ESI has recommended that a ramp input be chosen instead but with a very 'quick' rise time, i.e. from 0g to 1g acceleration in as short a time as possible. The quicker the rise the better representation of the actual case but where should the line be drawn? The gravity load curve rise time is thus chosen as a parameter for study. 3 rise time values were chosen : 2msec (the baseline model, 0.5% of the total model run time), 4msec (1% of the total model run time) and 8msec (2% of the total model run time). Figure 7.4 shows all the parametric gravity load curves studied here.

There are altogether seven parametric models to be studied and these are tabulated in Table 7.1 :

Model	Seats' cushion stiffness (N/mm)	Dynamic contact coefficient of friction	Gravity load curve rise time (msec)
1 (Baseline)	**In Figure 7.2**	**0.45**	**2**
cush-1	**-10%**	0.45	2
cush-2	**+10%**	0.45	2
frict-1	In Figure 7.2	**0.35**	2
frict-2	In Figure 7.2	**0.55**	2
grav-1	In Figure 7.2	0.45	**4**
grav-2	In Figure 7.2	0.45	**8**

Table 7.1 : The input variables for the parametric models

During earlier modelling exercises, the seats and floor mass were also chosen to be a parameter but were found to have no effect to the models even if the masses were increased by 2 orders of magnitude. This is directly due to the application of a velocity boundary load curve to the seats and floor since external energy would then required to be supplied to the model and such application of external energy would be 'adjusted' as the masses of the seats and floor change in order to conform with the defined velocity load curve. As a results no effects would be 'felt' by the dummies in the models if the masses of these fixtures were varied. It was also found during the preliminary trail modelling practices that the results are virtually insensitive to the changes of initial velocities within the range of 9 to 8m/s. The C3 pulse would take this initial velocity range to a final velocity range that is close to zero, which is mandatory.

7.5 Results and discussions

7.5.1 Effects of cushions' stiffnesses on the dummy's kinematics

Figure 7.5 shows the animation sequence for the baseline model together with those obtained by BRR's DYNA3D model. We do not expect the two models to have exactly the same response (the two models are not entirely the same and the means of application of deceleration pulse for them were different) but generally the animation sequence of the two models have exhibited similarities between them as shown in Figure 7.5. Note that the PAMCRASH dummy studied here is more agile (more freedom in moving its limbs and other body parts) whereas the DYNA3D dummy is seen to be more 'rigid' during the simulation. This is thought to be the consequence of

applying the deceleration pulse directly on the dummy thereby 'governing' how it should be moved.

Figure 7.6 shows the plot of z-x trajectories for the three models studying the cushion stiffness. This are plots showing the flight paths of the centre of gravity (c.o.g.) of the dummy head in various models and note that only spatial and no temporal information is offered in this plot. No significant difference could be seen for all the models during the first metre travelled in x-direction although there is a clear trend showing that by increasing the cushion stiffness 10% the trajectory during the first metre longitudinal travel would be slightly lifted. After about 1m longitudinal travel of the dummy head, the legs engaged the opposite seat-edge and the whole dummy rotates about the leg/seat-edge contact point advancing the head towards the opposite seat-back at an angle of approximately 45°. Thereafter the dummy head penetrated the opposite seat-back cushion to some depth and then rebounded back via the same angle as it had penetrated. Once the rebound is completed, the dummy head settled downwards and also backwards in a rotary motion as the other part of the body is being lifted off from the opposite seat. The baseline dummy model is seen to behave in a similar way to the one in cush-2, the latter has its dummy head engaging the opposite seat-back at a slightly higher location which was follow by a more violent rebound. The model with the softest cushion, cush-1, also has a similar head trajectory with the other two models until the head rebound occurs. The soft seat cushion has encouraged the head to move upwards after rebound and hit the head-rest of the opposite seat again before settling downwards.

Figure 7.7 shows the dummy head deceleration-time history for the three models and also results from the sled test. Three period of distinct response pattern could be chronicled for all the results shown in Figure 7.7 :

(1) Slight decelerations were experienced by all the dummy heads when the legs engaged the opposite seat-edge from about 160msec to 220msec. For the FE parametric models, increasing the cushion stiffness is seen to slightly reduce the head deceleration during this period of response. All of them however have fairly well followed the actual sled test results in this period.

(2) The duration from 220msec to about 300msec is when the head/seat-back made contact and produce the major deceleration for the dummy head. Here the cushion stiffness has the most influence over the head deceleration response. The sled test results showed two initial peaks of 700m/s^2 at about 240msec and 900m/s^2 at 250msec, which quickly subsided to 300m/s^2 at about 260msec and thereafter settled in a low-magnitude oscillatory deceleration through to 300msec. The FE models have shown that increasing the cushion stiffness will produce a head deceleration to one that is closer to the sled test and also will reproduce the steep descent in deceleration for the period between 250msec to 300msec.

(3) After the main deceleration cause by the head/seat-back impact, the dummy heads have entered the post impact period (the rebound and downward swinging movement as seen previously in Figure 7.6) which all the FE models have over-predicted the actual sled test results. The baseline model and cush-2 (stiffest cushion) showed settling sign for the dummy heads' deceleration during this period since their results have not shown any tendency to rise, only oscillate. The model cush-1 (softest cushion) however, from the previous discussion, has shown to engage in a further head to head-rest impact and hence sustained a more injurious deceleration for the head during this post impact period. As a result, a long duration (from 320msec-400msec) moderately high deceleration (average about 350m/s^2) was sustained by the dummy's head of cush-1 during this period which aggravated the potential of the head injury.

Figure 7.8 shows the graphs of head/neck bending moment against time for the three FE models with the sled test results. All FE model fail to predict the peak moment of about 35Nm which occurred at 200msec during the sled test. The model cush-1 has achieved an exceedingly high peak of 210Nm at 270msec which over-predicted the injury potential. The best FE model to follow the sled test results is cush-2, here the model is seen to have fairly accurately followed the sled test response from 250msec to 400msec.

Figure 7.9 shows the graphs of lower leg contact force for the models. The baseline model has produced two peak contact forces from 140msec to 180msec, both of which are about 3.5kN with the first peak much sharper than the second. The model cush-1 has achieved a single peak of about 5kN for the same period. The model cush-2, however, has achieved an initial peak contact force of 5.5kN which sustained for a very short duration (less than 10msec) and then quickly settled at 1.5kN for the main part of the leg contact response. Although the model cush-2 has achieved the highest peak of 5.5kN, this contact force was only sustained for a very short time, which is thought to be better than the results produced by the other models with lower force and much longer duration.

The baseline model has shown to be a good one for reproducing the sled test results and is thus a good model for future prediction of forward facing dummy model. The model that has consistently produced the best correlated results to the sled test is cush-2, the model with 10% cushion stiffness enhancement. Base on this finding, the cushion stiffness load curve shown in Figure 7.2 would be enhanced for future 'forwards facing dummy sitting in a 423 open-bay environment' simulations in this thesis.

7.5.2 Effects of contact friction on the dummy's kinematics

Figure 7.10 shows the plot of z-x trajectories for the models studying the cushion stiffness. There is a strong indication that larger contact friction produces a lower flight path of the dummy head prior to the head/seat-back contact. This also has dictated the

models with a smaller contact friction to reach the opposite seat-back at a slightly longer time with a smaller angle of approach in the x-z plane. The baseline model and frict-1 (lowest friction model) have shown the familiar downward & backward swinging motion after the head rebound from the seat-back, the model frict-2 has, however, swung upwards after the rebound.

Figure 7.11 shows the deceleration-time history of the dummy head for the models and sled test. The three phases of response are again seen here for all the models with the highest friction model (frict-2) showing the best correlation with the sled test, especially in the post impact period since it showed the unmistakable sign of subsiding towards the end of the head deceleration-time history which is found in the sled test. The worst correlating model is the lowest friction model (frict-1) which has produced a very severe deceleration pulse between 300msec and 400msec for the dummy's head. All the FE models shows reasonable agreement to the sled test for the first two phases of head deceleration response.

Figure 7.12 shows the head/neck bending moment against time for the models and sled test. Both frict-1 and frict-2 are good models in reproducing the sled test results. The baseline model has slightly over-estimated the head-neck bending moment especially towards the end of the simulation. All FE models considered here again have failed to obtain the peak bending moment occurred at 200msec during the sled test.

Figure 7.13 shows the leg contact force against time for the models and sled test. The model frict-2 has obtained a rather high leg contact force of 7.5kN and frict-1 has achieved two distinct peak contact forces for the lower legs : the first with 2.1kN at 160msec and the second one with 4.5kN at 220msec. The high contact force of 7.5kN for the lower leg is in excess of the allowable threshold value of 3.8kN, thus indicating that leg injury is likely to be inflicted.

In summary, within the range of the coefficient of contact friction of 0.45 to 0.55, the PAMCRASH dummy model could fairly well reproduce the sled test results.

7.5.3 Effects of gravity rise time on the dummy's kinematics

Figure 7.14 shows the plot of z-x trajectories for the models studying the gravity rise time. This figure indicates that increasing gravity rise time has slightly risen the dummy's head trajectory prior to the head/seat-back collision. All the models rebound with a downward and backward swinging movement and increasing gravity rise time tends to lower the head trajectory during this phase of motion.

Figure 7.15 shows the deceleration-time history of the dummy head for the models and sled test. Both grav-1 and grav-2 have produced identical head deceleration-time history as the baseline case, indicating that the small range of gravity rise time considered here has not significantly altered the dummy head deceleration response.

Figure 7.16 shows the head/neck bending moment against time for the models and sled test. This figure has indicated that gravity rise time has no significant effect on the head/neck bending moment prior to the completion of the head/seat-back collision, but decreasing the gravity rise time would reduce the head/neck bending moment during the rebound phase of the dummy's head motion.

Figure 7.17 shows the leg contact force against time for the models and sled test. All models has produced identical results for these plots.

To summarise, within the range of the gravity rise time of 0.2 to 0.8msec, no significant difference in dummy response were predicted.

7.5.4 The optimal set of input parameters for the PAMCRASH's dummy model

From the previous analyses, it was found that increasing the cushion stiffness and contact friction of the baseline case could be of merit in producing a dummy response that is closer to the actual sled test. Gravity rise time has no significant effect on the dummy response. It is now required to select an optimal set of input parameters for the PAMCRASH dummy model.

After some trial & error modelling, the optimal set of input parameters was found as :

Model name	Seats' cushion stiffness (N/mm)	Dynamic contact coefficient of friction	Gravity load curve rise time (msec)
c3fwd	+5%	0.47	3

Table 7.2 : The input variables for the optimal model, c3fwd.

The trajectory and deceleration-time history of the dummy's head for the model c3fwd is shown in Figures 7.18 and 7.19 respectively. The head/neck bending moment is shown in Figure 7.20 and the leg contact force is shown in Figure 7.21. These figures have also included the results from the baseline case and sled test. All the figures have

shown that c3fwd has improved (i.e. closer to the sled test) the baseline model in term of dummy response, and the set of input parameters listed in Table 7.2 is thus confirmed for used in future simulation work with the forward facing dummy.

Table 7.3 summarises the results of injury potential for the model c3fwd, with sled tests' results included as comparison :

	Allowable	Sled test	c3fwd
Head injury criteria (*HIC*)	1000	219 (240-260ms)	283 (243-262ms)
3msec exceedance for head	80g	64g	62.6g
Peak head/neck bending moment (Nm)	190 (Flexion) 57 (Extension)	39-F (at 267ms)	43-F (at 271ms)
Maximum leg contact force (kN)	3.8	---	3.9

Table 7.3 : Summarised results for the forward facing dummy subjected to the C3 pulse.

The results in Table 7.3 together with Figures 7.19 and 7.20, have shown that a satisfactory level of confidence is achieved by PAMCRASH dummy models in reproducing the actual kinematics of the dummy, which render accurate predictions for the potential of injury.

7.6 Conclusions

The following conclusions can be drawn from Chapter 7 :

(1) The PAMCRASH dummy model, even with simple articulated rigid bodies, has shown to be a reasonably accurate tool in reconstructing a dummy response during sled tests;

(2) For articulated rigid bodies to successfully represent a dummy, the cushion stiffness shown in Figure 7.2 can be tuned by stiffening 10%;

(3) The contact coefficient for forward facing PAMCRASH dummy works best between 0.45 and 0.55;

(4) The gravity rise time has no significant effects on the PAMCRASH dummy model;

(5) The optimal set of input parameters for a forward facing PAMCRASH dummy are : cushion stiffness +5% over those shown in Figure 7.2, contact coefficient 0.47, gravity rise time 3msec;

(6) Contact friction is identified as the most influential parameters in this parametric study, it should be carefully studied for future parametric validations of dummy model with different set-ups;

(7) It is more realistic to apply the acceleration pulse to the seats and floor rather than on the dummy model itself as the later tends to constrain the dummy movements;

(8) This chapter has identified some parameters for PAMCRASH dummy models to behave in a similar manner to those in sled tests. Future simulations of similar kind could now be modelled with confidence.

References

[1] The Motor Industry Research Association, "Post Clapham Programme Interior Crashworthiness Development Volume 3 : HyGe Sled Testing.", MIRA Report, No. 427909, March 1991.

[2] The Motor Industry Research Association, "Post Clapham Programme Interior Crashworthiness Development Volume 2 : Computer Modelling.", MIRA Report, No. 427909, March 1991.

[3] Swindell, M., "Crashworthiness Development : Theoretical Methods for the Assessment of Vehicle Interiors & Occupant Kinematics.", British Rail Research Report, No. LR/VST/92/042, Derby, November 1992.

[4] Robinson, K. P., "Injury Criteria for Use in a Railway Environment.", British Rail Research Report, No. LR/VST/94/001, Derby, May 1994.

[5] Rock, N. I. C., Brownson, P. & Haidar., R., "Crash Victim Simulation Using Spinal Modelling.", Proc. IMechE. Conf. on CAE in Vehicle Design Crashworthiness Modelling, Paper No. 6, IMechE HQ, London, p. 1, 2 November 1994.

[6] Prasad, P. & Chou, C. C., "A Review of Mathematical Modelling.", Proc. ASME Winter Annual Conf. on Crashworthiness and Occupant Protection in Transportation Systems, (Khalil, T. B. & King, A. I eds.), San Francisco, California, p. 95, 10-15 December 1989.

Chapter 8
Assessment of kinematics of forward facing occupant, Part II : Effects of different acceleration pulses on the occupants

8.1 Introduction

The last chapter identified the required input parameters for the PAMCRASH 50th% male hybrid III dummy model to behave in a similar manner to the dummies in actual sled tests. This chapter furthers the study of dummy kinematics by looking into the effects of selected acceleration pulses on the dummies. Previously in chapters 3, 4, 5 and 6, the effects of various parameters on the energy distribution pattern along colliding rakes has been studied. This chapter extracts the acceleration pulses from the mass-spring models in these chapters and applies them to the dummy models. All dummy models studied here have the Class 423 interior open bay seating arrangement.

Section 8.2 introduces the selected acceleration pulses derived from the mass-spring models of previous chapters. Most of these were acceleration pulses experienced by the leading coach and some of them were derived from the mass-spring models with a small interfacial centre mass which introduced small perturbations in the acceleration response, these have to be filtered away before application to the dummy models. The selected pulses were divided into various parametric series and used as input to the dummy models, which were also categorized into different parametric series according to the pulse they received. A total of 19 dummy models were created. The results and analyses of these dummy models are described in Section 8.3. All the dummy models discussed in this chapter were in forward facing configuration. One of the aims of this chapter is to study the kinematics for occupants sitting in trains with mixed crush-zones' characteristics (as in the model mixn6 in Chapter 6) colliding at 60km/h. Hence two models were included in Section 8.3, with one subjected to the M1 pulse and the other the M6 pulse. The M1 pulse is derived from the acceleration-time history of the leading coach of the model mixn6 and M6 was derived from the last coach. In Section 8.4, general findings and observations of the modelling results are discussed with emphasis placed on the potential of head injury (the HIC scores) as predicted by the dummy models. Section 8.5 concludes this chapter by summarizing the main findings.

8.2 The acceleration pulses derived from previous Chapters

8.2.1 Introduction

Figure 8.1 shows the acceleration-time history of the six coaches (from the first coach nearest to the impact plane to the last) as predicted by the model mixn6, in 'raw' form. From these graphs, it can be seen that : (1) All coaches have a main pulse which lasted for about 15msec and except for the last coach, all other coaches have a small triangular relieved pulse during the first half of the main pulse; (2) There is a violent perturbation towards the end of each main pulse (except the last coach) which quickly

dies away; (3) Once the perturbation has damped out, the coach settles in small oscillations until the end of the simulation.

Note that coaches in the initially moving rake would experience deceleration and those in the initially stationary rake would be accelerated in a symmetrical manner with the impact plane as the plane of symmetry.

The main pulse is a direct result of the primary collision between the coach and its leading vehicle. These pulses appear in sequence demonstrating that as the leading coach completes its primary collision the following coach takes over, which is a designed function of a crashworthy rake. The triangular relief in the initial phase of the main pulse is caused by the forces in the trailing interface couplers, the last coach has no trailing interface hence no such relief was observed in its main pulse. Note that the couplers have decelerated their trailing coach while relieving (accelerating) the leading one.

The perturbations were caused by the small interfacial masses in the model. Recall that the impact interface does not have any small central mass because velocity-sensitive couplers were assumed to break away rather quickly at this interface. Hence they were not modelled, which lead to the omission of the small central mass in the impact interface. The other interfaces have a small central mass. These small masses settled earlier than the coaches (big masses) and unloading soon occurred at the leading springs of these small masses only to be followed by reloaded by the trailing springs. These perturbed activities happened when the interface concerned was about to settle and hence they appeared only as brief disturbances towards the end of the main pulse of the front coach. The last coach does not have a trailing interface and hence exempts itself from such disturbance.

The small oscillatory motion for every settled coach is to be expected since elastic unloading and reloading is allowed in the model.

8.2.2 The processing of raw acceleration pulses

The raw acceleration pulses have to be processed before they could be used as input to the dummy models. These raw pulses were processed in two respects : elastic oscillatory motions about the y-axis (during settling) and the perturbation at the end of each main pulse were filtered manually. The first process is justified since it has been shown that such oscillatory components of this kind have no apparent effect on the dummies. The second process is necessary because the perturbations caused by the small interfacial masses are not real and it is only a modelling side effect introduced as the result of using the mass-spring representation to model a rake of coaches linked by Oleo couplers. Figure 8.2 shows the processed version of those pulses experienced by the same coaches shown previously in Figure 8.1. No special technique were involved in processing these pulses. The perturbations and oscillatory components of the individual coach's acceleration-time history could be easily identified and the duration of the main pulse is also clearly shown in Figure 8.1. The data of the raw pulse were manually inspected and corrected.

Small deceleration pulses were introduced by the couplers in front of Coach 2 to 6 before the coaches received their primary impact. Such small pulses acting on their own (i.e. separated well apart from the main pulse) are thought not to have significant effects (average about 1g for 5msec) on the passengers occupying these coaches apart from slight jerks. The coach nearest to the impact plane has no such pulse but all the other coaches have a small triangular pulse prior to their main impact which would be ignored and only their main pulses would be used as input to the dummy models. Consequently all the main pulses for Coach 2 to 6 would be shifted in time so that their starting points coincide with the origin.

8.2.3 The acceleration pulses used in this Chapter

Figure 8.3 shows the 4 acceleration pulses derived from leading coach of Gap1 to Gap4, the theoretical gap models in Chapter 4, i.e. mass-spring models without couplers but with varying gap size. This graph shows that only the tuned gap size (0.53m) has a single and continuous pulse, the others have separated their main pulses in two. The larger the model gap size, the longer would be the duration of the first portion of these pulses. The acceleration experienced by a coach is a direct result of force differential between both of its ends. For the case of the leading coach in Gap1 to Gap4 we need to refer to the force-time history of interface 1 and 2 of these theoretical gap models which were shown previously in Figures 4.4a, 4.5a, 4.6a and 4.7a. It is clear that as long as the force acting on the leading end of the coach (thus decelerating it) remains unopposed from the other end, the coach would decelerate according to Newton's second law. The smaller the interfacial gap the sooner the opposing force would act from the trailing end. Since the two forces are equal and opposite the coach starts to move at constant velocity, which explains the brief moments of zero acceleration in some of the pulses shown in Figure 8.3. The acceleration would pick up again only if there is a further force differential between the coach's ends. This could occur when the passenger compartment is collapsing causing a higher force to act from the leading end of the coach, or when the leading interface of the coach has completely unloaded with a simultaneous loading from its trailing interface. The former has an interfacial gap size smaller than the tuned case. The latter has one which is greater. Note that the 4 pulses shown in Figure 8.3 have been named N0, N25, N53 and N75. The 'N' denotes 'no couplers'. The figures followed by it show the theoretical gap size in centimetres.

Figure 8.4 shows the 2 acceleration pulses derived from the leading coach of Cp1 and Cp2, the models in Chapter 4 with both Oleo couplers and gaps. The small triangular reliefs at the initial phase of these pulses caused by the couplers are clearly visible. The leading coach in Cp1 has a step rise for the second half of its pulse due to the infringement of the passenger compartment. The duration of this pulse is shorter compared to its counterpart in Cp2. Cp2 has not infringed the passenger compartment due to the extra length of crush zones at the impact interface. One of the disadvantages in saving the passenger compartment is to subject the coach to a pulse of greater duration, although the pulse's average magnitude is less. The two pulses shown in Figure 8.4 are named O1 and O2, 'O' denotes that Oleo couplers are being considered. '1' indicates that the infringement of passenger compartment has occurred. '2' indicates otherwise.

Figure 8.5 shows the 3 pulses derived from the leading coach of Iv40Gp38, Iv40Gp53 and Iv40Gp70, models that included Oleo couplers in Chapter 4 with 40mph impact velocity but 3 varying gap sizes. Figure 8.5 suggest that the gap size and pulse duration are proportional to each other. This agrees with the previous discussions about the pulse duration and gap size of the theoretical gap (coupler-less) models. It is to be noted that the mass-spring models have extended crush zones so that the passenger compartment didn't get crushed. The three pulses shown in Figure 8.5 are named G38, G53 and G70.

None of the above pulses have considered the effects of damping. Figure 8.6a shows two pulses, one of which was derived from the leading coach of Iv30Gp53 (from Chapter 4) without any damper and the other was with 0.5% critical damping. Damping raises the pulse magnitude initially but slowly reduces it as the pulse progresses. Damping also causes earlier termination of the pulse, since the dampers help to dissipate some collision energy which would cause earlier settling of the colliding coaches. Figure 8.6b shows another pair of pulses, derived from the leading coach of Iv40Gp53 (from Chapter 4) with and without 0.5% critical damping. With these pulses, effects of damping on the dummy kinematics could be studied at moderate (30mph) and higher (40mph) colliding velocities. The two pulses in Figure 8.6a are named D30 and V30 to represent the pulse with and without damping respectively. The other pair shown in Figure 8.6b are named D40 and V40. Note that the V40 pulse is the same as the G53 pulse described in the previous paragraph.

Figure 8.7 shows three pulses derived from the leading coach cf1.6, cf2.3 and cf3.0 in Chapter 6 and these pulses are named F16, F23 and F30 respectively. Figure 8.8 shows the two pulses derived from the leading coach of rp1.95 and rp2.30 and they are named R19 and R23 respectively. Damping was included in these pulses.

Figure 8.9 shows the M1 pulse, which is extracted from the acceleration-time history of the leading coach in Figure 8.2 and Figure 8.10 shows the M6 pulse, which is extracted from the sixth (last) coach.

All the above pulses were 'fed' as input load curve to the dummy models.

Table 8.1 over the page summarizes the dummy models which were analysed in Section 8.3.

Parametric series	Number of dummy models created	Description of input pulses	Objectives of the parametric series
N-series	4	N0, N25, **N53** & N75	Effects of theoretical gap size on the dummy kinematics without Oleo couplers
O-series I	1	<u>N53</u> & **O1**	Effects of Oleo couplers on the dummy kinematics with no infringement of passenger compartment
O-series II	1	<u>O1</u> & O2	Effects of Oleo couplers on the dummy kinematics with infringement of passenger compartment
G-series	3	G38, **G53(V40)** & G70	Effects of gap size on the dummy kinematics (with Oleo couplers)
D-series I	2	V30 & D30	Effects of damping at 30mph on the dummy kinematics
D-series II	1	<u>V40(G53)</u> & D40	Effects of damping at 40mph on the dummy kinematics
F-series	3	**F16**, F23 & F30	Effects of the magnitude of crush zones' collapse force on the dummy kinematics
R-series	2	<u>F16</u>, R19 & R23	Effects of hardening slopes of the crush zones on the dummy kinematics
M-series	2	M1 & M6	Effects of the coach's position (within a rake) on the dummy kinematics

Note :

1) The name of a dummy model is the same as the pulse it received. A total of 19 forward facing dummies on a Class 423 open bay seats subjected to various pulses were simulated;
2) The underlined entries denote that the dummy model have been simulated in other parametric series (the bold entries), thus they have not been recreated but the results were 'borrowed' from the relevant model for parametric comparison.

Table 8.1 : The total number of dummy models simulated for discussion in section 8.3, broken down into various parametric series according to the pulse they received.

Apart from the applied pulse, all other input parameters such as seats' dimensions, contact-stiffness load curves between the dummy and the various parts of the opposite seat, contact friction, gravity load curve, dummy initial seating position etc., are the same as those described in the model c3fwd in Chapter 7.

8.3 Results of the forward facing dummy models subjected to the 'N', 'O', 'G', 'D', 'F', 'R' and 'M' pulses

8.3.1 Forward facing dummies subjected to 'N-series' pulses

Figure 8.11 shows some of the sequence of animation for the dummy model N53, the model with an applied pulse derived from the tuned theoretical gap (no couplers) mass-spring model. The response of the dummy looks similar to those with C3 pulse applied. Figure 8.12 shows the head acceleration-time history for various dummy models in the N-series. The dummy with the 'largest-gap' pulse-N75, has produced a distinctively high head acceleration of nearly 110g at 0.26sec, indicating that severe injury is likely for this applied pulse. This is within expectations since the N75 pulse has the largest area under its acceleration-time graph, i.e. the pulse had produced the highest relative velocity change to the coach among all the N-series pulses (refer to figure 8.3). The N75 pulse has two separate parts. The first part alone is more durable than the N53 pulse. The other models have produced head accelerations with similar orders of magnitude to those observed in the parametric study in Chapter 7. However, the dummy model with the 'gapless' pulse-N0 has produced consistently low head accelerations throughout the simulation period. The N0 pulse also has two parts : a sudden rise from 0g to about 5.8g at the beginning which quickly relieved to 0g within 40msec, and not until another 40msec (i.e. at 80msec) before it picked up the second half of the pulse which acted for a longer duration (see Figure 8.3). Figure 8.13 shows the sequence of animation for this dummy model during the simulation. The full relief of the pulse during the first 80msec has effectively weakened the pulse's action and the dummy-to-opposite-seat impact was thus considerably less severe, this will be demonstrated later. Once the dummy's lower legs made contact with the opposite seat-edge, it's whole upper body rotated about the contact points which encouraged sliding action between the head and the opposite seat-back as the head bowed towards the seat-back. Such trajectory of the head avoids the injurious head-on impact with obstructions and thus provides lesser chance of serious injury to the occupant.

Figure 8.14 shows the graph of head/neck bending moment against time. The N75 pulse is again seen here to cause the most harm to the occupant. A peak 289Nm moment in flexion was registered. This is one and a half times the allowable 190Nm. The other dummy models were shown to be considerable safer in this respect, although the dummy model with N25 pulse has produced a peak head/neck bending moment of 202Nm in flexion. This is only 6% higher than the allowable value. Nevertheless, it does indicate a fair chance for neck injury to occur when a forward facing occupant is subjected to the N25 pulse.

Figure 8.15 shows the leg contact force for the dummy models in the N-series. All models have exceeded the allowable 3.8kN, indicating that lower leg injuries are likely. The N75 pulse has again produced the worst leg contact force (about 7kN) confirming its severity for a forward facing occupant.

Table 8.2 over the page summarizes the results for the dummy models in the N-series.

	Allowable	Model N0	Model N25	Model N53	Model N75
Head injury criteria (HIC)	1000	90 (338-374ms)	713 (262-295ms)	383 (260-296ms)	1430 (250-279ms)
3msec exceedance for head	80g	31.7g	83.4g	63.1g	117g
Head/neck bending moment (Nm)	190 (Flexion) 57 (Extension)	26.8-E (at 390ms)	202-F (at 290ms)	148-F (at 290ms)	289-F (at 270ms)
Maximum leg contact force (kN)	3.8	5.56	6.73	6.42	7.05

Table 8.2 : Comparison of results for various forward facing dummy models in the N-series.

The results shown in Table 8.2 have demonstrated that the N0 pulse produces the safest results for a forward facing occupant in the N-series, but results from Chapter 4 indicated that part of the passenger compartments of the two leading coaches (in the impacting and impacted rakes) had been crushed, so passengers sitting adjacent to the crush zones would lose their required survival space. In this case there is a trade off between structural and interior crashworthiness.

N75 has produced the worst results consistently in all the selected injury criteria. Previously in Chapter 4, it was found that gaps larger than the optimal size have produced more even energy distribution along colliding rakes than those which are smaller. The results here have shown the opposite : larger gaps produce more injurious pulses for the passengers. This again has posed a contradiction between the requirements of structural and interior crashworthiness. This contradiction was first noted by Chatterjee and Carney [1]. Optimisations of a crashworthy design should always be sought by mediating between the structural and interior crashworthiness requirements.

N53 has produced the second best results in Table 8.2, without infringing the passenger compartments. The only failure of compliance to the selected injury criteria by this dummy model was the high contact forces on the lower legs. If the leg contact force could be improved for this model by modifying the seat-edge design or otherwise, this pulse seems able to satisfy both structural and interior crashworthiness requirements.

8.3.2 Forward facing dummies subjected to 'O-series' pulses

Figure 8.16 shows the head acceleration-time history for the two dummy models N53 and O2. The dummy's head in the model N53 has a peak acceleration of 65g during the simulation with a HIC score of 383. Correspondingly in O2, the dummy's head has

a slightly lower peak of 58g with a HIC score of 225. Note that the dummy's legs in N53 made an earlier contact with the opposite seat-edge. This occurred as the N53 pulse had not been relieved by the couplers' forces which increased the initial relative velocity between the dummy and the opposite seat. Figure 8.17 shows the leg contact force for the two models. It is clear that the dummy model subjected to the N53 pulse has suffered higher leg contact force. Hence it is possible to conclude that the couplers' forces had delayed the legs/seat-edge contact and also reduced the impact severity. Slightly higher HIC score was registered in the model N53 despite the fact that the area under the O2 pulse (8.81m/s) is bigger than in the N53 pulse (7.88m/s). The 'gentler' initial contact offered by the O2 pulse is thought to aid the subsequent dummy's upper body trajectory which ameliorates its overall head injury potential during the whole process of secondary impact.

Figure 8.18 shows the graph of head/neck bending moment against time for the two models. The dummy in O2 developed a peak head/neck bending moment of 46.4Nm in extension whereas in N53 it was 148Nm in flexion. Both are within the allowable limits.

Figure 8.19 shows the dummy's head acceleration-time history for the two models O1 and O2. The O1 pulse infringed the passenger compartment whereas the O2 pulse did not. The O1 pulse had a stronger average magnitude but was not as long as the O2 pulse. From Figure 8.19, it is seen that O1 produced a sharp peak of about 70g at 0.25sec and the HIC score was 295, as compare to 225 in O2. The stronger pulse experienced by the occupant in O1 due to infringement of the passenger compartments, has an adverse effect on the forward facing occupants during secondary collisions.

Figure 8.20 shows the leg contact force for the two models. Here we see that couplers have helped in reducing the leg contact force. Both dummy models have predicted a leg contact force of about 4.2kN, which is still higher than the allowable 3.8kN but much improved from the 6.42kN obtained by the model N53. Figure 8.21 shows the head/neck bending moment against time for the two models. The dummy in O1 had developed a peak head/neck bending moment of 64.7Nm in extension whereas in O2 it was 46.4Nm in extension as well. The former exceeded the allowable 57Nm limit, indicating that neck injuries are likely. In all, the dummy model with the O1 pulse predicted more harmful results consistently in all the selected injury criteria when compared to the dummy with O2 pulse. For rakes with proper gap size and coaches connected by Oleo couplers, crush zones should have sufficient energy dissipating capacity in order not to involve crushing of the high strength passenger compartment. Otherwise, some passengers will be crushed and others suffer high possibilities of serious/fatal injuries during the secondary impacts.

Table 8.3 over the page summarizes the results for the O-series.

	Allowable	Model N53	Model O2	Model O1
Head injury criteria (HIC)	1000	383 (260-296ms)	225 (262-281ms)	295 (247-262ms)
3msec exceedance for head	80g	53.1g	56.5g	69.5g
Head/neck bending moment (Nm)	190 (Flexion) 57 (Extension)	148-F (at 290ms)	46.4-E (at 320ms)	64.7-E (at 300ms)
Maximum leg contact force (kN)	3.8	6.42	4.36	4.46

Table 8.3 : Comparison of results for various forward facing dummy models in the O-series.

8.3.3 Forward facing dummies subjected to 'G-series' pulses

Figure 8.22 shows the head acceleration-time history for the three dummy models in the G-series. G38 has produced the safest head acceleration with a peak of about 40g and a HIC of only 61.6. G53 has a peak of 60g with a HIC of 266. G70 has a peak of about 100g with a HIC of exactly 1000. The area under the three pulses are : G38-7.63m/s, G53-8.83m/s and G70-9.87m/s. The bigger the gap, the larger the change in the relative velocity due to longer pulse duration. So the head injury potential predicted by models in the G-series is correlated to the change in the coach's velocity caused by the pulse.

Figure 8.23 shows the graphs of head/neck bending moment against time for the three models discussed here. G38 has a peak bending moment of 18.5Nm in extension at 0.38sec. This again is the safest among the three models. G53 predicted a peak of 46.8Nm in extension at 0.32sec which is the second safest. G70 has a peak of 70.3Nm in extension at 0.32sec. G70 is the only model that exceeded the allowable limit of head/neck bending moment for models in the G-series.

Figure 8.24 shows the leg contact force for the three models. G53 and G70 have similar peak contact force of about 4.5kN which exceeded the allowable limit of 3.8kN. G38 has a peak of 3.67kN. So far this is the only model that passed the leg contact force criterion.

Table 8.4 over the page summarizes the simulation results in the G-series.

	Allowable	Model G38	Model G53	Model G70
Head injury criteria (HIC)	1000	61.1 (284-305ms)	266 (262-280ms)	1000 (254-269ms)
3msec exceedance for head	80g	34.4g	60.1g	104g
Head/neck bending moment (Nm)	190 (Flexion) 57 (Extension)	18.5-E (at 380ms)	46.8-E (at 320ms)	70.3-E (at 320ms)
Maximum leg contact force (kN)	3.8	3.67	4.36	4.43

Table 8.4 : Comparison of results for various forward facing dummy models in the G-series

8.3.4 Forward facing dummies subjected to 'D-series' pulses

Figure 8.25 shows the head acceleration-time history for the four dummies in the D-series. Dummies in V30 and D30 have suffered lesser head acceleration compared to V40 and D40. The HIC scores are : V30-15.2, D30-67.2, V40-266 and D40-772. Damping increases the head injury potential at both collision velocities (30mph and 40mph). Damping also causes earlier contact between the legs and the opposite seat-edge. This is due to the higher initial pulse magnitude produced by damping. Thus higher leg contact force is expected for models with damping. This is confirmed in Figure 8.26, which shows the leg contact force for the four models. V30 is the only model in the D-series with a leg contact force less than 3.8kN, indicating that the other models have predicted possible leg injuries for the forward facing occupant.

Figure 8.27 shows the head/neck bending moment for the four models. Their peak moments are : V30-16.7Nm in extension, D30-41.5Nm in flexion, V40-46.8Nm in extension and D40-164Nm in flexion. Due to the different modes of bending predicted by these models, it is difficult to conclude the effects of damping on the head/neck bending injury potential.

Models with damping considered here have consistently predicted more injurious results than those without damping for the forward facing dummy. It is important that future simulations should consider damping.

Table 8.5 over the page summarizes the results predicted by dummy models in the D-series.

	Allowable	Model V30	Model D30	Model V40	Model D40
Head injury criteria (HIC)	1000	15.2 (267-302ms)	67.2 (298-325ms)	266 (262-280ms)	772 (246-279ms)
3msec exceedance for head	80g	14.6g	31.1g	60.1g	88.9g
Head/neck bending moment (Nm)	190 (Flexion) 57 (Extension)	16.7-E (at 360ms)	41.5-F (at 340ms)	46.8-E (at 320ms)	164-F (at 270ms)
Maximum leg contact force (kN)	3.8	3.66	4.83	4.36	7.27

Table 8.5 : Comparison of results for various forward facing dummy models in the D-series

8.3.5 Forward facing dummies subjected to 'F-series' pulses

Figure 8.28 shows the head acceleration-time history for the three dummies in the F-series. The dummy in F30 suffered an excessively severe acceleration of 100g for about 25msec. The HIC scores for the three models are : F16-990, F23-475 and F30-2040. F16 has the lowest pulse magnitude but it sustains the longest duration of 23msec among all the pulses considered in this chapter. This has suggested that prolonged pulses at low magnitude are also very harmful to passengers. The HIC results in the 'F-series' have suggested that the crush zone collapse force can neither be too high nor too low, 2.3MN (from which the F23 pulse is derived) seems to be an appropriate value.

Figure 8.29 shows the head/neck bending moment for the three models. Their peak moments are : F16-67.5Nm in flexion, F23-152Nm in flexion and F30-87.4Nm in extension. The only dummy model considered here which didn't fulfill the head/neck injury criterion is F30. This model has also predicted the highest HIC so far in this chapter. Now the failure to meet the head/neck injury criterion has confirmed its unsuitability to be applied to occupants. Note that previously in Chapter 6 the model with the 3MN constant collapse force produced the best energy distribution (compared to cases with 1.6MN and 2.3MN constant collapse force) along the 5 to 5 colliding rakes. Now we see the disastrous effects of its derived pulse on a forward facing passenger. This has again emphasized the fact that the requirement to produce the most even distribution of collision energy along colliding rakes very often fails to meet the interior crashworthiness requirements. A balance should be struck between these two separate requirements in order to produce an optimal crashworthy design for rail passengers.

Figure 8.30 shows the leg contact force for the three models. The strong pulse of F30 has caused an excessively large leg contact force of about 17.5kN which is so far the highest encountered in this chapter. All models in the F-series have exceeded the maximum allowable leg contact force of 3.8kN.

Table 8.6 below summarizes the simulation results in the F-series :

	Allowable	Model F16	Model F23	Model F30
Head injury criteria (HIC)	1000	990 (281-296ms)	475 (237-268ms)	2040 (290-326ms)
3msec exceedance for head	80g	107g	73.1g	97.8g
Head/neck bending moment (Nm)	190 (Flexion) 57 (Extension)	67.5-F (at 300ms)	152-F (at 265ms)	87.4-E (at 275ms)
Maximum leg contact force (kN)	3.8	4.80	4.85	17.7

Table 8.6 : Comparison of results for various forward facing dummy models in the F-series

8.3.6 Forward facing dummies subjected to 'R-series' pulses

Figure 8.31 shows the head acceleration-time graph for the three models in the R-series. R19 and R23 score better HIC and lesser peak accelerations than F16 despite greater areas under their pulses. F16 delayed the head to seat-back collision. This pulse has sustained a very long duration which remained active when the dummy first made contact with the opposite seat. Some of the models discussed previously also have this characteristic, i.e. the pulse was active while the forward facing dummy contacted the opposite seat-edge. These models are N25, N75, G70 and D40, all of them have outstandingly long duration for their pulses. They also share some common features in their results : high HIC score; severely high peak acceleration for the head which occurs during the head to seat-back collision; and after the major collision the dummy's head tends to settle at relatively high acceleration. These characteristics of dummy response are not found in the other dummy models except F30. In fact if F30 is taken out, N25, N75, G70, D40 and F16 would stand out prominently as the five most harmful pulses discussed in this chapter. This point will be re-addressed later in Section 8.4.1.

Figure 8.32 shows the head/neck bending moment against time for the models in the R-series. All except R19 passed the allowable limits.

Figure 8.33 shows the leg contact force for the three models. R23 has the highest leg contact force which is not surprising since the initial portion of its pulse is stronger than the other two pulses. All models have exceeded the allowable 3.8kN limit, indicating that leg injuries are likely for the occupants.

The results for models in the R-series are summarized on next page.

	Allowable	Model F16	Model R19	Model R23
Head injury criteria (HIC)	1000	990 (281-296ms)	425 (254-269ms)	518 (234-248ms)
3msec exceedance for head	80g	107g	74.9g	83g
Head/neck bending moment (Nm)	190 (Flexion) 57 (Extension)	67.5-F (at 300ms)	63.7-E (at 315ms)	44.5-F (at 260ms)
Maximum leg contact force (kN)	3.8	4.80	4.49	6.37

Table 8.7 : Comparison of results for various forward facing dummy models in the R-series

F16 in Table 8.7 should be ignored if the effect of hardening slopes on the occupant kinematics is to be studied. For it has introduced an additional factor (the pulse remains active while the dummy contacted the opposite seat-edge) to increase the injury potential of the occupants. Table 8.7 suggests that increasing the ramp slope would increase the injury potential for the forward facing occupant.

8.3.7 Forward facing dummies subjected to 'M-series' pulses

Figure 8.34 shows the acceleration-time history for the dummies' heads in the M-series. M1 produced a more injurious result than M6. M1 is a stronger pulse, in term of the average magnitude (and thus the area under the pulse). That is why the dummy in M1 made the head to seat-back collision earlier than the one in M6. The previous mass-spring models in Chapter 6 demonstrated that the last coach has absorbed the least amount of collision energy and sustained minimum crush. Now it is seen that the pulse it received is also the least harmful within the whole rake. However, for the present M-series, both M1 and M6 satisfied the head injury criteria.

Figure 8.35 shows the results for the head/neck bending moment against time in the M-series. Here the M6 had produced a large moment of 234Nm in flexion. M1 had a peak moment of 116Nm in flexion. M1 in this case has passed the head/neck bending criterion but M6 failed.

Figure 8.36 shows the leg contact force for the two models. Due to stronger pulse in M1, leg contact force is much higher than that of the M6. M6 predicted a maximum leg contact force of 3.17kN, which is lower than the 3.8kN limit.

The results for the two models in the M-series are summarized in Table 8.8. on the next page.

	Allowable	Model M1	Model M6
Head injury criteria (HIC)	1000	416 (243-258ms)	360 (292-325ms)
3msec exceedance for head	80g	77.1g	59.1g
Head/neck bending moment (Nm)	190 (Flexion) 57 (Extension)	116-F (at 270ms)	234-F (at 320ms)
Maximum leg contact force (kN)	3.8	6.91	3.17

Table 8.8 : Comparison of results for various forward facing dummy models in the M-series

8.4 Discussions

8.4.1 Correlation between 'area under the pulse' and HIC

The log-log plot of HIC against 'area under the pulse' (ΔV) for all the models is shown in Figure 8.37. Area under the pulse represents the change in the coach's velocity caused by the application of the pulse. Large scattering is observed. If, however, the data are segregated into four groups, each with a common variable, then some patterns could be observed from this graph. The four groups are described as follow :

(1) The φovlp group : Models from this group have their pulses still active while the forward facing occupant reaches the opposite seat-edge. The general effects of this on the occupant is to increase his/her injury potential. Five models from Section 8.3 qualified for this group : N25, N75, G70, D40 and F16.

(2) The φhyge group : Models from this group have very high average acceleration on the pulse. Average acceleration (A_m) is calculated by $\Delta V/t_p$ where t_p is the effective duration of the pulse. Originally from the pool of models discussed in Section 8.3, only F30 has attained an A_m of 8.4g, all the others have not exceeded 6.6g. To qualify for this group, the A_m of the applied pulse should be above a cut-off value and this lies between 8.4g and 6.6g. So another dummy model with the same ΔV as F30 but a lower A_m of 7g was created, i.e. the F30 pulse is scaled both in the x and y axes with a lower A_m but longer t_p. This is to maintain the same area under the pulse. The result of this model is marked '7g' in Figure 8.37. It turned out that 7g qualified for this group so two models were grouped here : F30 and 7g.

(3) The φncop group : Models from this group have no relief in the initial part of their pulses. They are either derived from mass-spring models without couplers or from the last coach. Two models from Section 8.3 were grouped here : N53 and M6. To supplement the data in this group, a dummy model was created with the same ΔV as N53 but with a higher A_m of 6.5g. Results from this model are marked '6.5g' in Figure 8.37.

(4) The φnorm group : Models from this group have terminated the pulse action before the dummy reaches the opposite seat. The A_m of the applied pulse does not exceed 6.7g and the pulse has initial relief caused by the couplers. Many models from Section 8.3 satisfied these requirements : O1, O2, G38, G53(V40), V30, D30, F23, R19, R23 and M1.

Note that N0 was not included in any of the above groups because it has a different (less forceful) trajectory shown in Figure 8.13, caused by the long duration of relief during the initial portion of its pulse. This had produced a different injury mode for the occupant. All the other models have shown very similar trajectories to the one seen in Figure 8.11, so their results could be compared here.

When the data in Figure 8.37 are interpreted separately according to the above groups, it is seen that all groups show a power law correlation between HIC and ΔV, or $HIC = a(\Delta V)^m$, where a and m are constants. That implies that the slope of this graph increases as ΔV increases. It could also be seen that data points from φncop are situated to the left of those from φnorm, which suggests that pulses without an initial relief have the effect of moving to the left of this graph. All the data from φovlp have high HIC scores and so they are located above those in the φnorm. The φhyge data also have high HIC scores and so they tend to position at the top of the graph.

7g has the same ΔV as F30 but its HIC is nearly half of that achieved by F30. Similarly 6.5g has the same ΔV as N53 and yet it scored a much higher HIC. F30 and 6.5g have higher A_m than 7g and N53 respectively. So the HIC of a forward facing occupant could also be correlated with the average magnitude of the applied pulse to which 'he' is subjected. This is discussed next.

8.4.2 Correlation between 'average pulse acceleration' and HIC

Figure 8.38 shows the log-log plot of HIC against A_m for all the models. Data from φhyge and φncop show the power-law relationship between HIC and A_m. Data from φovlp do not. This indicates that if the applied pulse was still active when the occupant contacted the opposite seat-edge, then the HIC of the occupant is not governed by the A_m of the applied pulse but by some other parameters. ΔV as shown from Figure 8.39 is one such parameters, the other is the 'overlapped velocity change' which will be discussed in the next section.

Figure 8.38 also shows that the data from φnorm do not display the power-law behaviour once the A_m of the data points fall below or at the vicinity of 5g; they scatter along the line A_m=5g. Above 5g the data seem to 'behave properly' according to the power law. This suggested that for cases with A_m falling near or below 5g, the HIC are not sensitive to A_m. At this lower range of A_m, the HIC is better correlated to ΔV as suggested by Figure 8.37. At higher A_m the pulse acceleration become influential in governing the HIC of the forward facing occupant. This contention is supported by the data from φhyge and φncop. Figure 8.38 shows that at high A_m the three groups of

data (φnorm, φhyge and φncop) shared identical behaviour of 'log *HIC* against log A_m'.

8.4.3 Correlation between 'overlapped velocity change' and HIC

Those models from φovlp have a durable applied pulse which remains active when the occupant makes contact with the opposite seat-edge. These models scored very high HIC but the ΔV of their pulses were of similar magnitudes with those from φnorm. Also the HIC scores did not show any correlation to the A_m of the applied pulse. Figure 8.39 shows the log-log plot of HIC against 'the change in velocity during the overlapped period (ΔV_{olp})' for the five models in φovlp. The overlap period is the duration when the dummy first made contact with the opposite seat-edge until the applied pulse terminated. ΔV_{olp}. is computed by integrating the various graphs in figure 8.40 showing the final portion of the acceleration pulse for the models in φovlp during the overlapped period. The curve fit for figure 8.39 suggests that there is a threshold HIC of about 500 (intercept of the fitted line, this is half the allowable limit of 1000) for models in the φovlp. The additional power for secondary impact supplied by the prolonged application of the pulse to the forward facing occupant raised the head injury potential for the occupant.

Note Figures 8.37, 8.38 and 8.39 could serves as a rough guide for predicting the HIC of a forward facing occupant in Class 423 open-bay seats once the grouping of the applied pulse could be identified.

8.4.4 Summarised results for all the models

The grand summary of all the modelling results discussed in Section 8.3 is shown in Table 8.9 over the page. In this table, the four selected injury criteria, namely the HIC, 3msec exceedance for the head, head/neck bending moment and leg contact force, are being assessed in a go/no-go manner. If the results of a particular model fulfilled a criterion, an 'O' will be marked for that model in the appropriate column of the table, an 'X' denotes failure to meet the criterion. The last column provides the overall assessment on the model, an 'X' in this column indicates that the model fails at least one of the four chosen criteria, an 'O' in the last column implies that the model has fulfilled all four. It is seen that vast majority of the models fail to meet the maximum leg contact force of 3.8kN. Some of the models passed on all criteria except the leg contact force. Many of these models produced less than 4.8kN of leg contact force, which is about 25% more than the allowable limit. These models have an 'X*' marked on the 'leg contact force' column and a 'Ø' in the last column, which means that the models have potential to score an overall 'O' pending some improvements to the seat design so as to moderately lower the leg contact force to below 3.8kN.

Model	HIC	3msec exceedance for the head	Head/neck bending moment	Leg contact force	Overall results
N0	O	O	O	X	X
N25	O	X	X	X	X
N53	O	O	O	X	X
N75	X	X	X	X	X
O1	O	O	X	X	X
O2	O	O	O	X*	Ø
G38	O	O	O	O	O
G53	O	O	O	X*	Ø
G70	X	X	X	X	X
V30	O	O	O	O	O
D30	O	O	O	X*	Ø
D40	O	X	O	X	X
F16	O	X	O	X	X
F23	O	O	O	X*	Ø
F30	X	X	X	X	X
R19	O	O	X	X	X
R23	O	X	O	X	X
M1	O	O	O	X	X
M6	O	O	X	O	X

Table 8.9 : The overall assessment for the models (pulses).

Note that Table 8.9 is also an assessment of the suitability of the applied pulse on the forward facing occupant. It can be seen that the two most suitable pulses for the forward facing occupant are G38 and V30. G38 bought interior crashworthiness by sacrificing structural crashworthiness since the mass-spring model from which this pulse was derived showed an uneven collision energy distribution along the colliding rakes which overloaded the leading interface. V30 has comparatively low impact velocity. The relatively low kinetic energy for this case produced a short pulse duration with relatively small ΔV which resulted in its excellent 'performance' in Table 8.9.

The three worst pulses (fail on all four criteria) are N75, G70 and F30. The first two are from the φovlp group and the last has excessively high A_m.

The N53, R19, R23, M1 and M6 pulse are derived from mass-spring models which produced some of the best energy distributions that are currently aspired to. Table 8.9 found them harmful for the forward facing occupants. This reiterates the fact that the requirement to produce the most even distribution of collision energy along colliding rakes very often contradicts interior crashworthiness requirements. However, it should be noted that all these pulses have done well on the HIC, none of them scored more than 550. Also, N53 and M1 have scored very well on all the criteria except the leg contact force. M6 has only exceeded the allowable head/neck bending moment by less

than 25% but has scored extremely well on the other criteria. Thus these three models have demonstrated great potential to be improved for achieving the overall 'O'.

The recommended pulses for the forward facing occupant are O2, G53, V30, D30 and F23, but the leg contact force for these models (except V30) must be improved. These pulses were derived from mass-spring models with acceptable energy distribution along the colliding rakes. They have thus satisfied both the interior and structural crashworthiness requirements.

8.4.5 Chest acceleration

Traditionally the limitation for chest acceleration has been no more than 60g for 3msec, but recently Bowmer [2] has recommended a stricter limit of 40g. The chest injury potential are thought to be unimportant for forward facing occupants sitting in open bay seats because the chests of these dummies are unlikely to bear significant injuries. That was thought to be the reason for previous study [3] to ignore the chest injury predictions. Moreover, there are other more realistic criteria for chest injuries such as limiting the chest's deflection to within 44-65mm and also the Viscous Criteria which involves the rate of compression of the chest. Both of these criteria require a deformable dummy's chest and thus are not applicable for the articulated rigid-body dummy used in this thesis. Nevertheless, the accelerations of the dummy chests for all the models could still be extracted from the modelling results and are tabulated in Table 8.10 below :

Model	3msec exceedance for chest	Model	3msec exceedance for chest
N0	17.2g	D30	18.8g
N25	28.6g	D40	26.6g
N53	25.3g	F16	31.5g
N75	29.7g	F23	22.1g
O1	15.8g	F30	56.5g
O2	20.4g	R19	19.1g
G38	15.6g	R23	27.4g
G53 (V40)	21.5g	M1	25.7g
G70	36.6g	M6	29.0g
V30	9.70g		

Table 8.10 : The 3msec chests' accelerations for various dummy models.

All models have fulfilled the '3msec exceedance' criteria (i.e. none has produced more than 60g for 3msec). This confirms that chest injuries are unlikely for forward facing occupants. Even if the stricter 40g criterion were to be employed, we see that only one model fails to meet such a stringent criterion (F30 failed at 56.5g). The vast majority of the modelling results would still support the conclusion that the chest is unlikely to suffer any injury for the forward facing occupant.

8.5 Conclusions

The following conclusions can be made from this chapter :

(1) There exits a general contradiction between the requirements of structural and interior crashworthiness. A mass-spring model that produced an even energy distribution along the colliding rakes would very often develop acceleration pulses which are very harmful to the occupants. Optimisation of a crashworthy design should always be sought by mediating between structural and interior crashworthiness requirements. Thus it is important that studies on these two subjects should be complementary and not in isolation to each other.

(2) Increasing the gap between coaches has the effect of extending the pulse duration which is very harmful to the occupants.

(3) Breakaway couplers have ameliorated the severity of secondary collision for the occupants by introducing an initial relief on the coach acceleration. Without such initial relieves on the applied pulse, the head injury potential of the occupant would be higher if both pulses (with and without initial relief) have the same change in velocity. Couplers also reduce the leg contact force experienced by the occupant.

(4) Damping force has increased the injury potential of the occupants by raising the initial acceleration of the coach. Hence it is important that mass-spring models should include damping.

(5) In general, increasing the hardening slopes of crush zones would be more harmful to the occupants especially in terms of the head and leg injury potential.

(6) Passengers in the last coach of a rake have a lesser potential (compared to the other coaches in the rake) for injury because it absorbs the smallest amount of energy producing a relatively short-duration pulse.

The following points are applicable only to forward facing occupants sitting in open-bay seats :

(7) The average acceleration of a pulse should not exceed 6.7g. In this respect, the ideal crush zone collapse force should not be more than 2.3MN for trains with 35tonne coaches. It must be emphasized that this only applies to coaches with interior arrangement identical to the Class 423 open-bay seating layout.

(8) The applied pulse should terminate before an occupant encounters any obstacle in front of him/her. Otherwise, the injury potential for the occupant's head increases substantially.

(9) Area under the pulse, or velocity change caused by the pulse, has a power-law correlation to the Head Injury Criteria (HIC) of the occupant to whom the pulse is applied. Figure 8.39 provides some rough estimates on the HIC expected for a forward facing occupant.

(10) When an applied pulse with average acceleration falls near or below 5g, the HIC produced by the occupant is not related to the magnitude of the average acceleration but is sensitive to change in velocity produced by the applied pulse. For applied pulses with higher average acceleration, the pulse magnitude becomes influential in governing the head injury potential of the occupant.

(11) Leg contact forces produced by the models are quite sensitive to the initial pulse magnitude. In this respect, couplers provide some safeguarding for the leg injury but damping force increases the potentials of leg injuries.

(12) Chest injuries caused by excessive acceleration are not likely for forward facing occupants.

(13) Forward facing occupants in an open-bay seating layout are very vulnerable to injuries. Out of 19 models only 2 could fully satisfy all the four chosen injury criteria. This agrees with findings from some recent independent research works, all of which have confirmed that an increase in injury severity occurs for open-bay forward facing occupants, compared to those on unidirectional seats. This is primarily due to the longer trajectory involved during the secondary impacts. One effective way to remedy the situation is to install crashworthy bay tables to prevent any interaction between opposite passengers and to provide energy absorbers for cushioning the leg's or abdomen's collisions with the tables [4].

References

[1] Chatterjee, S. and Carney, J. F., III, "Occupant Protection and Interior Crashworthiness in Trains.", Internal Report, Vanderbilt Engineering Centre for Transportation Operations and Research, Vanderbilt University, Nashville, Tennessee, May 1995.

[2] Bowmer, C., "Report on the Proposed Levels of Injury Criteria for Use in Rail Passenger Vehicle Interiors.", The Engineering Link Technical Report, No. 95/XXX/6461/01, Derby, February 1995.

[3] Swindell, M., "Crashworthiness Development : Theoretical Methods for the Assessment of Vehicle Interiors & Occupant Kinematics.", British Rail Research Report, No. LR/VST/92/042, Derby, November 1992.

[4] Bowmer, C., "Report on the Development of a Crashworthy Table.", The Engineering Link Technical Report, No. 95/XXX/6461/03, Derby, March 1995.

Chapter 9
Conclusions

9.1 Concluding remarks on the studies of the behaviour of rakes of trains

A better understanding of the behaviour of vehicles in rakes has been achieved by the modelling work covered in this thesis, using non-linear mass-spring models to simulate the dynamic response of coaches connected by velocity-sensitive couplers.

Energy dissipative power, a parameter introduced by the present author, is a useful tool in determining the effects of damping, coach mass, impact velocity, crush-zone collapse force, wheel/track friction and external impulses on the dynamic behaviour of an interface of colliding trains. It was found that wheel/track friction has insignificant effects on the kinetic energy dissipation of an interface, and damping has only second-order effects.

Couplers have upset the theoretical energy distribution achieved by perfectly tuned gaps, causing the impact interface to be over-crushed and the last interface to be under-crushed, with all intermediate interfaces approaching the ideal crush distance. Couplers have also slightly lower the theoretical optimal gap size for any impact velocity higher than 4m/s.

Crush zones should preferably collapse with a hardening characteristic and avoid softening characteristics. For modern trains with a projecting nose at the ends, have mixed crush-zone characteristics : the impact interface collapses with a hardening characteristic and intermediate interfaces collapse with a fairly constant force. Such a mixed crush-zone arrangement has also demonstrated the ability to evenly distribute the collision energy along colliding rakes, provided the mean collapse forces of all the interfaces are of similar magnitudes.

The inclusion of linear structural damping for the mass-spring models makes the energy distribution results more realistic, and has also modified the derived pulses from a rectangular to a trapezoidal shape. Such a modification of the pulses has significant consequences on the interior crashworthiness and this will be highlighted in the next section.

The number of coaches in a train was found to have an insignificant effect on the overall energy distribution along colliding rakes, and this applies to crush zones that collapse with either a hardening or a constant force characteristic.

The work carried out in Chapters 3 and 4 have confirmed the validity of the sequential collision energy management philosophy. The good correlation in results achieved by the one-dimensional mass-spring models and a full scale rake test, has demonstrated the usefulness of these models in predicting rake behaviour.

9.2 Concluding remarks on the studies of forward facing occupant's kinematics

Forward facing occupants in open-bay seats are susceptible to serious injuries during secondary collisions, especially if the occupant is subjected to a long-duration pulse which remains active when the occupant contacted the opposite seat-edge. The resulting turning mechanism of the upper body can lead to serious head injuries.

Applied pulses with an initial relief, such as the type produced by Oleo couplers, were found to benefit the forward facing occupant during secondary collisions. Damping, however, increases his/her injury potential. Thus damping is an important factor and should be considered when deriving an applied pulse.

Most pulses derived from mass-spring models reported in this thesis, satisfy the head and neck injury criteria for the forward facing occupant, but not the legs. This has indicated a need to look into the preventive measures of possible leg injuries for the forward facing occupant. After a parallel arrival at the same conclusion, BR is currently in the process of evaluating a crashworthy bay table for preventing the legs of forward facing occupants to contact their opposite seat.

Change of velocity caused by an applied pulse is a good guide for preliminary assessment for the head injury potential of the occupant. The mean acceleration of the pulse should not exceed a threshold value and the work covered in Chapter 8 has suggested this to be 6.7g.

9.3 General conclusion

There is strong evidence, to suggest that interior crashworthiness and structural crashworthiness have contradicting design requirements. A train that is suited for one will have to sacrifice, in some ways, the other. This idea was first conceptually postulated by Chatterjee and Carney. After extensive studies of the behaviour of vehicles in rakes and the behaviour of occupants during secondary impacts, as reported in this thesis, a more concrete assertion of such an idea has been gained so that the above statement could be quantified.

9.4 Future studies

Possible continuations of the work reported by this thesis are :

(1) Extend the study of occupant kinematics in other seating layouts, such as Class 323 unidirectional seats.

(2) Effects of seat pitch and occupant size on interior crashworthiness should be studied in detail.

(3) How to prevent trains from derailing is very important. Derailment generally occurs during high-velocity collisions and greatly increases the chances of passenger fatalities. Identifying the parameters of a coach structure that favour its derailment should be considered.

(4) Studies on the prevention of vehicle over-riding each other during collisions are also very important. Past accident statistics have shown that over-riding is the major cause of fatalities in end-on collisions; in collisions with over-riding, the fatality rate per accident is many times that of collisions without over-riding.

(5) The crashworthiness performance of coach structures made by different materials should be compared. Recent studies in Stainless Steel and Composites have shown that these materials have achieved good controllable collapse characteristics and are potential candidates in replacing the aluminium alloy used currently in modern coaches.

(6) Studies on the behaviour of joints during a structural collapse are still at an infant stage with many potential research areas awaiting to be explored. A better understanding of the behaviour of joints will lead to their realistic numerical simulations.

Appendix A
Experimental study of HDPE tubes as an energy dissipating system

A.1 Introduction

Crashworthy studies have been very attentive towards investigating the energy absorbing characteristics of tubes/shells of different shapes & sizes subjected to axial loading. Hence one of the objectives for the current research work is to investigate this kind of problem. Morgan [1] has already examined the energy dissipating properties of some axially loaded plastic tubes. As an extension to his work, High Density Polyethylene (HDPE) tubes with various thickness to diameter (t/D) ratio were experimentally investigated in terms of their load-deflection characteristics when subjected to quasi-static axial loading. The experimental results obtained were then compared to some selected theories as highlighted in Chapter 2. One interesting feature of using HDPE tubes as an energy absorber is their ability to recycle after being crushed. i.e. after submerging the crushed tubes in boiling water for about 10 minutes, the tubes recovered somewhat to their original shapes & sizes, and the recycled tubes could be re-crushed and their load-deflection (or energy absorbing) characteristics could be re-assessed. This enables the study of the recycled energy-dissipative performance of the HDPE tubes. The idea of a recyclable energy absorber is very attractive from both economical and environmental viewpoints.

A.2 Theories for predicting the mean post-buckling load of axially crushed tubes

A.2.1 General

When a thin-walled tube (small t/D) is subjected to an axial quasi-static compression, the load-deflection would be typically look like one which is shown in Figure 2.7. From this graph, it can be seen that the tube has a high initial buckling force and this is followed by the post-buckling phase where a series of oscillating curves are observed. The mean value of these oscillating curves is distinctively lower than the initial peak load.

Tubes subjected to axial compression would buckle into the axisymmetric ring (as shown in Figure 2.4), or into the diamond-lobe buckling mode (Figure 2.5), or develop the mixed mode failure (the tube fails by axisymmetric mode and after forming a few buckles changes into a diamond mode). The study here only concerns with the diamond-lobe buckling mode of failure. Many theories have been proposed for predicting the mean post-buckling load of axially loaded tubes that collapsed into the axisymmetric ring or diamond-lobe buckling collapse mode, and the following assumptions are common to all theories :

(1) The material is assumed to be rigid-perfectly plastic.
(2) For the bending of a sheet of rigid-perfectly plastic material, the plastic bending moment per unit length, M_p is given by :

$$M_p = \frac{\sigma_0 t^2}{4} \tag{A.1}$$

where t is the tube wall thickness, σ_O is the effective yield strength of the material. Under plane strain conditions if the material obeys the von Mises criterion of yielding, then:

$$\sigma_o = \frac{2}{\sqrt{3}}\sigma_y \tag{A.2}$$

where σ_y is the yield strength under uni-axial tension or compression (assumed to be equal);
(3) The tube ends are free to deform or change shape, i.e. frictionless platens;
(4) The thickness of the tube wall is negligible compared to the crushing distance;
(5) The density of the tested material remains constant even after reheating for recycle purposes.

A.2.2 Alexander theory

Alexander [2] proposed a theory for predicting the mean post-buckling load of tubes which collapse into the axisymmetric ring mode. He did this by considering the work done in forming concentina with straight sided convolutions (see Figure 2.8) to which the final collapse shape is assumed. The work done includes bending at the circular joints and also stretching the material between the joints. The final expression of his theory is :

$$P_m = K\sigma_y t^{1.5}\sqrt{D} \tag{A.3}$$

where K is a constant equal to 0.59. Axisymmetric ring collapse mode does not appear in the HDPE tubes studied here.

A.2.3 Pugsley and Macaulay theory

Pugsley & Macaulay [3] derived a theory to predict the mean post-buckling load of tubes that deformed into the diamond buckling mode. It was assumed that the tube walls buckled into a diamond pattern and each diamond being approximately square with its diagonals in the longitudinal and circumferential directions. Their theory is based on the work done in the plastic bending along the lines of the final folds and also the work done in plastic shear distortion along the sides of each diamond (Figure 2.7). They only considered tubes which fail with 3 or 4 circumferential diamond buckling lobes, and derived the following expression for P_m :

$$\frac{P_m}{P_y} = C_1 \frac{t}{D} + C_2 \tag{A.4}$$

where P_y is the end load that would cause simple yielding in direct compression :

$$P_y = \pi D t \sigma_y \tag{A.5}$$

and C_1 and C_2 are constants depending on n, the number of diamond lobes formed. For n=3, the theory gives C_1=3.24 and C_2=0.12. Pugsley and Macaulay did not consider n=2 for their theory as the two diamond-lobe failure mode is rarely seen in metallic tubes.

A.2.4 Johnson *et al.* theory

Johnson, Soden and Al-Hassani [4] proposed 2 theories to predict the mean post buckling load for the inextensional diamond collapse mode of axially compressed thin-walled tubes. The first theory takes account of the energy absorbed in forming stationary plastic hinges. The second theory considered the effect of a travelling hinge mechanism. A travelling hinge is a plastic hinge which moves relative to the material of the tube which allows the progressive plastic collapse of tube during crushing. These theories are discussed separately in the sections to follow.

Stationary hinge theory

This mechanism considers the plastic work done in compressing the tube to be in 2 parts : folding along the curve surface and that done by flattening the curve surface, giving :

$$\frac{\sigma_m}{\sigma_y} = \frac{t}{\sqrt{3}D}\left[1 + n.cosec(\frac{\pi}{2n}) + n.cot(\frac{\pi}{2n})\right] \tag{A.6}$$

where σ_m is the mean post-buckling stress (i.e. P_m divided by the cross section area of the tube).

Travelling hinge theory

The equation including the travelling hinge is :

$$\sigma_m = \frac{\sigma_y}{\sqrt{3}}\left(\frac{t}{D}\right)\left[\frac{\frac{D}{r} - n.cot(\frac{\pi}{2n}) + 1 + n.cosec(\frac{\pi}{2n})}{(1 - \frac{2r}{h_1})}\right] \tag{A.7}$$

where $r = \frac{D}{A}\left(\sqrt{1 + \frac{h_1 A}{2D}} - 1\right)$ and A=1+$n.cosec(\pi/2n)$-$n.cot(\pi/2n)$.

For the physical meaning of the trigonometry notation employed in these equations, refer to Figures 2.10 to 2.12 in Chapter 2.

These theories suggest that the mean post-buckling stresses for tubes with the diamond-lobe collapse mode are straight lines of different gradients ('*n*' dependent) passing through the origin.

A.2.5 Thornton and Magee theory

Thornton & Magee [5] discovered by experimental observation that the energy absorbed per unit mass in axially compressed metallic cylindrical shells, E_s^c (specific compressive energy absorbed) obeys the expression :

$$E_S^c = B(\frac{t}{D})^z \tag{A.8}$$

where B and z are material dependent constants. The study here will obtain these constants experimentally for HDPE tubes.

A.2.6 Comments

These theories are developed on the basis of simplifying assumptions, and some authors even modified their own theory by accepting their experimental results semi-empirically.

A.3 Material, machine and methods

A.3.1 The testing machine

The tensile/compression testing machine used for the current work was a Mayes 100kN tester capable of doing both static & fatigue tests for most engineering materials. It has a x-y plotter built-in to its control panel for plotting force against deflection while a test is being performed. The rate of loading for any test is selected by the user and the rate of loading selected for the crushing of HDPE tubes was 10 mm/min, in order to be consistent with the tests carried out by Morgan [1].

Specially manufactured steel platens were attached to the testing machine's vices. The surfaces of the platens were ground to provide a dry, nominally frictionless surface for the ends of the specimens to slide on. These serve as parallel flat rigid platens for compressing the tube axially.

A.3.2 The tensile properties of HDPE

The specimens used in the experiment are High Density Polyethylene (HDPE) extruded tubes. The tubes came in a nominal external diameter of 90 mm and internal diameter of 79 mm (i.e. thickness t=5.5 and mean diameter D=84.5) which gives a t/D ratio of 0.0651. A total of 4 HDPE strips (see Figure A.1) were cut from the tubes and tested for their true stress against true strain plots as shown in Figure A.2. A typical engineering stress-strain curve is also shown in Figure A.3. The data tabulated over the page summarises these test results :

Young modulus (GN/m^2)	Yield stress (MN/m^2)	Ultimate tensile strength (MN/m^2)	Fracture stress (MN/m^2)	Fracture strain
0.67	13.4	24.0	99.05	0.66

Table A.1 : Mechanical properties of HDPE used by this project.

The true stress against true strain curves for three notched strip specimens (specimen A, B and C) are shown in Figure A.2. These curves are important because they enable the determination of the constant plastic stress that could approximate the actual collapse process. Such a perfectly plastic approximation would then enable the application of the theories discussed in Section A.2 to be applied to the tested tubes. The calculated results can then be compared with those obtained experimentally. The main aim here is to determine the perfectly plastic yield stress σ_y so as to used it in Equations A.1 to A.7.

Figure A.2 shows that the tensile behaviour of HDPE could roughly be classified into three categories : an elastic loading up to a proof stress of 13.4 MN/m^2, followed by a 'fairly-flat plateau' during the early stage of plastic deformation, the hardening slope increased (indicating severe necking) and the plastic deformation continued with the increased stiffness until final fracture. The range of true strains for which the 'plateau' occurred is between 0.05 to 0.2, representing about one third of the total plastic deformation. It is assumed that the tube collapse process would be dominated by this early stage of plastic deformation in the 'plateau' of Figure A.2, since the tubes are expected to be only moderately stressed and severe necking is not expected to occur. This assumption will be validated later in Appendix B.

With these assumptions, data points from the plastic region with the range of strain between 0.05 to 0.2 on Figure A.2 were re-plotted on Figure A.4. A best line fit for a constant true stress is 19.2MN/m^2. This will be employed as σ_y in Equations A.1 to A.7 later.

The other physical property of HDPE required by the study here is the density. This was easily found by dividing the mass of a tube by its volume. The mass of a tube was found by using an electrical weighing machine sensitive enough to measure up to 1/10 of a gram. The density of HDPE was found to be 975 kg/m^3. This agreed with the data provided by Ashby & Jones [6].

A.3.3 The HDPE tube specimens

The tube specimens crushed in the experiment are sized as shown in Figure A.5. The thickness of some tubes were reduced to various sizes by turning down the outside diameter to the required thickness. The final geometry of the specimens being tested are as tabulated in Table A.2 :

Specimen no.	Internal diameter (mm)	External diameter (mm)	*t/D*	length (mm)
1 to 3	79	90.00	0.0651	97
4 to 6	79	87.75	0.0525	97
7 to 10	79	86.75	0.0468	97
11 to 14	79	85.75	0.0410	97
15 to 18	79	84.75	0.0351	97
19 to 22	79	83.75	0.0292	97

Table A.2 : Specimen numbers & geometry.

There were more than one specimen for each *t/D* ratio, and for ease of graphical presentation, the results obtained for each *t/D* ratio were averaged. This is consistent with Morgan's [1] experimental results.

A.3.4 Interpretation of results : Energy absorbed

For every HDPE tube crushed, a load-deflection graph would be plotted automatically by the machine's plotter. A typical graph is shown in Figure A.6. The energy absorbed during the compression of each tube specimen was determined by calculating the area, A_C, (see Figure A.6) under its force/deflection curve. This is quite easily achieved, since standard SI graph papers were used in the machine's plotter. However, an upper bound deflection was instigated for each tested specimen which corresponded to the point at which the specimen was fully compressed and hence the compressive force began to increase rapidly. This was taken as an upper bound because any energy absorbed after this point would be due to the compression of the tube wall material and hence was not relevant to the present study.

A.3.5 Interpretation of results : Mean post-buckling load

The area A_p bounded by the load-deflection curve (see Figure A.6), the x-axis and the lower bound extension point was calculated for each specimen. The area A_p represents the energy absorbed by each specimen throughout the duration of the initial peak load and hence the lower bound extension corresponded to the point at which the initial peak force had subsided. The A_p values were subtracted from the A_C values. The resulting area, A_m represented the energy absorbed by each specimen during the post-buckling collapse. A_m was then divided by the distance between the upper & lower

extension bounds to give the mean post-buckling load. Typical upper & lower extension bounds are indicated in Figure A.6.

A.4 Results

A.4.1 Tests done on original/machined tubes

The following table shows the results of tests carried out on the original tubes (or those machined from the original tubes) :

t/D	P_m. (kN)	P_o (kN)	E_s^c (kJ/kg)	$\frac{\sigma_m}{\sigma_y}$
0.0651	11.14	31.44	6.38	0.40
0.0525	6.91	23.17	4.92	0.31
0.0468	5.41	18.57	4.75	0.28
0.0410	3.86	17.07	3.94	0.23
0.0351	3.65	13.31	4.19	0.26
0.0292	2.57	12.18	3.67	0.22

Table A.3 : Results for original/machined tubes .

A.4.2 Tests done on the reheated HDPE tubes

Table A.4 over the page shows the results for the tests carried out on the tubes after the reheating :

t/D	P_m. (kN)	P_o (kN)	E_s^c (kJ/kg)
0.0651	8.41	20.57	4.54
0.0525	4.75	11.58	3.64
0.0468	5.29	8.44	3.89
0.0410	3.13	10.23	3.23
0.0351	2.63	4.86	2.88
0.0292	2.15	4.66	2.59

Table A.4 : Results for the reheated-and-recrushed tubes.

By comparing the corresponding initial peak load (P_o) in Tables A.3 and A.4, it is seen that the P_o is deteriorating after each crush and reheat process. This is mainly due to the failure of the crushed tubes to fully recover to their original perfect circular shape and sizes after the reheat. This will be elaborated later.

A.4.3 Modes of collapse

The axial crushing of HDPE tubes investigated here only encountered the diamond-lobe collapse mode of failure. 2 types were found, i.e. n=2 and n=3. Table A.4, which includes Morgan's [1] results on some other polymeric tubes, shows the relationship between t/D and n :

t/D	n	Material
0.0229	3	PVC
0.0291	3	PVC
0.0292	3	HDPE
0.0351	3	HDPE
0.0410	3	HDPE
0.0468	3	HDPE
0.0481	2	Polypropylene
0.0525	2	HDPE
0.0552	2	Polypropylene
0.0651	2	HDPE
0.0672	2	ABS
0.0711	2	Polypropylene
0.0793	2	PVC

Table A.5 : Mode of collapse against t/D.

A.5 Discussions

A.5.1 Comparison with theories

The following sections compare the experimentally obtained P_m (mean post-bucking load) and those predicted by the theories highlighted earlier. Note that experimental data from Morgan [1] which included Polypropylene, Acrylonitrile-Butadiene-Stryrene (ABS) and Unplasticised Polyvinyl Chloride (PVC) tubes, were included here to augment the HDPE tubes data for the two diamond-lobe failure mode (i.e. n=2). For the n=3 failure mode, the HDPE specimens have sufficient data points on their own (see Table A.5) so no augmentation is needed. As mentioned in Section A.3.2, the mean yield stress for HDPE is 19.2MN/m^2 and this value will be used for all the theories.

Johnson *et al.* theory

With Table A.3, the graphs of σ_m/σ_y against t/D for n=2 and 3 are plotted in Figures A.7 and A8 respectively. Figure A.7 has included Morgan's [1] experimental data points (for n=2). Both graphs have the Johnson *et. al.* theoretical lines superimposed : Equation A.6 (the stationary hinge theory) and Equation A.7 (travelling hinge theory). It can be seen that for n=2, the experimental data agreed fairly well with the travelling

hinge theory. Whereas for n=3, the experimental data agreed fairly well with the stationary hinge theory. This is entirely in agreement with previous works by Morgan [1] and Johnson *et al* [4] on axial crushing of plastic tubes, where it had been established that the initial failure mode for n=2 differed from those of n=3. The n=2 mode failed initially by yielding at a circumferential hinge near one end of the tube which then collapsed progressively in the n=2 mode. The n=3 mode appeared to fail firstly by elastic instability and the travelling hinge mechanism was less pronounced. In relatively thick tubes where n=2 is observed, the plastic travelling hinge theory could represent the deformation process. For the n=3 mode of collapse, where the tubes are considerably thinner, elastic instability seems to dominate the initial collapse pattern and hence the Johnson *et al.* theory seems not to hold true.

Pugsley and Macaulay theory : For cases with n=3 only

For cases with n=3 deformation, it is useful to compare with the Pugsley & Macaulay theory [3]. This is shown in Figure A.9. The Pugsley & Macaulay theory takes the form of $\frac{P_m}{P_y} = C1\frac{t}{D} + C2$, where C_1 and C_2 are constants and the theory established C_1=3.24 and C_2=0.12 for the n=3 collapse mode. Figure A.9 has shown all the experimental HDPE tube crushing data to agree fairly well with the Pugsley & Macaulay theory.

Energy absorbed : Thornton and Magee theory

Tables A.3 and A.4 have highlighted, for original and reheated (recycled) cases, the specific energy absorbed for each t/D ratio. These are plotted on a log-log scale as suggested by the Thornton & Magee theory (in Equation A.8) [5], on Figure A.10. It can be seen that the 2 sets of experimental data (original/machined tubes, reheated-and recrushed tubes) each fit well on a log-log straight line.

Equation A.8 (Thornton & Magee theory) has the form $E_s^c = B(\frac{t}{D})^z$. From Figure A.10 the constants B and Z can be evaluated for the tested HDPE tubes. They are tabulated in Table A.6 below :

	B	Z
Original/machined tubes	49.76	0.77
Reheated-and-recrushed tubes	33.83	0.74

Table A.6 : The constants B and Z in Equation A.8 as determined from Figure A.10.

An obvious trend is seen from Table A.6 : B and Z reduce after the crush-reheat-recrush process. i.e. energy dissipative capability has deteriorated after the first crushing. This is also obvious if one compares the two sets of experimental data shown in Figure A.10. Since mean post-buckling load P_m is directly proportional to the energy absorbed, we can expect P_m to deteriorate by the same proportion as well.

The main reason for such deterioration could be attributed to the failure of perfect recovery of the tube during the reheating process. There will always be some 'wrinkles' left behind from the previous plastic hinges. These wrinkles serve as initial imperfections to eradicate the high initial peak buckling load (refer to Tables A.3 and A.4). The post-buckling collapse process would also be easier with such wrinkles serving as 'guides' for the recrushed plastic hinges to follow and so no new plastic hinge was developed, all recrushed plastic hinges always followed the 'old-wrinkle lines'. If the HDPE tubes were to be employed as recyclable energy absorbers, then their loss in specific energy absorption after the collapse process should be noted.

A.5.2 The energy dissipating performance of 'recycled' tubes

It is of interest to know the alteration of energy dissipative capability after each crush and reheat process. This could be assessed by the absorbed energy ratio, i.e. the ratio of the specific energy absorbed for a first-crushed tube before the reheat process, $(E_s^c)_{pre}$, to the specific energy absorbed during the recrush after the reheat process, $(E_s^c)_{post}$. Table A.7 provides this information for both the first and second reheat processes for the HDPE tubes studied :

(1)	(2)	(3)	(4)
$(E_s^c)_{pre}$ kJ/kg	$(E_s^c)_{post}$ kJ/kg	Energy ratio (1)/(2)	*t/D*
3.67	2.59	1.42	0.0292
3.19	2.88	1.45	0.0351
3.94	3.23	1.22	0.0410
3.75	3.89	1.22	0.0468
3.92	3.64	1.35	0.0525
6.30	3.54	1.41	0.0651

Table A.7 : Energy ratio Vs *t/D* for the re-crushed tubes.

Base on the results of energy ratio against *t/D* shown in Table A.7, another graph, Figure A.11, was plotted basing to show the relationship between the energy ratio against *t/D*. The data points show much scatter with no noticeable trend, suggesting that the energy ratio for the HDPE tube crushing and recrushing is not dependent on the *t/D* ratio. However, if more specimens were used for testing, then a more confident conclusion could be made on this contention.

The data in Table A.7 has shown that the average loss in specific energy absorption between the first-crushed tubes and the recrushed tubes is between 22% and 45%.

A.5.3 Comparison of the performance of specific energy absorption for various plastic materials

Tubes with four types of plastic materials were tested both by Morgan [1] and in this study : ABS, HDPE, PP and PVC. Figure A.12 shows the log-log plots (Thornton & Magee theory) between the specific energy absorbed (E_S^C) and *t/D* for all the tubes tested by Morgan and the author. It can be seen that the ranking for these four materials is in the following order (in order of merit) :

(1) PVC;
(2) ABS;
(3) PP;
(4) HDPE.

Table A.8 below shows a ranking criterion σ_y/ρ for the four polymeric materials, i.e. for tubes with same size and shape, the larger σ_y/ρ for the tube material, the better is the specific energy absorption for the tube :

Material	σ_y MN/m^2.	ρ kg/m^3.	σ_y/ρ kNm/kg
PVC	40.2	1380	29.3
ABS	28.1	1060	26.5
Polypropylene	19.1	895	21.3
HDPE	19.2	975	19.7

Table A.8 : σ_y/ρ as a ranking criteria for polymeric tubes in term of specific energy absorbing capability.

It does not come as surprise that σ_y/ρ is a good indicator for ranking the material of axially loaded tubes in terms of specific energy absorbing capability. A simple derivation of a mathematical expression between specific energy absorbed by an axially loaded tube and the σ_y/ρ of the tube material would explain this.

Consider an axially loaded tube with a length *l*, a cross sectional area *A*, a thickness *t*, a mean diameter *D*, a constant plastic yield strength σ_y and a density ρ. According to various theories, the mean post-buckling load P_m of an axially loaded tube is a function of *t/D* $\left(\text{i.e. } f\left(\frac{t}{D}\right)\right)$ multiplied by the yield force of the tube ($\sigma_y A$), or :

$$P_m = (\sigma_y A) f\left(\frac{t}{D}\right) \tag{A.9}$$

Since P_m is proportional to energy absorbed (E) during the crushing process, we have the following expression for E :

$$E = (\sigma_y A)(k)\left[f\left(\frac{t}{D}\right)\right] \tag{A.10}$$

where k is a constant depending on the stroke of crushing of the tube. The specific energy absorbed (E_S^C) for the tube is :

$$E_S^C = \frac{E}{\rho A l} = \left(\frac{\sigma_y}{\rho}\right)\left(\frac{k}{l}\right)\left[f\left(\frac{t}{D}\right)\right] \tag{A.11}$$

The second and last term on the right hand side of Equation A.11 are geometric parameters of the tube, and the first term is of course σ_y/ρ , the criterion for ranking the material of the tube for its specific energy dissipative capability.

A.5.4 Transition of collapse mode between 2 diamond lobes and 3 diamond lobes

From Figure A.7 and A.8, it was found that a possible transition range of *t/D* exists for the changeover of n=2 collapse mode to n=3 collapse mode. This range was found to be between 0.0481 and 0.0468. The experimental data from Johnson *et al.* [4] on PVC tubes agreed with this finding.

Figure A.13 is plotted to show more clearly the relationship between n & *t/D*, for the range of *t/D* tested by Morgan [1] and those in the present study. Changeover mode of deformation would accompany a change in the post-buckling load performance as seen from Figure A.7 and A.8. Hence it is useful to identify the *t/D* (of axially crushed tubes) where changeover occurs for various energy dissipating systems.

A.6 Conclusions

The following can be summarised for the experimental work done in this Appendix :

(1) The two diamond-lobe buckling mode for all the plastic tubes tested has shown close agreement with the travelling hinge theory.

(2) The departure from travelling hinge theory for cases with three diamond-lobe collapse, is thought to be caused by the elastic instability of thin walled tubes under axial compression.

(3) The Pugsley and Macaulay theory adequately describes the mean post-buckling load for the three diamond-lobe collapse mode of HDPE tubes.

(4) The compressive energy absorbed by the tubes obeys the Thornton & Magee theory, even for the recycled HDPE tubes.

(5) The ratio $\frac{\sigma_y}{\rho}$ is a good indicating factor for ranking the material of the tube in terms of its capability of absorbing specific compressive energy.

(6) The loss in the energy absorbed for the HDPE tubes before & after each recycled process seems to be independent of the thickness to diameter ratio (*t/D*).

(7) The possible range of *t/D* for a changeover of two diamond-lobe to three diamond-lobe collapse for the plastic tubes tested, was suggested experimentally to be $0.0481 < t/D < 0.0468$.

(8) Geometrical recovery of the crushed HDPE tubes after the reheating process was found not to be perfect. Re-crushing always follows the old-wrinkle lines left-behind by the plastic hinges formed during the first crushing. As such the recrushed tubes can lose up to 45% of their specific energy absorption when compared with their original conditions.

References

[1] Morgan, J. S., "Axially Loaded Cylindrical Shells as Energy Absorbers.", Final Year Undergraduate Project Report, Department of Mechanical & Process Engineering, University of Sheffield, June 1992.

[2] Alexander, J. M., "An Approximate Analysis of Thin Cylindrical Shells Under Axial Loading.", Quart. J. Mech. Appl. Maths., Vol. XIII, p. 10, 1960.

[3] Pugsley, A. & Macaulay, M., "The Large Scale Crumpling of Thin Cylindrical Columns.", Quart. J. Mech. Appl. Maths., Vol. XIII, p. 1, 1960.

[4] Johnson, W., Soden, P. D. & Al-Hassani, S. T. S., "Inextensional Collapse of Thin Walled Tubes under Axial Compression.", J. Strain Anal., Vol. 12, p. 317, 1977.

[5] Thornton, P. & Magee, C. L., "The Interplay of Geometric & Materials Variables in Energy Absorption.", J. Eng. Mat. & Tech., Vol. 29, p. 114, 1977.

[6] Ashby, M. F. & Jones, D. R. H., "Engineering Materials I.," Pergaman Press, Oxford, 1988.

Appendix B
DYNA3D simulations for tube crushing

B.1 Introduction

A number of non-linear Finite Element (FE) models were created, as part of the crashworthiness study package, to simulate the following experimental tests :

(1) Quasi-static axial compression of a High Density Polyethylene (HDPE) tube between steel platens. The experimental work for this model was reported previously in Appendix A;

(2) Quasi-static axial compression of a conical Rigid Polyvinyl Chloride (PVC) tube between rigid platens. The results of this model was compared with those obtained experimentally by Mamalis *et al.* [1];

This appendix highlights the results of 3 FE models. They were created by using the pre-processor FEMGEN which is available in the computer network operated by Sheffield University Computing Services. These meshed models prepared by FEMGEN were then converted into an input file 'recognisable' by the non-linear Finite Element code DYNA3D. This is carried out by a program called NCODE which comes with DYNA3D. The input files were then submitted to DYNA3D for analysis. Results were analysed by the post-processor D3PLOT which also comes with DYNA3D.

The main purpose of performing all these tube crushing simulations was to get familiar with the use of DYNA3D. The experience gained in these exercises would enable future analyses, conducted without the benefit of prior tests, to be made with more confidence. To be able to use DYNA3D effectively as simulations for crushing of structures is of great advantage in crashworthiness study in the railway industry. As actual full scale train collision test is very costly. FE modelling works play an important role in modern train design.

Section B.2 describes two models of a HDPE tube with a t/D of 0.0651, being crushed between steel platens. One model used a true material's stress-strain property (i.e. the true stress-true strain curve of HDPE obtained experimentally in Appendix A) for the HDPE tube, the other used a bi-linear stress-strain curve (i.e. using only the initial part of the true plastic deformation curve). These two models would validate the assumption made previously in Appendix A on the early stage of plastic deformation (less than 0.2 of true strain) dominates the response of the HDPE tube crushing. Section B.3 described the model of a conical PVC tube being crushed axially. Section B.4 discusses the results produced by all the models making comparisons with the experimental results. Section B.6 summarises the conclusions for this Appendix.

B.2 The DYNA3D simulation of the axial crushing of a HDPE tube with a *t/D* of 0.0651

Two models were created to simulate the axial crushing of the thickest (original) HDPE tube as reported in Appendix A. Both models shared exactly the same geometrical co-ordinates for all the nodes. The models have two parallel solid platens separated by the tube, as shown in figure B.1, with a small 1mm (about 1% of the tube height) initial separation between the tube and the unmoveable top platen.

B.2.1 The HDPE tube in the models

The HDPE tube for both models described here, has 800 nodes which form a total of 768 quadrilateral shell elements as shown in figure B.1. The first model, known as HDPE-true, used the full HDPE true stress-true strain curve (as shown in figure B.2) for the material of the tube. The other model, known as HDPE-bilinear, used a bi-linear simplification to substitute the HDPE true stress-true strain curve, also shown in figure B.2. The mean diameter and wall thickness for the tubes in both models are 84.5mm and 5.5mm, the same as the actual tube tested. Poisson's ratio for HDPE was taken as 0.4, this was thought to be a reasonable value for HDPE since it is a thermoplastic material.

Actual man-made components are not perfect geometrically no matter how good the manufacturing process is. Problems involving structural buckling are very sensitive to the initial structural imperfections contained in the structures. It is thus realistic to introduce some small imperfections to the tube radii. From figure B.1, it is seen that the nodal x and y co-ordinates of tube model define a tube radius R on a lateral plane. If a random factor K with $0.99 \le K \le 1.01$ (i.e. within the range of ±1%) is multiplied to every pair of x and y co-ordinates of the nodes, then an imperfection of 1% would be introduced to the radii of the tube. This is achieved by running a FORTRAN program which would multiply the x and y co-ordinate by a random number K and $0.99 \le K \le 1.01$. As a result, the tube model has a small zigzag appearance over its circumference when viewed from the plan. This technique was extensively studied by Distin [2] and 1% to 1.5% random imperfections were found to be suitable in modelling the axial tube crushing tests.

B.2.2 The Platens in the models

The platens were modelled as rigid bodies, i.e. not required to input any stress-strain property as they will not deform. This is reasonable since the steel platens are practically rigid when compared with the stiffness of the HDPE tube. This also saved CPU time for analysing the models since no evaluation of stress or strain was required for the platens. Each platen has a dimension of 160mm by 160mm for the cross-section area and a thickness of 12.5mm. They were meshed into 898 nodes with a total of 400 six-node-brick elements, as shown in figure B.1. The platens were parallel to each other with the surface perpendicular to the tube axis. The top platen was fixed so that it could neither rotate or translate in all directions, but the bottom platen is allowed

only to translate in the z-direction (see figure B.1), so that it could move upward and crush the tube.

B.2.3 The loading speed

The quasi-static loading rates for most experiments discussed here are too slow and are not suitable for DYNA3D, which is meant for analysing models with high impact velocity. If the actual compression speed was used on the HDPE tube crushing models, they would take weeks to solve. Loading rate was thus considerably increased to the level of 5m/s. This was thought to be justified since the tube model would not be sensitive to strain rate if one had chosen not to use strain-rate dependent material (which is selectable in DYNA3D). Also, the inertia effect of the models is only of second order significance.

For the HDPE tube crushing models, a velocity load curve was imposed to all the nodes in the bottom platen as shown in Figure B.3. Note that the initial rising portion of the load curve (before 9msec) was half a cosine curve which immediately joined a constant loading velocity of 5m/s for the rest of the analysis. A cosine rise curve was chosen instead of step or ramp rise curve to reduce the noise in the initial part of the analyses.

B.2.4 Contact surfaces

Defining contact surfaces for the models is important. Without careful consideration, two surfaces that are supposed to meet and react against each other would simply pass through one another and the model fails. For the case of modelling the crushing of a HDPE tube between platens, the contact surfaces anticipated are straight forward : The top platen and all the nodes in the tube, the bottom platen and all the nodes in the tube and the tube self contact when severe buckling caused layers of diamond lobes to contact one another. All such contact surfaces are available in DYNA3D, and so a total of three contact surfaces were defined for the HDPE tube crushing models.

B.2.5 Summary input information for the two models simulating the axial crushing of a HDPE tube with a *t/D* of 0.0651

The summary of input data for both the HDPE tube crushing models are shown in Table B.1 :

	Model HDPE-true		Model HDPE-bilinear	
	The platens (each)	The HDPE tube	The platens (each)	The HDPE tube
Dimension	160mm x 160mm x 12.5mm	*D*=84.5mm height=200mm *t*=5.5mm	160mm x 160mm x 12.5mm	*D*=84.5mm height=200mm *t*=5.5mm
No. of nodes	898	800	898	800
Type of element	Solid 8-node brick	Quadrilateral shell	Solid 8-node brick	Quadrilateral shell
No. of elements	400	768	400	768
Types of material	Rigid body	Stress-strain curve as shown in Figure B.2.	Rigid body	Stress-strain curve as shown in Figure B.2.
Loading curve	As in figure B.3 (bottom platen only)	---	As in figure B.3 (bottom platen only)	---
Constraints	Top platen is fixed, bottom platen is allowed to move straight axially.	---	Top platen is fixed, bottom platen is allowed to move straight axially.	---
Remark	---	1% imperfection was introduced to its radial nodal co-ordinates.	---	1% imperfection was introduced to its radial nodal co-ordinates.

Table B.1 : Input data summary for various component used in the model HDPE-true and the model HDPE-bilinear.

It is clear that the two models differ only in the material stress-strain curve defined for the HDPE tube. So any difference in their results should be caused by the difference in the material stress-strain curves of both tubes.

B.3 The DYNA3D simulation of the axial crushing of a conical PVC tube

The initial state of this model is shown in Figure B.4. The conical tube has a smaller diameter of 36.1mm at the top, and a bigger diameter of 58.3mm at the base. The tube is meshed into 1152 four-node quadrilateral shell elements with 1188 nodes. The thickness of the tube wall is 1.6mm and the height is 58.3mm. The top platen is modelled as a 70mm by 70mm square plate and meshed into 784 shell elements with 5mm thickness. The bottom platen is a 87mm by 87mm square plate and meshed into 576 shell elements with 5mm thickness. This model is named PVC-conic. The input data is summarised as below :

	PVC-conic		
	The top platen	The bottom platen	The PVC tube
Dimension	70mm x 70mm x 5mm	87mm x 87mm x 5mm	D_1=36.1mm, D_2=58.3mm, L=127mm, t=1.6mm
No. of nodes	841	625	1188
Type of element	Quadrilateral shell	Quadrilateral shell	Quadrilateral shell
No. of elements	784	576	1152
Types of material	Rigid body	Rigid body	Stress-strain curve as shown in Figure B.5.
Velocity load curve	As in figure B.3	---	---
Constraints	Allow to translate axially.	Fixed in space.	---
Remark	---	---	1% imperfection was introduced to its radial nodal co-ordinates.

Table B.2 : The summary of input data for the simulation of the crushing of the conical PVC tube.

The top platen has finer elements so as to be compatible with the finer element at the top end of the tube. The platens are now modelled as 4-node shell elements instead of solid 6-node brick elements. Accumulated experience has shown that the platens when modelled as rigid bodies, meshing them into 4-node shell elements or solid 6-node brick elements would produced similar results.

B.4 Results and discussions

B.4.1 The axial crushing of HDPE tubes

The load-deflection results for both models, HDPE-true and HDPE-bilinear, are shown in Figure B.6 together with the one obtained experimentally. The progression of the simulated crushing event for the tube at various time interval for the model HDPE-bilinear is as shown in Figure B.7. It can be seen that the collapse of the tube was initiated by forming an axisymmetric ring at around 10msec, then this ring quickly collapsed to form two diamonds and the subsequent deformations took on this 2 diamond-lobe pattern until the end of the computations. The mode of buckling as predicted by the model was the same as those observed in the experiment. Similar models of the axial crushing of HDPE tubes (using the bi-linear stress-strain curve for the HDPE tubes) with other t/D ratio have been created and also produced the same mode of buckling as those observed in experiments, i.e. thicker tubes buckled into 2 diamond lobes and thinner tubes buckled into 3 diamond lobes. To demonstrate the results of one of these models with t/D=0.0351 (i.e. one that would collapse into 3 diamond lobes), the load-deflection curves (both computed and experimental) are as shown in Figure B.8 and the sequential animation of the crushing of the tube for the model are as shown in Figure B.9.

From Figure B.6, it is clear that the use the full true stress-true strain curve for the tube model is not necessary as the bi-linear curve would produced almost identical results. This also has validated the previous assumption that the first 30% of the true plastic strain from the true stress-true strain curve of HDPE (i.e. up to 0.2 true strain where the 'plateau' is located) has dominated the whole crushing behaviour of the tube.

Both Figure B.6 and B.8 have shown that the computation results have under-estimated the experimental initial peak buckling load, although the same order of magnitude were obtained. The post-buckling behaviour, however, was satisfactorily re-produced by the models. The initial buckling load is well known to be highly sensitive to the imperfections contained within the tube, which could be geometric (such as those modelled here) or material. It is extremely difficult to model these imperfections exactly as they were contained in the tube, which partly contribute to the failure for the models to reach the experimental initial peak load. Also the simplification of using shell elements for modelling the tubes and rigid bodies for the platens would also effect the accuracy of the models. If 3-dimensional brick elements were used for the tubes and deformable platens were modelled instead of rigid bodies, better results for matching the experiments would certainly be obtained but this is done at the expense of high CPU times. The CPU times for the three models are : 3.3 hours for HDPE-true, 2.0 hours for HDPE-bilinear and 4.7 hours for the model with a t/D of 0.0351 for the tube. The higher CPU times for the last model was due to the fine meshes used in order to facilitate the higher number of diamond-lobes buckled. In view of using these simple models for simulating HDPE tubes with large plastic buckling behaviour, the results shown in Figure B.6 and B.8 are considered to be acceptable in terms of post-buckling behaviour, total energy absorbed and fairly low CPU times.

B.4.2 The axial crushing of the conical PVC tube

The load-deflection results of the model PVC-conic are as shown in Figure B.10 together with the experimental results. The progression of the simulated crushing event for the tube at various time intervals for the model is shown in Figure B.11. The model has predicted a 2-lobe buckling mode developed at the smaller end which progressively spread to the bigger end. The last diamond-lobe formed at the bigger end is a 3 lobe deformation. This is exactly what was reported in Reference [1] during the experiment. The simple model (2 shell plates crushing a shell tube in between) has accurately predicted the actual mixed-mode buckling as observed during the experiment.

Figure B.10 has again shown that the model failed to reach the experimental initial peak load level, but the computed post-buckling curve closely matched the experimental results. These observations resemble those mentioned in the previous models in the HDPE tubes.

B.5 Conclusions

(1) The use of simple DYNA3D models could produce results that match quite closely with those obtained experimentally at acceptable CPU times. All models have predicted the correct mode of failure. The post-buckling load-deflection characteristics observed in the experiments were fairly well re-produced by the models, but the models consistently under-estimated the initial peak buckling load. Improvements could be made to these simple models to rectify this shortcoming, but would be done at the expense of increased CPU times.

(2) The use of bi-linear stress-strain characteristics for the HDPE tube material to substitute its full stress-strain curve was justified because both produced identical results. Since the bi-linear curve only considers the initial stage of the true plastic deformation (up to 0.2 true strain, i.e. the stress 'plateau' as mentioned in Appendix A), the previous assumption made in Appendix A that the HDPE tube collapse process must be dominated by this early stage of plastic deformation is validated.

References

[1] Mamalis, A. G., Manoakos, D. E., Viegelahn, G. L., Vaxevanidis, G. L. & Johnson, W., "On the Inextensional Axial Collapse of Thin PVC Conical Shells.", Int. J. Mech. Sci., Vol. 28, No. 5, p. 323, 1986.

[2] Private communication with Distin, K. W. on 1st September 1993, after the seminar on Crashworthiness of Rail Vehicles organised by Advanced Railway Research Centre in Stephenson Hall of Residence, Sheffield University.